Atomic scale in situ control of Si(100) and Ge(100) surfaces in CVD ambient

D i s s e r t a t i o n

zur Erlangung des akademischen Grades

d o c t o r r e r u m n a t u r a l i u m

(Dr. rer. nat.)

im Fach Physik

eingereicht an der

Mathematisch-Naturwissenschaftlichen Fakultät I

der Humboldt-Universität zu Berlin

von

Dipl.-Ing. Sebastian Brückner

Präsident der Humboldt-Universität zu Berlin:

Prof. Dr. Jan-Hendrik Olbertz

Dekan der Mathematisch-Naturwissenschaftlichen Fakultät I:

Prof. Stefan Hecht, PhD

Gutachter/innen: 1. Prof. Dr. Recardo Manzke

2. Prof. Dr. Thomas Hannappel

3. Prof. Dr. Wolf Gero Schmidt

Tag der mündlichen Prüfung: 21.11.2013

Zusammenfassung

In dieser Arbeit wurde die atomare Oberflächenstruktur von Si(100)- und Ge(100)-Oberflächen untersucht, die mittels metallorganischer chemischer Gasphasenabscheidung (MOCVD) für anschließende Heteroepitaxie von III-V-Halbleitern präpariert wurden. An der Grenzfläche des Gruppe-IV-Substrates zur III-V-Schicht führen atomare Einfachstufen auf der Substratoberfläche zu Antiphasenunordnung in der epitaktisch gewachsenen Schicht. Dies kann jedoch durch Erzeugung von atomaren Doppelstufen auf dem Substrat vermieden werden. Die MOCVD-Prozessgasumgebung hat einen starken Einfluss auf die Domänen- und Stufenbildung der Si(100)- und Ge(100)-Oberfläche. Deswegen wurden in situ Reflexions-Anisotropie-Spektroskopie (RAS) und verschiedene Ultrahochvakuum-(UHV)-basierte oberflächensensitive Messmethoden verwendet, um die verschiedenen Oberflächen in Abhängigkeit von der Präparation zu charakterisieren. In situ RAS ermöglicht die Identifizierung der Oberflächenstruktur sowie Zuordnung der entscheidenden Prozessschritte und somit auch Kontrolle über die Oberflächenpräparation, insbesondere der Domänenbildung auf Si(100)- und Ge(100)-Oberflächen. Sowohl Si(100) als auch Ge(100) zeigen eine starke Wechselwirkung mit dem Prozessgas H_2, die letztlich zur Bildung einer Monohydrid-Bedeckung der Oberflächen während der Präparation führt. Detaillierte Analyse verschiedener Si(100)-Oberflächen und Einflüsse der Hauptprozessparameter weisen auf Si-Abtrag während der Präparation unter hohem H_2-Druck hin. Die Erzeugung von Leerstellen auf den Terrassen bewirkt eine kinetisch bedingte Oberflächenstruktur, basierend auf Diffusion von Si-Leerstellen und Atomen. Entsprechend unserer in situ RAS- und Rastertunnelmikroskopie-(STM)-Messungen führt dies auf verkippten Si(100)-Substraten zur Bildung von ungewöhnlichen D_A-Doppelstufen, bei denen die Dimere auf den Terrassen senkrecht zur Stufenkante orientiert sind, während auf exakten Si(100)-Substraten ein schichtweiser Abtragsprozess stattfindet. Präparation unter niedrigem H_2-Druck hingegen führt zu einer Domänen- und Stufenstruktur, die energetisch bedingt ist. Im Gegensatz zur Si(100)-Oberfläche zeigen verkippte Ge(100)-Oberflächen keinen direkten Einfluss der H_2-Prozessgasumgebung auf die Stufenstruktur. Bei der Ge(100)-Oberfläche ist der Einfluss von Gruppe-V-Elemente auf die Stufen- und Domänenbildung sowie auf die nachfolgende III-V-Nukleation entscheidend. In dieser Arbeit wurde der Einfluss von As- und P-Angebot auf die Ge(100)-Oberfläche untersucht. Detaillierte Untersuchungen der As-terminierten Ge(100)-Oberflächen zeigen die Ausbildung von eindomänigen Oberflächen unterschiedlicher Dimerorientierung und deutlich unterschiedlicher Stufenstruktur in Abhängigkeit von Temperatur und As-Quelle. Angebot von P an Ge(100)-Oberflächen durch Heizen in Tertiarybutylphosphin führt zu einer ungeordneten, P-terminierten Ge(100)-Oberfläche, wie Beugung niederenergetischer Elektronen (LEED) zeigt. Den in situ RAS-Messungen zu Folge ist die Ge(100):P-Oberfläche instabiler als die Ge(100):As-Oberfläche. Die nachfolgende III-V-Heteroepitaxie auf Gruppe-IV(100)-Substraten hängt empfindlich von der Domänenausbildung der Si(100) und Ge(100)-Oberflächen ab. Hier wurde RAS als in situ Messmethode zur Kontrolle aller Prozessschritte während der Präparation von Si(100) und Ge(100) in MOCVD-Umgebung etabliert.

Abstract

In the present work, the atomic surface structure of Si(100) and Ge(100) surfaces prepared in metalorganic chemical vapor phase deposition (MOCVD) ambient was studied with regard to subsequent heteroepitaxy of III-V semiconductors on group IV(100) substrates. At the crucial interface between the group-IV substrate and the III-V layer, single-layer steps on the substrate surface induce anti-phase disorder in the epitaxial film. In principle, double-layer stepped substrates can be employed to avoid anti-phase disorder. The MOCVD process gas environment strongly influences the domain and step formation of Si(100) and Ge(100) surfaces. To this end, in situ reflection anisotropy spectroscopy (RAS) and several other ultra-high vacuum-based (UHV) surface sensitive methods were applied to investigate the different surfaces dependent on the preparation. In situ RAS enabled identification of the surface structure and correlation of the crucial process steps, leading to complete control of surface preparation, in particular the domain formation of Si(100) and Ge(100) surfaces. Both the Si(100) and Ge(100) surface strongly interact with H_2 process gas which eventually leads to monohydride termination of the surfaces during preparation. Detailed analysis of Si(100) surfaces and the influence of the main process parameters indicated Si removal during processing in high H_2 pressure ambient. The generation of vacancies on the terraces induces a kinetically driven surface structure based on diffusion of vacancies and Si atoms leading to energetically unexpected step structures. Consequently, anomalous D_A-type double-layer steps, with dimers on the terraces oriented perpendicular to the step edges, are formed on vicinal Si(100) substrates according to in situ RAS and scanning tunneling microscopy (STM) measurements, whereas Si layer-by-layer removal occurs on large terraced substrates. However, processing in low H_2 pressure ambient leads to a step and domain structure which is energetically driven. In contrast to Si(100), H_2 annealed vicinal Ge(100) surfaces indicate no direct influence of the H_2 process gas ambient on the step structure. At the Ge(100) surface, group-V elements strongly influence step and domain formation as well as subsequent III-V nucleation. In this work, the exposure of vicinal Ge(100) substrates to As and P was studied. Detailed characterization of Ge(100):As surfaces showed the formation of single domain surfaces with different majority domain and significantly different step structures depending on temperature and As source, respectively. In contrast, exposure to P by annealing in tertiarybutylphosphine leads to a very disordered P-terminated vicinal Ge(100) surface according to low energy electron diffraction (LEED) measurements. In situ RAS measurements showed that the Ge(100):P surface is less stable compared to the Ge(100):As surfaces. The subsequent III-V heteroepitaxy strongly depends on the step and the domain structure of the group-IV(100) substrate. Here, RAS was established as a powerful in situ method to control all process steps of Si(100) and Ge(100) surface preparation in MOCVD ambient.

Table of Contents

Publications

Major publications:

1. S. Brückner, H. Döscher, P. Kleinschmidt, and T. Hannappel, *"In situ investigation of hydrogen interacting with Si(100)",* Applied Physics Letters, vol. 98, no. 21, p. 211909, 2011.

2. S. Brückner, H. Döscher, P. Kleinschmidt, O. Supplie, A. Dobrich, and T. Hannappel, *"Anomalous double-layer step formation on Si(100) in hydrogen process ambient",* Physical Review B, vol. 86, no. 19, p. 195310, 2012.

3. S. Brückner, P. Kleinschmidt, O. Supplie, H. Döscher, and T. Hannappel, *"Domain-sensitive in situ observation of layer-by-layer removal at Si(100) in H_2 ambient",* New Journal of Physics, vol. 15, no. 11, p. 113049, 2013.

4. S. Brückner, E. Barrigón, O. Supplie, P. Kleinschmidt, A. Dobrich, C. Löbbel, I. Rey-Stolle, H. Döscher, and T. Hannappel, *"Ge(100) surfaces prepared in vapor phase epitaxy process ambient",* physica status solidi (RRL) – Rapid Research Letters, vol. 6, no. 4, pp. 178–180, 2012.

5. S. Brückner, O. Supplie, E. Barrigón, J. Luczak, P. Kleinschmidt, I. Rey-Stolle, H. Döscher, and T. Hannappel, *"In situ control of As dimer orientation on Ge(100) surfaces",* Applied Physics Letters, vol. 101, no. 12, pp. 121602–121602–4, 2012.

6. E. Barrigón, S. Brückner, O. Supplie, P. Kleinschmidt, I. Rey-Stolle, and T. Hannappel, *"Optical in situ monitoring of hydrogen desorption from Ge(100) surfaces",* Applied Physics Letters, vol. 102, no. 11, pp. 111608–111608–4, 2013.

7. E. Barrigón, S. Brückner, O. Supplie, H. Döscher, I. Rey-Stolle, and T. Hannappel, *"In situ study of Ge(100) surfaces with tertiarybutylphosphine supply in vapor phase epitaxy ambient",* Journal of Crystal Growth, vol. 370, pp. 173–176, 2013.

8. O. Supplie, S. Brückner, O. Romanyuk, H. Döscher, P. Kleinschmidt, F. Grosse, and T. Hannappel, *"Atomic scale analysis of the GaP/Si(100) heterointerface by in situ reflection anisotropy spectroscopy and ab initio density functional theory",* submitted, 2013.

9. H. Döscher, A. Dobrich, S. Brückner, P. Kleinschmidt, and T. Hannappel, *"Si(100) surfaces in a hydrogen-based process ambient",* Applied Physics Letters, vol. 97, no. 15, 2010.

10. H. Döscher, S. Brückner, A. Dobrich, C. Höhn, P. Kleinschmidt, and T. Hannappel, *"Surface preparation of Si(100) by thermal oxide removal in a chemical vapor environment,"* Journal of Crystal Growth, vol. 315, no. 1, pp. 10–15, 2011.

11. H. Döscher, S. Brückner, and T. Hannappel, *"Investigation of oxide removal from Si(100) substrates in dependence of the MOVPE process gas ambient",* Journal of Crystal Growth, vol. 318, no. 1, pp. 563–569, 2011.

12. S. Brückner, H. Döscher, T. Hannappel, P. Kleinschmidt, O. Supplie, and A. Dobrich, *"Verfahren zur Oberflächenpräparation von Si(100)-Substraten",* Deutsche Patentanmeldung 102011122749.4, 2013.

Other publications:

13. H. Döscher, O. Supplie, S. Brückner, T. Hannappel, A. Beyer, J. Ohlmann, and K. Volz, *"Indirect in situ characterization of Si(100) substrates at the initial stage of III-V heteroepitaxy",* Journal of Crystal Growth, vol. 315, no. 1, pp. 16–21, 2011.

14. S. Brückner, O. Supplie, E. Barrigon, P. Kleinschmidt, A. Dobrich, I. Rey-Stolle, C. Algora, H. Döscher, and T. Hannappel, *"Si(100) versus Ge(100): Watching the interface formation for the growth of III-V-based solar cells on abundant substrates",* 37th IEEE Photovoltaic Specialists Conference (PVSC), pp. 002538–002542, 2011.

15. S. Brückner, O. Supplie, E. Barrigón, A. Dobrich, J. Luczak, C. Löbbel, I. Rey-Stolle, P. Kleinschmidt, H. Döscher, and T. Hannappel, *"In situ control of Si(100) and Ge(100) surface preparation for the heteroepitaxy of III-V solar cell architectures",* AIP Conference Proceedings, vol. 1477, no. 1, pp. 32–35, 2012.

16. P. Kleinschmidt, H. Döscher, O. Supplie, A. Dobrich, S. Brückner, and T. Hannappel, *"MOVPE Preparation of Double-Layer Stepped Silicon(100) for III-V-on-Silicon Solar Cells",* 27th European Photovoltaic Solar Energy Conference and Exhibition, Frankfurt, pp. 67 – 69, 2012.

17. T. Roesener, H. Döscher, A. Beyer, S. Brückner, V. Klinger, A. Wekkeli, P. Kleinschmidt, C. Jurecka, J. Ohlmann, K. Volz, W. Stolz, T. Hannappel, A. W. Bett, and F. Dimroth, *"MOVPE Growth of III-V Solar Cells on Silicon in 300MM Closed Coupled Showerhead Reactor,"* 25th European Photovoltaic Solar Energy Conference and Exhibition / 5th World Conference on Photovoltaic Energy Conversion, Valencia, Spain, pp. 964 – 968, 2010.

Selected conference contributions:

1. S. Brückner, H. Döscher, A. Dobrich, P. Kleinschmidt, O. Supplie, C. Höhn and T. Hannappel, *"VPE preparation of Si(100) and in situ characterization via RAS"*, oral presentation, 24. DGKK Workshop Epitaxie von III/V Halbleitern, Berlin, 2009.

2. S. Brückner, H. Döscher, A. Dobrich, O. Supplie, P. Kleinschmidt and T. Hannappel, *"In situ characterization of hydrogen termination of VPE prepared Si(100) via RAS"*, 24. DGKK Workshop Epitaxie von III/V Halbleitern, Aachen, 2010.

3. S. Brückner, H. Döscher, A. Dobrich, O. Supplie, P. Kleinschmidt, T. Hannappel, *"Preparation and in situ control of Si(100) substrates for III-V on Si via MOVPE"*, oral presentation, Compound Semiconductor Week 2011 / 23rd International Conference on Indium Phosphide and Related Materials, Berlin, 2011.

4. S. Brückner, E. Barrigón, O. Supplie, J. Luczak, C. Löbbel, P. Kleinschmidt, H. Döscher, T. Hannappel, *"In situ spectroscopy and surface characterization of MOVPE-prepared Ge(100) for III-V heteroepitaxy"* poster presentation, 13th International Conference on the Formation of Semiconductor Surfaces and Interfaces, Prag, Czech Republic, 2011.

5. S. Brückner, E. Barrigón, O. Supplie, J. Luczak, C. Löbbels, P. Kleinschmidt, H. Döscher, T. Hannappel, "*Atomic surface structure of Ge(100) surfaces in vapor phase epitaxy ambient",* poster presentation, 28th European Conference on Surface Science, Wroclaw, Poland, 2011.

6. S. Brückner, O. Supplie, E. Barrigón, A. Dobrich, J. Luczak, C. Löbbel, I. Rey-Stolle, P. Kleinschmidt, H. Döscher, and T. Hannappel, *"In situ control of Si(100) and Ge(100) surface preparation for the heteroepitaxy of III-V solar cell architectures"*,oral presentation, 8th International Conference on Concentrating Photovoltaic Systems, Toledo, Spain, 2012.

7. S. Brückner, O. Supplie, E. Barrigón, J. Luczak, P. Kleinschmidt , H. Döscher, and T. Hannappel, *„In situ control of dimer orientation on Si(100) and Ge(100) surfaces"*, oral presentation, 27. DGKK Workshop Epitaxie von III/V Halbleitern, Erlangen 2012.

8. S. Brückner, E. Barrigón, O. Supplie1, A. Dobrich, J. Luczak, C. Löbbel, I. Rey-Stolle, P. Kleinschmidt, H. Döscher and T. Hannappel, *"In situ control of the Ge(100) surface domain structure for III-V multi-junction solar cells"*, oral presentation, 9. International Conference on Concentrating Photovoltaic Systems, Miyazaki, Japan 2013.

1. Introduction

The worldwide power consumption of mankind is increasing every year due to rising population and living standard [1]. Currently, fossil fuels present the main power sources. Beside limited resources and soon depletion of oil and gas, their consumption is correlated with increasing environmental damage due to exploitation and CO_2 emission. Rising cost and possible power shortages as well as better environmental sustainability demand fast development of renewable energy sources.

While photovoltaic (PV) has the potential of providing a substantial share of electricity worldwide, to date its contributions to electricity generation is still very small due to relatively high energy production costs or low conversion efficiencies of solar cells. In 2012, only 5 % of the net electricity generation was supplied by solar cells in Germany [2]. The theoretical efficiency η of a single-band gap solar cell is set by the Shockley-Queisser limit to be about 30 % [3]. The Shockley-Queisser limit of a single-band gap solar cell can be exceeded by stacking solar cells with different band gaps on top of each other in so-called multi-junction solar cells [4]. III-V semiconductors are ideally suited for monolithic growth of multi-junction solar cells due to their superior optoelectronic properties and tunability of band gaps and lattice constant in a wide range by choice of composition. MOCVD is the established preparation technique for large-scale and high-quality III-V semiconductor growth [5]. Current industry standard is a GaInP/GaAs/Ge(100) triple junction solar cell which achieves device efficiencies over 40% [6].

Higher cell efficiency as well as cheaper production costs drive intensive research for the heteroepitaxial integration of III-V based multi-junction solar cells on Si(100) substrates. Compared to conventional III-V or Ge substrates, silicon exhibits much lower substrate costs and better availability. Si(100) substrates combine very attractive material properties and benefit from extensive research and technological experience, due to their scientific and technological relevance. Integration of III-V semiconductors and Si microelectronics might also enable new high-performance devices [7,8], stimulating intense research activities in this field since the 1980s [9].

1. Introduction

Very low defect densities are required for high quality devices in the subsequently grown III-V films. However, the transition from Si(100) to III-V semiconductors presents a difficult challenge due to lattice mismatch, different thermal expansion coefficients, and problems of polar-on-non-polar heteroepitaxy [10]. For the latter, the interface and surface formation plays a crucial role during III-V-on-IV(100) heteroepitaxy [9]: Formation of single-domain substrate surfaces with double-layer steps is essential to avoid so-called APDs, which arise depending on the step structure of the (100) substrate surface and are associated with planar defects in the III-V material.

With a view to III-V-on-silicon epitaxy, we use a MOCVD system with H_2 as process gas at a range from a few millibars to atmospheric pressure. However, most knowledge about Si(100) surfaces has been obtained from studies based on preparation in ultra-high vacuum (UHV), where standard surface science methods can easily be applied. Si(100) preparation in H_2 ambient differs considerably [11–14] from well established UHV preparation [15–19]. On the other hand, Ge(100) is the standard substrate for multi-junction solar cells, but little is known about surface preparation and formation of the crucial heterointerface in MOCVD ambient. Processes in MOCVD ambient are very complex due to competition between energetic and kinetic processes, interaction of process gas and sample surface, presence of precursors, as well as III-V residuals in the reactor from previous runs. Since the process gas ambient limits access to UHV-based surface science techniques, in situ characterization of the sample surfaces is required to understand surface preparation in MOCVD ambient. Reflection anisotropy spectroscopy (RAS) is ideally suited for in situ monitoring of sample surfaces during MOCVD processing [20,21]. However, the origin of RAS signatures is very complex and requires careful analysis for identification [22–24,24–26].

The goal of this work is to study the influences of the MOCVD process parameters on the atomic surface structure of Si(100) and Ge(100) substrates, enabling the preparation of single-domain surfaces for subsequent III-V heteroepitaxy. In particular, the influence of the main process parameters such as temperature, type of process gas and pressure, and precursors on the step and domain formation was analyzed. Correlation of in situ RA spectra to results from other surface science techniques allowed us to establish RAS

signals of Si(100) and Ge(100) surfaces for in situ surface characterization during MOCVD preparation. RAS signals of Si(100) surfaces are already relatively well understood due to numerous experimental and theoretical studies [24,25,27–35]. However, in the case of Ge(100) only scarce reports in literature exist [36,37].

Applying in situ RAS and UHV-based surface sensitive methods, we investigated the removal of oxides and other contamination from the substrates, the interaction between process gas and substrate surface, the influence of H_2 ambient on the step and domain formation, and the influence of As and P exposure on the surface structure of Ge(100). In situ RAS enabled control of domain formation by adjustment of the relevant process parameters.

2. Theoretical and experimental background

In this section, the theoretical background of multi-junction solar cells, III-V-on-IV(100), and the Si(100) and Ge(100) surfaces is discussed. Further, the experimental methods of this work and the basic MOCVD processes are presented. As a starting point for this work, state-of-the-art Si(100) preparation in MOCVD ambient and RAS results of Si(100) and Ge(100) surfaces are summarized.

2.1 Multi-junction solar cells

Solar cells enable direct conversion of sunlight into electrical energy. They consist of semiconductor material with a specific band gap E_g and a p-n-junction. Only the photons with energy larger than the band gap are absorbed leading to generation of electron-hole pairs. The electron-hole pairs are separated by the electric field at the p-n-junction resulting in a photoelectric voltage between front- and back-contact of the solar cell. Principally, the conversion efficiency η of the incoming radiation into electrical energy depends on the band gap of the solar cell material: Photons with energy $\hbar\omega < E_g$ cannot be absorbed and will be transmitted through the material (transmission losses). Only the photons with $\hbar\omega = E_g$ are ideally converted, since the photon energy larger than the band gap $\Delta E = \hbar\omega - E_g$ is converted into heat via phonon interactions in the crystal lattice within few picoseconds (thermalization losses). Accordingly, Shockley and Queisser calculated the conversion efficiency η of a single-junction solar cell without concentration to be limited at about 30 % [3].

Multi-junction solar cells consist of a combination of solar cells with different band gaps in serial connection which enables efficiencies beyond the Shockley-Queisser limit by reduction of thermalization and transmission losses. Fig. 1 illustrates the better exploitation of the solar spectrum by a GaInP/GaInP/Ge triple junction solar cell.

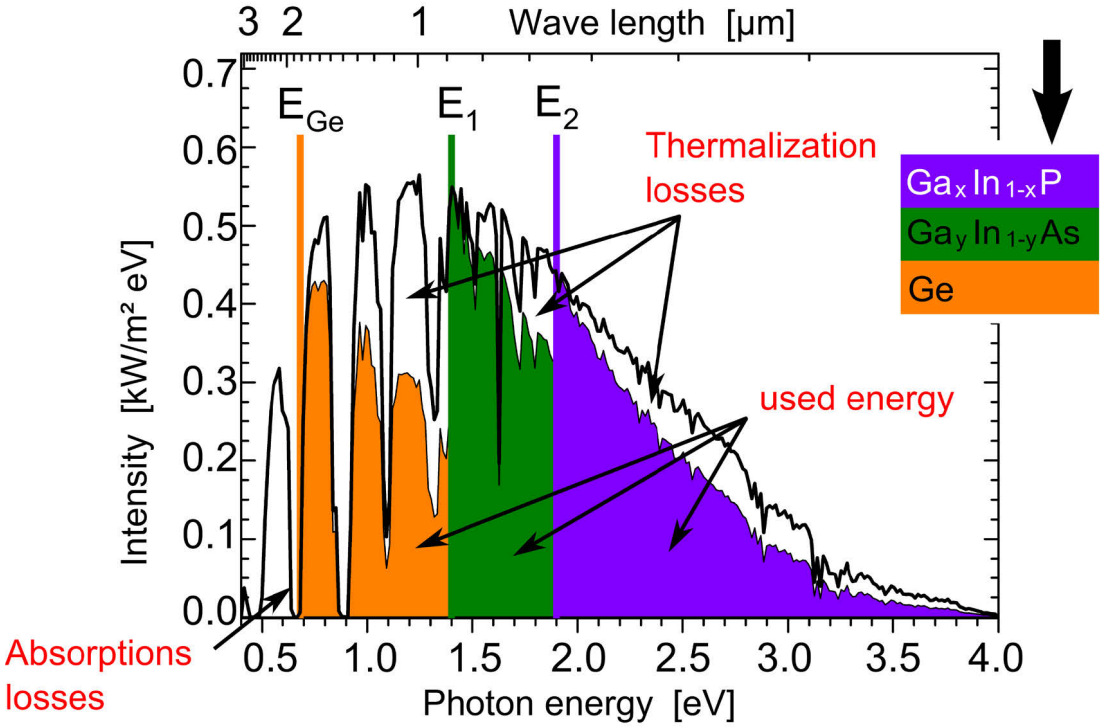

Fig. 1: Standard solar spectrum ASTM G-173-03 for terrestrial irradiance at an effective air mass of 1.5 atmospheres and its electrical yield by a triple junction solar cell based on the combination of GaInP/GaInP/Ge (colored areas) considering absorption and thermalization losses. The colored lines refer to the band gaps of the different materials indicating their absorption edges (after [38]).

While early III-V tandem cells consisted of GaInP top cells grown on GaAs bottom cells [4], state-of-the-art triple junction solar cells are fabricated on Ge(100) substrates which serve as a low band gap bottom cell below a GaInP/GaAs tandem cell. Low defect densities in the epitaxially grown films as well as ideal band gap combinations are crucial for high performance solar cell devices. Hence, III-V semiconductors exhibit ideal properties for realization of multi-junction solar cells, since ternary or higher order compounds enable band gap tuning as well as lattice matching over a wide range. The plot of band gap over lattice constant of III-V semiconductors and elemental semiconductor (Fig. 2) clearly shows the potentials of III-Vs and challenges of the heteroepitaxy on group IV substrates.

Current matching of the sub-cells limits the efficiency of the whole solar cell, due to serial connection of the individual sub-cells. A further sub-cell with a band gap of 1.0 eV

is required to improve current matching in current triple-junction cells [39], which is not available on the lattice constant of Ge and GaAs. An alternative low-band gap tandem could be realized on InP(100) substrates [40], which exhibits disadvantageous high material prices and availability. Therefore, Si(100) substrates present another option as alternative substrate. However, a change of the lattice constant is required to reach the composition regime of classical III-V compounds with direct band gap.

So far, multi-junction solar cells were mainly established to power satellites in space due to their high efficiency and production costs. Currently, progress in the development of concentrator systems (concentrator photovoltaic – CPV) makes terrestrial application of multi-junction solar cells competitive to other techniques [6]. Here, lenses or mirrors focus the sunlight on a smaller solar cell area, and a tracking system follows the course of the sun. Typically, concentrations are in the range of 500 to 1000 suns.

2.2 III-V-on-IV(100) heteroepitaxy

Heteroepitaxial growth of III-V semiconductors on Si(100) and Ge(100) substrates is technologically highly desired. III-V semiconductors provide excellent material properties for high-efficiency optoelectronic devices, but suffer from high material costs. Group-IV(100) substrates present cheaper substrates for applications such as multi-junction solar cells [41,42], and lasers [8]. Furthermore, III-V/Si heteroepitaxy enables the monolithic integration of III-V optoelectronics with well established Si microelectronics.

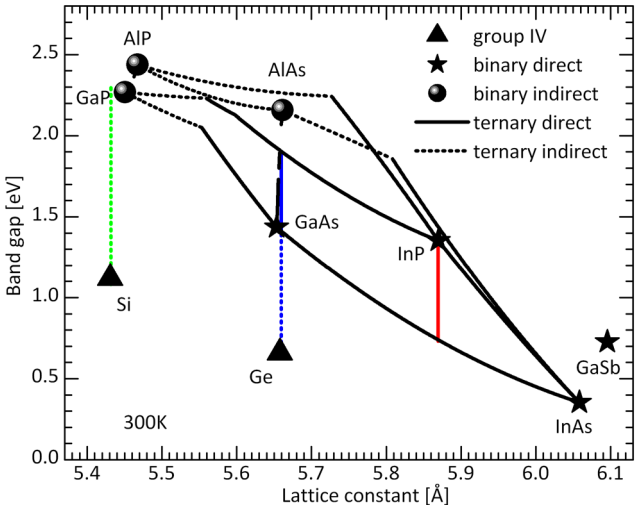

Fig. 2: Band gap over lattice constant plot for III-V semiconductors and their compounds, as well as group IV semiconductors. Solid and dotted lines present ternary III-V compounds with direct and indirect band gap, respectively. Colored lines represent lattice matched heterostructure on Si, Ge, GaAs, and InP substrates relevant for solar cells.

The main challenges of III-V-on-IV(100) heteroepitaxy are related to the crucial differences in the material parameters and formation of the heterointerface:

- lattice mismatch: different lattice constant of substrate and film result in tensile or compressive lattice strain. Misfit dislocations form to relieve stress in the epitaxially grown films [43].

- different thermal expansion coefficient: typical growth temperatures are between 670 and 970 K; after growth, strain may occur when the layers are cooled down and contract differently, resulting in crack formation [44].

- interdiffusion at the heterointerface may induce cross-doping in the substrate or the epitaxial films, e.g. Ge outdiffusion into GaAs [45,46].

- polar-on-non-polar heteroepitaxy: the heterointerface induces problems such as charge neutrality or anti-phase domains [9].

GaP (a_{GaP} = 5.45 Å) exhibits a small lattice mismatch to Si (a_{Si} = 5.43 Å) of only 0.37 %. Thin GaP films grow pseudomorphically on Si(100) substrates below the critical thickness resulting in GaP/Si(100) quasi-substrates [47]. Successive change of the lattice constant in subsequently grown III-V buffer layers by changing the ternary material composition, so-called grading, enables access to III-V compounds that are relevant for photovoltaic application. Grading layers are intended to relieve the strain and reduce the impact of defects such as misfit dislocations or threading dislocations [48–50]. On the other hand the novel material system of dilute nitrides (GaIn)(NAsPSb), which features incorporation of small amounts of N (<5%), enables lattice matched growth on Si(100) and a direct band gap [8,51–53]. In case of Ge(100), (In)GaAs and GaInP layers can be grown lattice matched.

2.2.1 Anti-phase domains

One of the most important defects to avoid during III-V/IV(100) heteroepitaxy are anti-phase domains (APDs) that originate from the polar-on-non-polar heterointerface [9]. Si and Ge crystallize in the diamond structure which equals two interpenetrating fcc sublattices (see Fig. 3). Each atom is connected to its four nearest neighbors by four tetrahedral bonds that differ in spatial orientation for the two sublattices. Both sublattices are occupied by the same type of atom species. In contrast, III-V semiconductors exhibit a zincblende structure, where the two sublattices are occupied by different atomic species. Accordingly, the symmetry in the zincblende structure is reduced compared to the diamond structure. In a single-domain crystal, only one sublattice orientation exists.

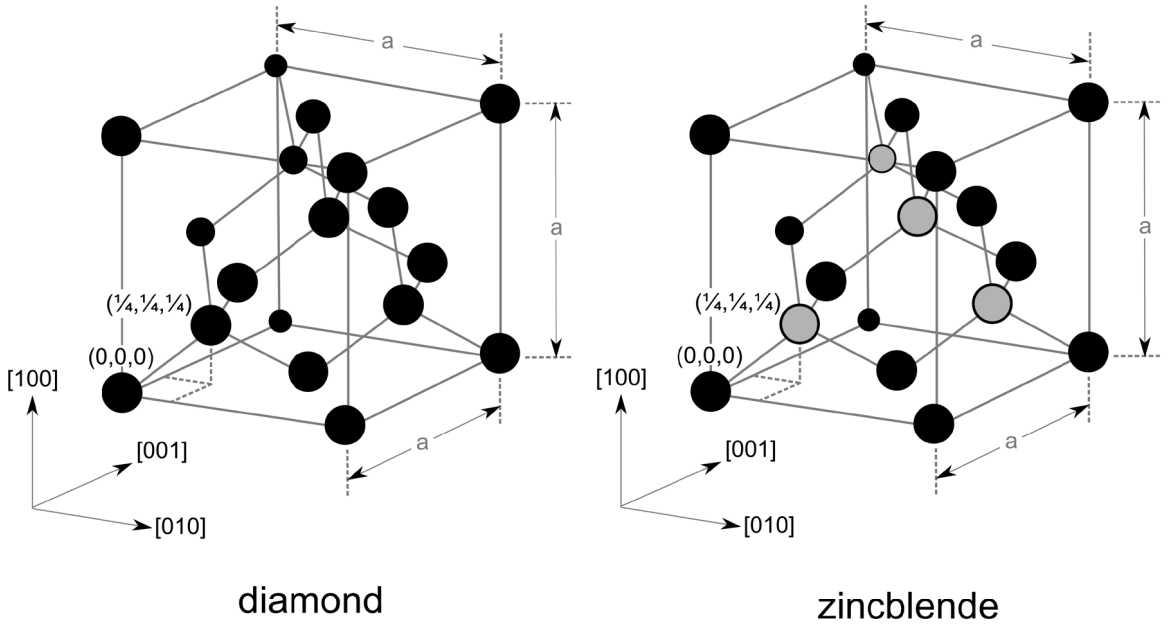

Fig. 3: 3D sketch of the diamond and zincblende lattice structure.

Any real Si(100) and Ge(100) surface exhibits steps. In case of single-layer steps (or an odd number height) undesired III-III or V-V bonds are formed at the step edges during III-V film growth assuming the same element as first monolayer on all terraces (Fig. 4, right side). These bonds represent electrically charged defects, so-called anti-phase boundaries (APB). APBs propagate through the III-V crystal during growth separating anti-phase domains (APDs). However, APDs can be avoided by double-layer (or even numbered) steps on the group-IV(100) substrate where the sublattice orientation in the III-V film is preserved (Fig. 4, left side).

Hence, formation of double-layer steps on the group-IV(100) substrates is a crucial prerequisite for subsequent APD-free III-V heteroepitaxy. Double-layer step formation is very well studied in UHV-based preparation ambient. However, much less is known during preparation in MOCVD where the presence of a process gas complicates access to standard surface science techniques. Step formation processes will be discussed in section 2.3.4.

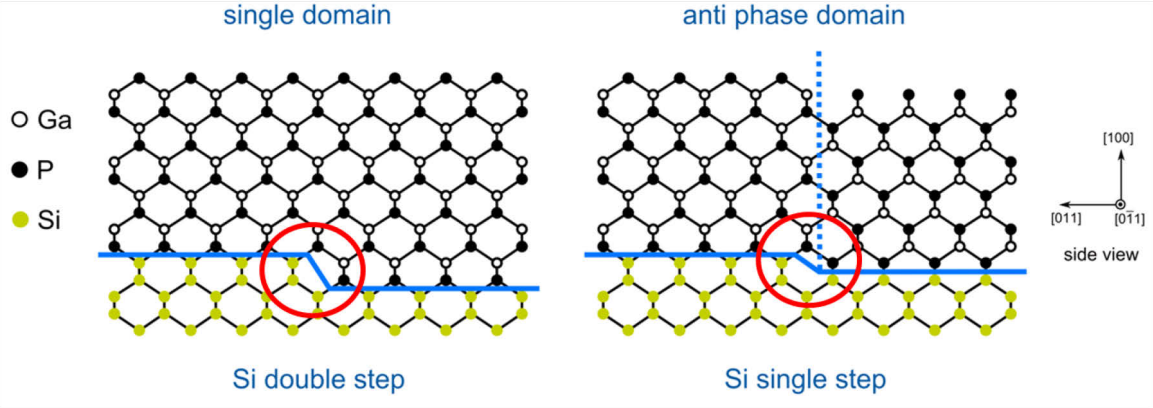

Fig. 4: Schematic diagram of APD formation. At double-layer steps, the sublattice orientation remains, while single-layer steps induce anti-phase boundaries (blue dotted line).

2.3 Si(100) and Ge(100) surfaces

While the first transistor was made from germanium [54], nowadays, the silicon based microelectronic industry prevails due to the success of CMOS (complementary metal oxide semiconductor) technology. For most applications controlling the microscopic Si(100) and Ge(100) surface structure is crucial due to the influence of defects as well as of step structures. Accordingly, Si(100) belongs to the most frequently studied surfaces, due to its unequalled relevance in microelectronics. There is a renewed interest in the Ge(100) surface as substrate for III-V semiconductor solar-cells [42], as well as for applications in microelectronics [55], and nanotechnology [56]. Both Si and Ge are group IV elements and consequently exhibit four valence electrons. Both elements crystallize in the diamond structure due to sp^3 hybrid orbital formation (see Fig. 3). The atoms form covalent bondings where every atom is surrounded by for nearest neighbors in a tetrahedral configuration. The lattice constants are 5.431 Å for Si and 5.658 Å for Ge. Pure Si and Ge are intrinsic semiconductors with indirect band gaps at 1.12 eV and 0.66 eV, and direct band gaps at 3.4 eV and 0.8 eV, respectively.

The following section reports on the Si(100) and Ge(100) surface regarding surface reconstruction, hydrogen termination, as well as step and domain formation.

2.3.1 Surface properties

Regarding surface properties, the Si(100) and the Ge(100) surface exhibit a lot of similarities. Both surfaces reconstruct by forming bonds between pairs of neighboring surface atoms (dimerization). In the case of Si(100), Schlier and Fansworth [57] first discovered the (2×1) surface reconstruction by LEED measurements. In comparison to the unreconstructed surface the reconstructed surface reduces the number of dangling bonds from two to one. Hereby, two neighboring surface atoms move out of equilibrium position to bond with each other. The resulting dimers are arrayed in rows parallel to the

[011] direction (see Fig. 5). The Si dimers exhibit a bond length of 2.2-2.4 Å [58,59] which is similar to the Si-Si distance in the bulk crystal. Dimerization induces an anisotropic surface stress tensor with compressive stress along dimer row direction and tensile stress perpendicular to the dimer rows. The stress of the crystal structure extends into the fifth layer [60].

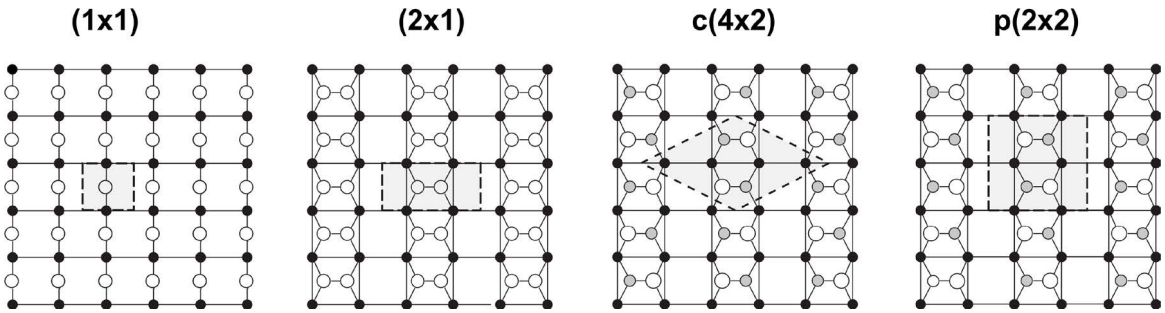

Fig. 5: Ball and stick model of the Si(100) and Ge(100) surface: (1×1) ideal unreconstructed surface, (2×1) reconstruction with symmetric dimers, c(4×2) and p(2×2) reconstruction due to dimer buckling. Grey areas represent the unit cell of the surface reconstruction (after Zandvliet [61]).

On Si(100), the dimers are buckled by about 19° [62,63] to further reduce the surface energy (see Fig. 6). The formation of antisymmetric dimers is favored by approximately 0.14 eV per dimer compared to the symmetrical configuration, corresponding to the formation of a c(4×2) and a p(2×2) surface reconstruction, respectively (see Fig. 5). On Si(100), the dimers oscillate at room temperature resulting in the observed (2×1) reconstruction in STM. Low temperature STM evidenced the presence of buckled dimers [64–66]. In contrast, on Ge(100) dimer buckling is present at ambient temperature. Stripes of (2×1), c(4×2) and p(2×2) surface reconstructions coexist on very clean surfaces [61].

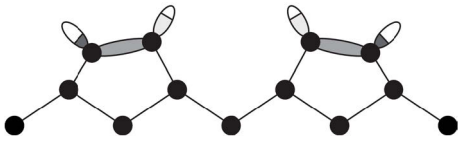

Fig. 6: Side view of two buckled dimers (after Zandvliet [61]).

The induced anisotropic surface stress tensor due to dimerization can be reduced by formation of surface reconstruction domains with mutually perpendicular dimer orientation. The domains are separated by monoatomic steps (step height $a_0/4$ = 1.36 Å

for Si(100)), leading to a balanced distribution of (2×1) and (1×2) domains on nearly exact Si(100) surfaces [67].

2.3.2 Hydrogen on Si(100) and Ge(100)

Hydrogen termination on Si(100) leads to passivation of the reactive clean surface, reducing its susceptibility to oxidation and other contamination. The hydrogenated Si(100) surface prepared in UHV by application of atomic hydrogen exhibits three different surface reconstructions with increasing hydrogen chemical potential (see Fig. 7): a monohydride (2×1), a mixed (3×1), and a dihydride (1×1) phase [68].

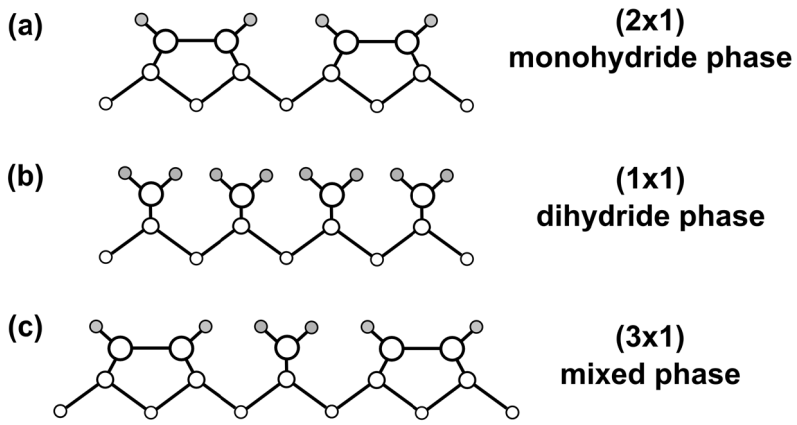

Fig. 7: Side view of the different surface reconstructions induced by adsorption of atomic hydrogen (after [69]).

In case of the monohydride phase, the number of hydrogen atoms equals the number of Si surface atoms, since H atoms saturate the remaining dangling bonds of the Si dimers. As a consequence of the saturation of the dangling bonds, interaction between them is suppressed. Hence, dimer buckling does not occur on the monohydride terminated surface leading to a (2×1) surface reconstruction. Monohydride termination occurs for hydrogen coverage $\theta \leq 1$ ML by exposure to moderate amounts of atomic hydrogen, but exposure at room temperature does not result in a well-ordered monohydride terminated (2×1) Si(100) surface due to possible formation of higher hydrides. Hydrogenation exceeding coverages larger than 1 ML result in breaking of the Si-Si bonds of the dimers and

saturation of the second dangling bond with hydrogen for temperatures below 570 K. A mixed (3×1) (θ = 1.5 ML) or a dihydride (1×1) surface reconstruction (θ = 2 ML) forms depending on temperature and hydrogen flux. For temperature above 570 K a well-ordered (2×1) monohydride surface reconstruction is formed on Si(100) [68,70–72].

FTIR measurements showed that desorption of hydrogen occurs from the dihydride surface for T = 640 – 700 K while monohydrides termination is stable for T = 720 – 800 K [73]. Hydrogen desorbs in a recombinative reaction [74]. According to laser-induced thermal desorption (LITD) studies, recombinative desorption kinetics of hydrogen from the monohydride phase follow a rate law of first order over a wide range of temperatures and coverages [75].

Kolasinky et al. [76] studied the dissociative adsorption kinetics of molecular hydrogen. Contrary to atomic hydrogen, molecular hydrogen does not adsorb at room temperature due to its extremely small sticking coefficient (S_0). S_0 increases with both molecular energy and substrate temperature. The adsorption of molecular hydrogen is activated and involves lattice vibrational excitations.

Both dissociative adsorption and recombinative desorption of H_2 on Si(100) surface is related to the dangling bonds of two neighboring dimers [77]. Since preadsorption of atomic hydrogen as well as thermal excitation of H_2 gas significantly change the adsorption barrier, surface coverage and temperature strongly influence the reactivity. Additionally, phonon excitation of the silicon substrate plays a crucial role.

Annealing of Si(100) in H_2 ambient results in monohydride termination as shown in Refs. [78] and [79]. Komeda and Kumagai [80] described a model for the hydrogen coverage (θ) of Si(100) surfaces during annealing in H_2. H coverage is a function of pressure $p_{(H2)}$ and substrate temperature. It is determined by the balance between the hydrogen adsorption and desorption rate at the Si surface. The change of the hydrogen coverage with time $\theta(t)$ can be written as:

$$\frac{\mathrm{d}\theta(t)}{\mathrm{d}t} = R_{\mathrm{ads}} - R_{\mathrm{des}}, \qquad \textbf{Eq. 1}$$

where R_{ads} and R_{des} correspond to the adsorption and desorption rate, respectively. R_{ads} can be denoted by the following formula:

$$R_{\mathrm{ads}} = S_0(T) f[\theta(t)] F, \qquad \textbf{Eq. 2}$$

where $S_0(T)$ is the sticking coefficient which depends on the substrate temperature T_s and gas temperature T_g. $f[\theta(t)]$ represents the coverage dependence of the adsorption $(1-\theta)$. F is the flux of impinging H_2 molecules. The temperature dependence of S_0 is described in detail by Kolasinky et al. [76].

The desorption rate corresponds to

$$R_{\mathrm{des}} = \theta(t)^n A_{\mathrm{d}} \exp\left(-\frac{E_{\mathrm{d}}}{k_{\mathrm{B}} T}\right), \qquad \textbf{Eq. 3}$$

where n represents the reaction order (for first-order kinetics $n = 1$), A_{d} the Arrhenius prefactor, E_{d} the desorption activation energy, and k_{b} Boltzmann's constant [80].

Applying parameters identical to Ref. [80], we calculated the hydrogen coverage in dependence of the substrate temperature We assumed equilibrium conditions regarding surface and gas phase temperature ($T_s = T_g$) as well as regarding hydrogen coverage ($t \rightarrow \infty$). The results are plotted in Fig. 26 (see section 3.1.1.2). It clearly depicts how the balance between hydrogen adsorption and desorption shifts with hydrogen pressure p_{H2}.

The interaction between hydrogen and the Ge(100) surface is quite similar to the Si(100) surface but much less studied. The Ge(100) surface also forms a (2×1) monohydride phase after exposure to atomic H. However, dihydrides are very instable, which inhibits a large-scale formation of the mixed (3×1) phase and the dihydride (1×1) phase at room temperature [81]. The monohydride termination of Ge(100) is unstable when exposed to

ambient air. Rapid contamination by hydrocarbon and GeC formation occurs, but immediate oxidation is suppressed [82]. H desorption kinetics has been studied by temperature-programmed desorption (TPD) [83], STM [84], and laser-induced desorption (LID) [85] analysis. Hydrogen desorbs from the Ge(100) surface following first order kinetics [83–85] with activation energies E_d in the range of 1.65 to 1.82 eV and pre-exponential factors ν_d in the range of $2.7 \cdot 10^{13}$ to $2.0 \cdot 10^{15}$ s^{-1}, see Refs. [84] and [85]. There are no reports in literature about the interaction of H_2 and Ge(100) surfaces.

2.3.3 Vicinal surfaces

STM measurements enabled studies of the atomic step structure showing single-layer and double-layer steps on the clean Si(100) and Ge(100) surface. According to Chadi [15] four different step types can be distinguished (see Fig. 8(a)): single- (S) and double- (D) layer steps with dimer orientation perpendicular (A-type) or parallel (B-type) to the step edge on the upper terrace. Additionally, step reconstruction may occur at the edges. The S_B-type step edge exhibits two possible configurations, a rebonded and a non-rebonded S_B step. Since the rebonded S_B step features less dangling bonds, it is energetically favored over the non-rebonded S_B step [15].

Substrates with small offcut exhibit mainly single-layer steps on both Si(100) and Ge(100), whereas substrates with higher offcut show double-layer steps ($\geq$ 2.5° for Si(100) and $>$ 5° for Ge(100)) [16,61]. Double-layer steps on Si(100) and Ge(100) surfaces were observed first in 1987 by Wierenga et al.[86,87]. Vicinal Si(100) and Ge(100) substrates with 6° offcut in [011] direction exhibited exclusively D_B double-layer steps. According to total energy calculations of Chadi [15], D_B double-layer steps are considered to be energetically favorable over the combination of S_A and S_B single-layer steps, while D_A double-layer steps are considered least favorable. In practice, D_B steps are obtained on vicinal Si(100) and Ge(100) surfaces simply by annealing in UHV [16,88,89]. In contrast, scarce reports on D_A double-layer steps are based on application

of either mechanical stress [90], direct current (electromigration) [91], or Xe-ion bombardment [92,93].

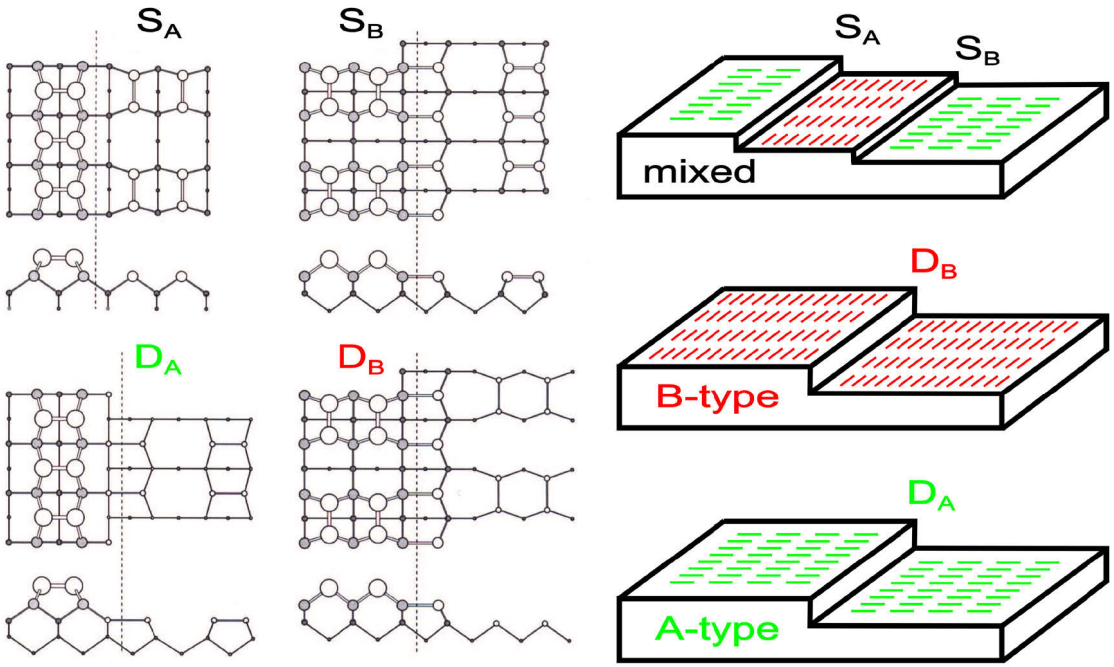

Fig. 8: (a) Ball and stick model of S_A-, S_B-, D_A-, and D_B-type steps of the Si(100) surface according to Chadi [15]. (b) Schematic diagram showing relation between step types and dimer orientation.

The schematic diagrams in Fig. 8(b) show the relation between step type and dimer orientation. While single-layer steps are associated with alternating dimer orientations inducing a two-domain surface, double-layer steps preserve the dimer orientation on adjacent terraces resulting in single-domain surfaces.

2.3.4 Step formation

For understanding the step formation under MOCVD conditions, energetics as well as kinetics on the Si(100) surface have to be regarded. On the one hand, a surface tends to minimize the total surface energy by formation of the energetically most favorable step structure. On the other hand, kinetic processes such as hydrogen adsorption and

desorption, Si removal or growth, diffusion of Si adatoms or vacancies, and annihilation of vacancies or attachments of adatoms at the step edges play a crucial role.

2.3.4.1 Influence of hydrogen

Hydrogen strongly affects the step structure on Si(100) surfaces. In contrast to the situation at the clean Si(100) surface, theoretical studies of the step formation energies do not predict any preference for double-layer steps in the range of the (2×1) monohydride reconstruction [18,19]. The hydrogen chemical potential μ_H influences the step energetics. For a wide range of μ_H the nonrebonded step structure is more stable than the rebonded one [18]. According to first-principle calculations of step formation energies, step formation requires energy on the (2×1) reconstructed surface while steps form exothermally on the (1×1) surface. As a result surface roughening on Si(100) surfaces occurs at high H chemical potentials at the dihydride surface[19].

Laracuente and Whitman [17] studied the equilibrium step structures for monohydride terminated Si(100) surface with different misorientations, which were prepared in UHV under exposure to atomic hydrogen, by STM. They confirmed the preference for single layer steps over double layer steps at misorientations up to 7° in the [011] direction.

There are contradictory reports about the step structure of Si(100) surfaces prepared in (MO)CVD ambient. Initial LEED and STM studies of our group [94] showed similar results to UHV studies for Si(100) substrates with 0.1°, 2° and 6° off-cut in [011] direction after annealing in H_2 ambient (see section 2.5.2). On the substrates with lower misorientation a single layer stepped two-domain (2×1)/(1×2) reconstructed surface was found. On 6° offcut substrates STM measurements showed mainly double-layer steps and but also some odd-numbered step heights (more details see section 2.5.2).

However, Kitahara and Ueda [95] observed a retreat of S_A steps after annealing Si(100) 2° offcut substrates in H_2 ambient. Refs. [12] and [14] reported on a tendency towards double-layer steps for nearly exact Si(100) substrates after MOCVD preparation which included homoepitaxial buffer growth and high-temperature annealing in H_2. Their AFM

measurement did not allow specification of the step type but showed a preference for double layer steps in the [011] direction. In Refs. [11,13], we reported on the influence of the final cooling sequence on the domain distribution during CVD-processing of Si(100) 2° substrates that was reflected in polarized FTIR spectra as well as in LEED patterns. Quantitative analysis of the FTIR data revealed a minority domain content of only 18.5 % for the CVD-prepared Si(100) sample, which contradicts established UHV results [16] (see details in section 2.5.3).

2.3.4.2 Si removal and growth processes

Growth and diffusion processes significantly influence the step structure of Si(100) surfaces. Roland and Gilmer [96] studied Si adatom diffusion and the role of steps as binding sites during homoepitaxial growth theoretically. Growth takes place more readily at the step edges than at the flat surface. In agreement with experimental observations [97], impinging adatoms rather bond at the end of dimer rows than on the sides. This results in anisotropic expansion of the terraces preferentially at the step edges of S_B type steps and a prevalence of the B-type terrace [96].

The opposite behavior is observed under conditions where Si removal occurs from the Si(100) surface. Bedrossian and Klitsner [92,98] as well as Swartzentruber et al. [93] studied the surface structure of Si(100) surfaces after Si removal by Xe-ion bombardment. Ion bombardment generated missing dimer vacancies in the Si layer. In analogy to Si adatoms, these vacancies exhibit an anisotropic diffusion behavior, i.e. faster diffusion along the dimer rows than perpendicular [99]. The generated surface vacancies preferentially annihilate at the end of dimer rows. Consequently, vacancies coalesce to elongated vacancy islands oriented parallel to the dimer rows of the Si terrace [92,99]. In case vacancy diffusion is small compared to the terrace width, formation processes of vacancy islands induce a layer-by-layer removal process, as indicated by RHEED measurements during ion bombardment [98]. If the vacancy diffusion length is large compared to the width of the Si terrace, annihilation of the vacancies at the B-type step edges occurs, resulting in a retreat of the B-type terraces and formation of a D_A

stepped surface [92]. The single-domain A-type surface prepared by ion bombardment is not an equilibrium structure and contradicts energetic considerations.

Si removal and growth plays a crucial role during preparation of Si(100) in H_2 ambient. Si etching in H_2 ambient is reported for T = 1170 – 1600 K by formation of SiH_4 and SiH_2 [100–102]. Additionally these processes are strongly affected by the hydrogen coverage present at the Si(100) surface. Nara et al. showed that the mobility of adatoms is reduced at the monohydride-terminated Si(100) surface compared to that on the bare Si surface [103].

The above described processes at the Si(100) surface are crucial for understanding the step formation processes in MOCVD ambient, which will be discussed later in this work.

2.3.4.3 Influence of group-V elements

Group III and group V elements also have a great impact on the step and domain structure of Si(100) and Ge(100) surfaces. In the following, the influence of As and P on the Ge(100) surface is discussed. Regarding As termination, there are again many similarities between Si(100) and Ge(100).

According to UHV results [87], the clean vicinal Ge(100) surface with 6° offcut tends to form a single-domain surface with D_B double-layer steps. III-V heteroepitaxy on Ge(100) substrates often starts with exposure to group-V precursors. While GaAs is usually grown on As terminated Ge(100) [104–107], GaInP is grown on P terminated Ge(100) [108,109]. The influence of As on the Ge(100) surface is studied more widely in literature [110–112] than the influence of P [108].

The surface structure of vicinal Ge(100) strongly changes with exposure to As [110–112] which has important consequences for GaAs nucleation [104–107]. The most relevant properties of Ge(100):As surfaces refer to the preferential As dimer orientation, the height of steps, and the atomic configuration at the step edges [110,111]. In analogy to Si(100) [113], As atoms adsorb on the Ge(100) surface and form As dimers, oriented either

parallel or perpendicular to the step edges. Here, we denote terraces of type A with (1×2) reconstruction as Ge(100):As_A (with As dimers aligned perpendicular to the step edges), and terraces of type B with (2×1) reconstruction as Ge(100):As_B (As dimers parallel to the step edges), as depicted in Fig. 9. Ge(100):As_A can be regarded as a surface where As is adsorbed in an additive fashion, whereas As may adsorb by displacing Si dimers at a Ge(100):As_B surface. According to Refs. [114–117], the displacing As_B adsorption leads to a lower surface energy configuration on Si(100), while the additive As_A adsorption represents a metastable structure. However, kinetics as well as energetics have to be considered to understand the step and domain formation. Ref. [113] highlights the impact of the preparation route on the resulting domain and step structure on vicinal Si(100):As. STM measurements revealed the dependence of dimer orientation on the timing of arsenic exposure and subsequent substrate annealing sequence, as well as on actual values of the As_4 flux and the exposure temperature.

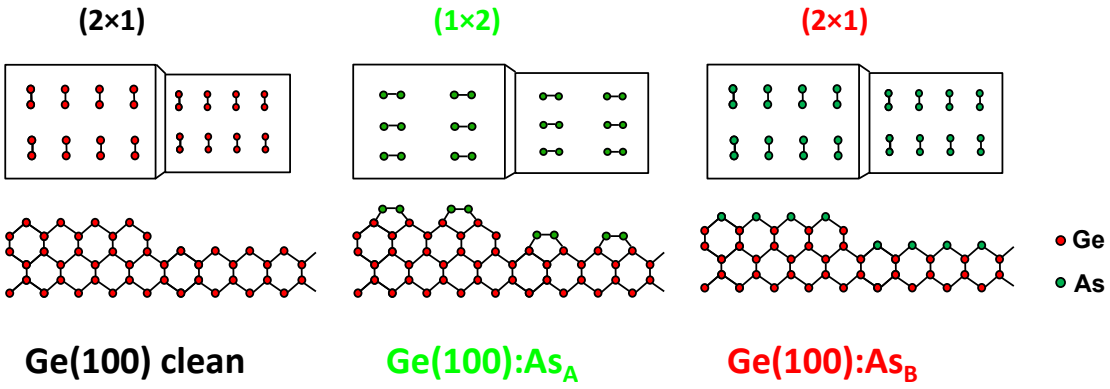

Fig. 9: Schematic drawing to illustrate the effect on As adsorption on the vicinal Ge(100) surface

McMahon and Olson [110,111] studied the arsenic-exposed vicinal Ge(100) surface prepared in MOCVD environment in great detail by STM. As passivates the Ge(100) substrate leaving the surface chemically unreactive, so the surface remains clean in UHV for some days. Process temperature, source, and partial pressure of arsenic are important parameters for the Ge(100):As surface preparation. In MOCVD ambient, As can be supplied either directly via precursors such as AsH_3 and tertiary-butyl-arsenic (TBAs), or indirectly as background As_4 originating from the reactor environment covered by As

precursor fragments. The sublimation temperature of solid arsenic is 878 K, however, As compounds already volatilize from GaAs at lower temperatures [104]. At typical annealing temperatures around 920 K the presence of background As_4 has to be considered to understand the step formation. AsH_3 annealing may induce significant step bunching and ridge formation due to etching of the Ge surface dependent on temperature and partial pressure [110,111]. Most As/Ge steps are reconstructed resulting in a variety of different step reconstructions, which can be separated into two types, “single-row”, and “double-row” steps. The formation of the step reconstruction depends on the sample preparation, too. Annealing at temperatures around 920 K in either AsH_3 or background As_4 result in (2×1) and (1×2) majority domain Ge(100):As surfaces, respectively, which deviate in step structure.

GaAs growth studies on Ge(100) [104], [106] indirectly showed the crucial influence of the surface preparation by As exposure on the quality of the subsequent GaAs nucleation layer. Ting and Fitzgerald [104] revealed a 90° sublattice rotation of the GaAs film grown on differently prepared Ge(100) surfaces in MOCVD ambient. Based on literature they discussed the sublattice rotation as an effect of the initial Ge(100):As domain structure, i.e. nucleation of GaAs on Ge(100):As_A and Ge(100):As_B. The formation of single domain Ge(100):As substrates significantly reduced the APD content and, as a consequence, the parallel resistance in subsequently grown GaAs solar cells [106].

P termination of the Ge surface should be obtained prior to nucleation for state-of-the-art GaInP on Ge heteroepitaxy in MOCVD [108] and [109]. Phosphine (PH_3) and tertiarybutylphosphine (TBP) are the two main P precursors used in MOCVD systems. Annealing under PH_3 at 573–720 K in low pressure CVD systems leads to P termination of Ge(100) surfaces by one atomic layer [118]. LEED analysis of a P-terminated Ge(100) surface with 2° offcut prepared by PH_3 exposure in MOCVD ambient shows a (9×2) surface reconstruction [108]. In contrast to AsH_3, PH_3 does not etch the Ge surface [119]. The influence of annealing under TBP on the Ge(100) surface is still unclear.

2.4 Experimental background

2.4.1 Metalorganic chemical vapor deposition

Metalorganic chemical vapor deposition (MOCVD) represents a flexible deposition technique for thin layers in the range of a few nanometers up to several micrometers. A great advantage of MOCVD is the ability to use a large variety of elements in the form of specially synthesized molecules, so-called precursors, for layer growth. In principle, precursors are transported by a highly purified carrier gas into the reactor at temperatures from 670 to 1200 K, where they decompose thermally and the elements are deposited on the heated substrate surface. Complex processes lead to growth of pure material layers which requires suitable process parameters. MOCVD is used for growth of metals (Al, Cu, FeTi), oxide compounds for optical coatings, sensors, and superconductors, as well as a large variety of semiconductor materials. For the growth of semiconductor materials, the term metalorganic vapor phase epitaxy (MOVPE) is also commonly used. Here, the monocrystalline structure is maintained during growth.

The principle of MOCVD was shown first by Manasevit and Simpson [120,121] in 1968/1969 for the growth of GaAs. Typical process pressures are in the range of 10 to 1000 mbar. Due to the high reproducibility of III-V compound semiconductor epitaxy and high throughput, MOCVD quickly became a well-established industrial technique for the growth of III-V semiconductor devices. High scalability made MOCVD superior over UHV-based techniques such as molecular beam epitaxy (MBE). The applied pressures during MOCVD preparation enable easier sample handling compared to UHV-based MBE growth. However, growth processes in MOCVD environment are less understood, since the growth reactions are much more complex. Here, reactions in the vapor phase, reactions on the substrate surface, as well as reaction with reactor residues from earlier deposited material have to be considered. Additionally, the presence of a process gas complicates analysis of the surface by standard UHV-based surface science tools.

In this work, an AIXTRON AIX200 MOCVD reactor was used for the sample preparation, a horizontal low-pressure reactor, which is specially equipped for surface analysis (see Fig. 10): optical in situ probes monitor the sample surfaces during MOCVD preparation, and a MOCVD-to-UHV transfer system enables contamination-free transfer of samples to UHV-based surface science tools. By correlation of results from surface science tools to characteristic in situ RA spectra, we achieved in situ control of sample surface preparation in dependence on the process parameters. Therefore, the samples are mounted on molybdenum sample carriers which enable transfer into UHV environment. In situ monitoring of the sample by RAS or a curvature and pyrometry probe (Laytec EpicurveTT) is provided by an optical view port at the reactor glass tube which consists of strain-free glass and an opening in the liner glass.

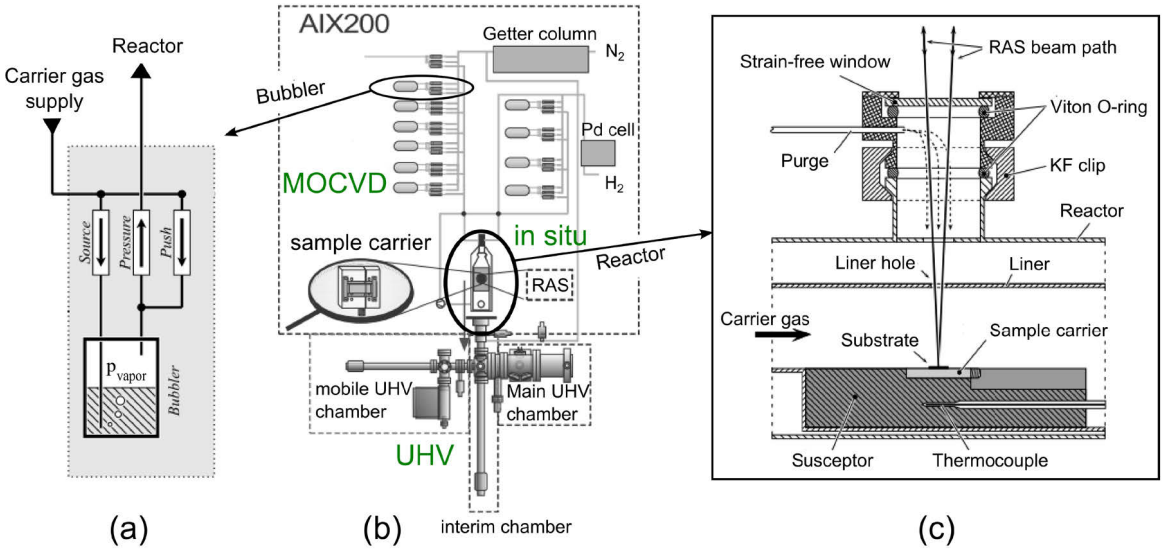

Fig. 10: (a) Precursor source with bubbler and mass flow controllers; (b) schematic drawing of the MOCVD setup with UHV transfer system used in this work; (c) side view of optical view port and MOCVD reactor (modified after [122,123]).

Fig. 10 shows a schematic drawing of the MOCVD setup. H_2 and N_2 serve as carrier gases, which are purified in a palladium cell or a getter column, respectively. In this work, the III-V precursors tertiarybutylphosphine (TBP), triethylgallium (TEGa), trimethylindium (TMIn), and tertiarybutylarsine (TBAs) as well as silane (10% SiH_4, diluted in H_2) are used. Hydride sources are supplied in gas bottles. The III-V precursors are stored as liquid or solid metalorganic compounds at constant temperature and pressure

in so-called bubblers. In a bubbler, the purified carrier gas streams through the metalorganic compounds and carries them into the reactor. To avoid pre-reactions, group III and group V precursors are conducted in separate pipes (lines) and are mixed in the reactor afterwards. Here, the MO-compounds decompose by thermal activation at the sample. Samples are placed on a graphite susceptor which is heated by IR lamps. The process temperature is measured by thermocouples inside the susceptor block. Typical process temperatures for III-V layer growth are in the range of 750 to 1000 K. After decomposition of the precursor molecules, the atoms of the group III and V elements diffuse to the substrate surface and incorporate according to the crystal structure of the substrate material. Carrier gas and source flow into the reactor is adjusted by so called mass flow controllers (MFC). Fig. 10(a) illustrates the principle of a bubbler. The source flow q_{source} from the bubblers is set by the pressure MFC which controls the pressure p_{bubbler} in the bubbler by the incoming and outgoing carrier gas. The "push" MFC stabilizes the flow into the reactor. The partial pressure p_{p} of a precursor in the reactor is given by

$$p_{\mathrm{P}} = \frac{q_{\mathrm{source}}}{q_{\mathrm{total}}} \cdot \frac{p_{\mathrm{vapor}} \cdot p_{\mathrm{reactor}}}{p_{\mathrm{bubbler}} - p_{\mathrm{vapor}}}, \qquad \textbf{Eq. 4}$$

where q_{total} is the total flow of all gases into the reactor, p_{reactor} the total pressure in the reactor and p_{vapor} the vapor pressure of the precursors in the bubbler.

2.4.1.1 MOCVD-to-UHV transfer system

In order to study the MOCVD-prepared samples with UHV-based surface sensitive techniques, our MOCVD reactor is equipped with a UHV transfer system. It consists of an interim chamber, which is connected to the MOCVD reactor, a main UHV chamber, a transfer rod for sample handling, and a mobile UHV transfer chamber to access other UHV analysis chambers (see Fig. 10). MOCVD reactor and all UHV chambers are separated by several gate valves. Baking of the whole UHV system at 120 °C for 10 h and

pumping via the turbo molecular pump of the main chamber leads to pressures $p \leq 4 \cdot 10^{-10}$ mbar.

At the end of sample preparation, the MOCVD reactor is evacuated to pressures around 1 mbar, and plate valves between mobile chamber, interim chamber and main UHV chamber are closed before transfer. The reactor gate is opened when the pressure between reactor and interim chamber is balanced. After transfer of the sample to the interim chamber, the vent to the main chamber is immediately opened. Within 30 s, the pressure in the interim chamber, where the sample is located, is reduced below $p \leq 2 \cdot 10^{-9}$ mbar. After another 5 min of evacuating with the help of a LN_2-cooled cold trap, the pressure is below $p \leq 5 \cdot 10^{-10}$ mbar. When the sample is located in the mobile UHV chamber, all valves are closed and the sample can be transferred to various surface science instruments. A battery powered ion getter pump maintains a pressure of about $p \leq 5 \cdot 10^{-10}$ mbar in the mobile UHV chamber.

2.4.2 Reflection anisotropy spectroscopy

Reflection anisotropy spectroscopy (RAS), also known as reflection difference spectroscopy (RDS) is a non-destructive optical probe of surfaces which can be applied in different environments, e.g. in MOCVD. RAS measures the difference in reflectance (Δr) between two orthogonal directions in the surface plane (x, y) of complex Fresnel reflection amplitudes r normalized to the mean reflectance (r) in near normal incidence configuration of plane polarized light:

$$\frac{\Delta r}{r} = Re\left(\frac{\Delta r}{r}\right) + i\, Im\left(\frac{\Delta r}{r}\right) = \frac{r_x - r_y}{\frac{1}{2}(r_x + r_y)}. \qquad \textbf{Eq. 5}$$

On (100) semiconductor surfaces, the two orthogonal directions are chosen as x = $[0\bar{1}1]$ and y = [011], consequently, the RAS signal measured in this work is defined as:

$$\frac{\Delta r}{r} = 2\frac{r_{[0\bar{1}1]} - r_{[011]}}{(r_{[0\bar{1}1]} + r_{[011]})}. \qquad \textbf{Eq. 6}$$

In the direction of these optical axes, ideal cubic crystals are isotropic and induce no RAS signal. Optical anisotropies mainly originate from the microscopic structure of the surface where the symmetry may be reduced due to surface reconstruction, atomic steps, or adsorbates. However, minor contribution to the RAS signal may originate from non-linear effects in the bulk such as defects or doping [124], and from buried heterointerfaces [26,125,126].

Although, RAS can be applied to many material systems, it is mainly established as a probe for single crystal surfaces. The interpretation of RAS signals from single crystal surfaces is difficult due to various contributions from the surface. Theoretical calculations of RA spectra have to regard the optical response of the surface, which depends on the complex dielectric function of both the surface region and the bulk. Since calculation of the dielectric function from first principles is rather complicated, only a limited number of theoretical studies of RA spectra of some surfaces exists, based on density-functional theory in the local-density approximation (DFT-LDA) (e.g.: [22,24,33,35]). Another successful approach is based on modeling of the RAS signal by different contributions (bulk, interface, surface) even without a detailed understanding of the optical response [26,126]. Also, comparison between RA spectra and experimental results from other surface-sensitive analysis tools such as STM, LEED, XPS, PE, enabled identification of different contributions to the spectra [127].

In the 1980s, Aspnes et al. [128] reported on the potential of RAS as a non-destructive optical probe of semiconductor surfaces. The need for control of substrate surfaces during preparation in different semiconductor growth systems pushed the development of RAS as in situ probe [20,21,129].

In this work, a RA spectrometer from the company Laytec (EpiRAS200) was used which features a phase-modulated RAS setup according to Aspnes [128]. Fig. 11 shows a

schematic sketch of the RAS setup. The light of a Xenon-arc-lamp is linearly polarized by a polarizing Rochon prism. It is focused onto the sample surface at near normal incidence in a 45° angle with regard to the anisotropic optical axes in the surface plane. In case of an anisotropic surface, the reflected light is elliptically polarized. The elliptically polarized light passes through a photo-elastic modulator (PEM), where it is phase modulated. In an analyzing prism, the phase modulation of the light signal is converted in an intensity modulation. The light is detected in a Si photo-diode in combination with a grating-monochromator. The measured modulated signal is processed in the connected electronics which includes a lock-in amplifier for analysis of the small RAS signals in the range of $\pm 5 \cdot 10^{-3}$. Details on the RAS signal processing can be found in Ref. [130].

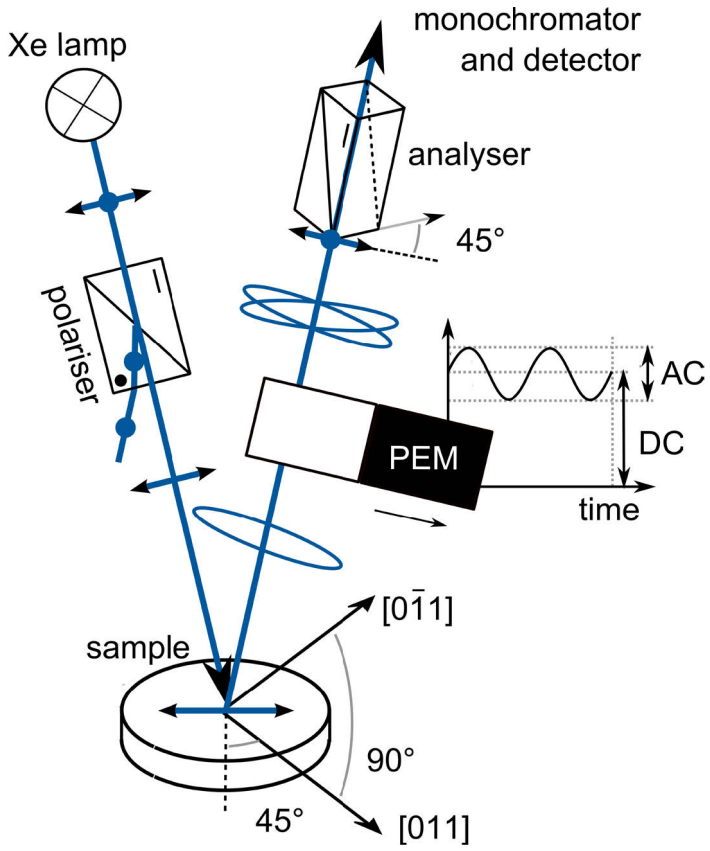

Fig. 11: Principle of the RAS setup according to Aspnes et al. [128].

The optical path of the RAS system used in this in this work is presented in Fig. 12. Spherical mirrors and a beam splitter direct the light on the sample in normal incidence. An anti-wobble mirror (AWM) is used to compensate tilt in the optical path. At the

MOCVD reactor a view port out of strain free glass enables access to the sample surface for in situ monitoring during preparation. A computer system allows control of the spectrometer and displays the measured data. Typically, RAS systems measure in the range of 1.5 to 5.5 eV. All optical parts in the RAS setup may cause additional anisotropies which contribute to the whole measured RAS signal. In our RAS and MOCVD setup, we corrected the measured data by subtracting a baseline RAS signal measured on an isotropic sample.

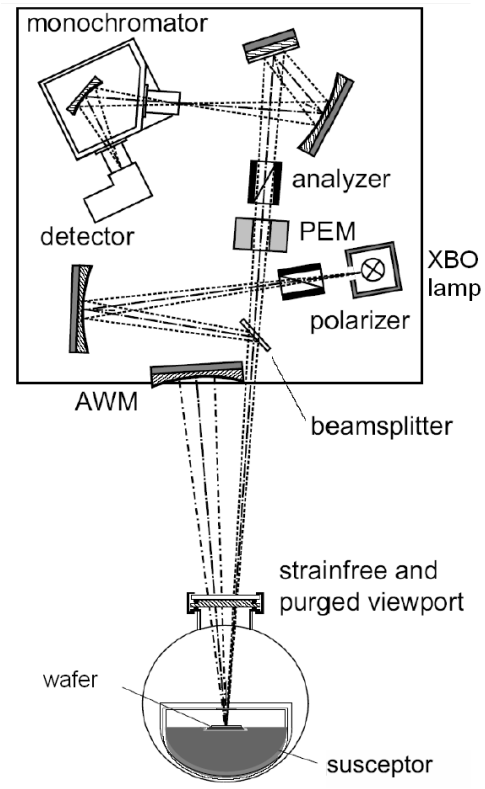

Fig. 12: Optical path of a Laytec EpiRAS 200 system (taken from [130]).

The RAS system can be operated in three different modes: a spectral mode which measures a RA spectrum in dependence of the wavelength, a transient mode which measures the change in a RAS signal at a fixed energy with time, and a colorplot mode which enables continuous RAS measurements in a color-coded representation (colorplot). Transient and colorplot mode enable observation of changes on the sample surface in dependence of the applied process parameters. In addition to the RAS signal, the plain

reflection signal is also measured. Changes in the reflection signal may contain information about surface roughening, growth rate, ternary compositions [131].

2.4.3 X-ray photoelectron spectroscopy

X-ray photoelectron spectroscopy (XPS) represents a surface-sensitive technique to study the chemical composition of sample surfaces. It allows determination of chemical elements as well as their binding state. The physical background of photoemission (PE) is based on the photoelectric effect which was discovered by H. Hertz [132] and explained by A. Einstein [133].

In principle, monochromatic light from an X-ray tube impinges on a sample and excites electrons from occupied states into empty states by the photoelectric effect. If photoelectrons escape into the vacuum their kinetic energy E_{kin} and momentum get detected by an electron-energy analyzer. The measured parameters are E_{kin} of the photoelectrons and their angle with regard to impinging photons and sample surface. If the energy of the light and the work function Φ are known, the binding energy E_{B} can be determined according to:

$$E_{\mathrm{kin}} = \hbar\omega - \Phi - E_{\mathrm{B}} . \qquad \textbf{Eq. 7}$$

The relation between energy levels and energy distribution of photoelectrons is shown in a schematic drawing in Fig. 13. The solid sample exhibits core levels and a valence band. The work function Φ separates the vacuum level E_{vac} and the Fermi energy E_{F} which is at the top of the valence band in case of a metal. For excitation of an electron from a core level state with binding energy E_{B} a respective kinetic energy $E_{\mathrm{kin}} = \hbar\omega - \Phi - E_{\mathrm{B}}$ is measured in the vacuum. In Fig. 13 the energy distribution of the emitted electrons is plotted dependent on their number per energy interval which corresponds to the electron-energy distribution of the solid. In a photoemission experiment, PE spectra are usually plotted as a function of E_{B}. In a real PE spectrum scattered electrons form a continuous

background, so-called secondary electrons, which superimposes on the measured PE lines.

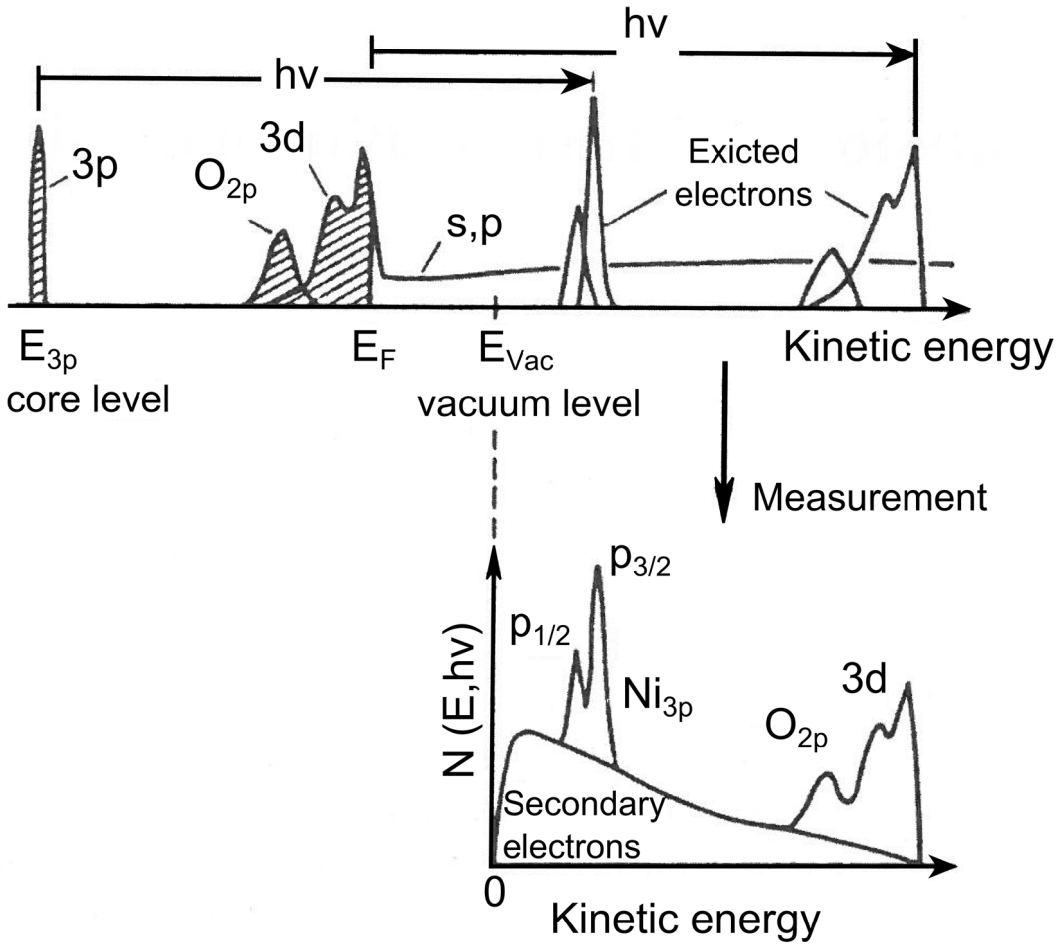

Fig. 13: Schematic drawing of the photoemission process for the example of a transition metal surface (e.g., Ni) with adsorbed atomic oxygen (O_{2p}). Photons with energy hv excite electrons into unoccupied quasi-continuous electron states within the crystal. These photoelectrons leave the crystal and can be detected as free electrons with energy E_{kin}. Scattered electrons form a background of so-called secondary electrons (after Ref. [134]).

PES exhibits a very high surface sensitivity due to the inelastic mean free path λ_e of the electrons in the solid. The photoelectrons are subjected to energy losses by different scattering processes. The specific losses lead to a dependence of λ_e on E_{kin} which is depicted in Fig. 14 [135]. The curve exhibits a minimum of λ_e for photoelectrons with E_{kin} 20 – 70 eV. For higher kinetic energies, which correspond to excitation of photoelectrons

by X-rays, λ_e increases to values in the range of 20 – 30 Å, while for low energies, λ_e increases quickly about several hundred Ås and the surface sensitivity is reduced.

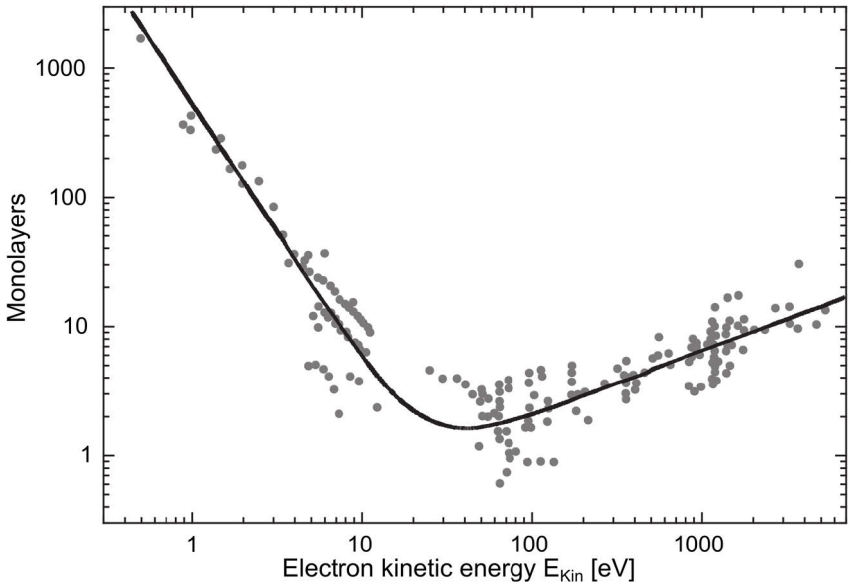

Fig. 14: Inelastic mean free path for electrons depending on their kinetic energy E_{kin} in different solids (grey dots) and the empirically derived "universal" curve [135].

The different PES techniques can be distinguished by the energy of the incoming light, which can be in the ultraviolet regime (5 – 100 eV) for UPS, in the soft X-ray-regime (100 – 1000 eV) for SXPS, or in the X-ray regime (> 1000 eV) for XPS. UPS enables determination of electronic dispersion curves $E(k)$ in the solid, since the wave vector $\vec{k}$ of the photoelectrons is conserved for photon energies < 100 eV [136]. X-rays excite the core level states of a solid, which depend on the chemical state of the sample. The binding energy of a particular core level changes in dependence on different chemical bonding of the same atom. The according difference in energy is called *chemical shift*. A typical example is the *chemical shift* between a metal and its oxide which enables analysis of the surface cleanliness. Therefore, XPS enables chemical analysis of samples by investigation of their core level states.

In this work, we used an XPS system with a hemispherical electron analyzer (Specs Phoibos 100) and a monochromated $Al_{K\alpha}$ X-ray source (Specs Focus 500). The measured XPS spectra were analyzed in detail using commercial software (CASA XPS) [137]. For

the quantitative analysis of the chemical composition of the sample surfaces the data were corrected taking into account the different cross-sections of the specific elements as well as the escape depths of the photoelectrons.

2.4.4 Low energy electron diffraction

Low energy electron diffraction (LEED) is a UHV-based method which enables the determination of the periodic surface symmetry of crystalline materials [138–140]. Electrons originating from a cathode are focused by electronic lenses on the sample surface in normal incidence (see Fig. 15 (a)). The diffracted electrons are imaged on a fluorescent screen where the image is related to the periodicity of the surface of the sample. According to the low energy of the electrons (energy range $E \approx 10 - 1000$ eV), their De Broglie wavelength ($\lambda_{DB} = h/p$) is in the order of the lattice constant of the crystals and the inelastic mean free path of the electrons is only a few Ångströms [135] (see Fig. 14). The back-scattered electrons are filtered by energy to eliminate inelastically scattered electrons. Hence, LEED only detects elastically scattered electrons and only the top atomic layers of the sample contribute to the diffraction pattern.

The diffraction pattern is the result of constructive and destructive interference of the elastically scattered electrons and represents an image of the reciprocal lattice of the surface. Constructive interference of scattered electrons is given by the Laue condition:

$$\vec{k}_f - \vec{k}_0 = \vec{G}, \qquad \textbf{Eq. 8}$$

where $\vec{k}_0$ is the wave vector of the incident electrons and $\vec{k}_f$ the vector of the diffracted electrons with $\left|\vec{k}_f\right| = \left|\vec{k}_0\right| = 2\pi / \lambda$ for elastically scattered electrons, and $\vec{G}$ a reciprocal lattice vector.

The Ewald's sphere construction represents a visualization of the Laue condition (see Fig. 15 (b)). Therefore, the wave vector of the incident electron $\vec{k}_f$ is drawn ending on a reciprocal lattice point. The Ewald's sphere is centered on the origin of the incident wave vector with the radius $\left|\vec{k}_0\right|$. In case of a surface, the Laue conditions is undefined perpendicular to the surface, since $\vec{k}_\perp$ can exhibit any value. Accordingly, the reciprocal lattice of a surface is equivalent to a 2D lattice with rods which propagate perpendicular to the sample surface. Accordingly, the lattice points can be replaced by lattice rods perpendicular to the surface in the Ewald's construction. The spots in the diffraction image correspond to the intersection of the reciprocal lattice rods with the Ewald's sphere.

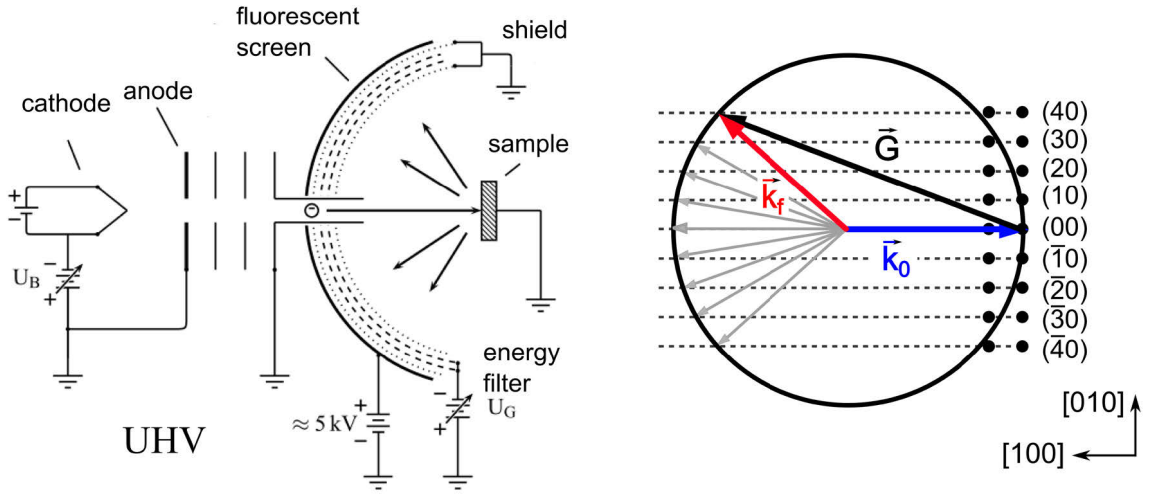

Fig. 15: (a) Schematic drawing of the LEED setup (after [122]) and (b) visualization of the Laue condition by the Ewald's sphere construction (after [38]).

In the experiment, the back-scattered electrons are visible on a spherical fluorescent screen (Fig. 15 (a)). Hence, the diffraction pattern observed on the fluorescent screen is equivalent to the reciprocal lattice of the surface. Since the radius of the Ewald's sphere is proportional to the electron energy, the LEED pattern gets smaller and spots of higher order become visible on the screen with increasing electron energy.

LEED enables determination of the size, orientation and symmetry of the primitive cell of a surface. Reduction of the surface symmetry by a surface reconstruction leads to

additional half-order spots in the LEED pattern as shown comparing the ideal (1×1) and (2×1) surface reconstruction in Fig. 16. A single-domain (2×1) surface exhibits half-order spots only in one main crystal direction, while a two-domain (2×1)/(1×2) surface shows half-order spots in both directions. Accordingly, LEED enables analysis of the domain distribution on the sample surface.

In this work, a commercial LEED setup (Specs ErLEED 100-A) with reverse view LEED optics was used. The diffraction patterns were recorded by a digital video camera.

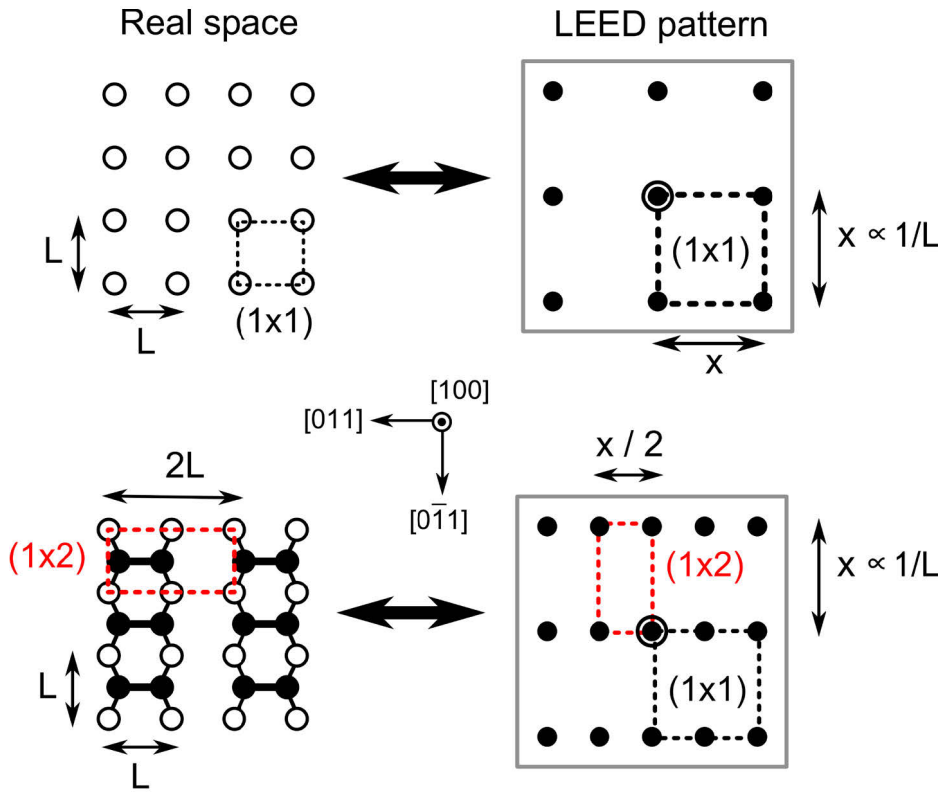

Fig. 16: Models of (100) surfaces with (1×1) and (1×2) symmetry in real space and their corresponding LEED pattern. The ideal (1×1) surface results in a LEED pattern which exhibits the diffraction spots of first order. The double symmetry distance of the (1×2) reconstruction in real space induces half order spots in the LEED pattern (after [38]).

2.4.5 Scanning tunneling microscopy

Scanning tunneling microscope (STM) enables analysis of the structure of solid surfaces with atomic resolution. STM records a direct real space image of the surface by scanning the sample with a sharp metal tip and recording the electron tunnel current as a function of position. Tunneling is a quantum mechanical effect in which electrons travel from one conductor through a potential barrier into a second conductor which cannot be explained classically [140]. Tunneling occurs when the wave functions of the two conductors reach into the potential barrier and overlap within the classically forbidden regions. In the STM, electrons tunnel from the tip through a vacuum gap into the sample surface (or vice versa) only when there is significant overlap, which corresponds to atomic-scale distances. Fowler and Nordheim expressed an approximation for the tunneling current I_t which depends exponentially on the distance d between tip and surface [141]:

$$I_t \propto \frac{U}{d}\exp(-Kd\sqrt{\bar{\phi}}), \qquad \textbf{Eq. 9}$$

where U is the applied voltage between tip and sample, $\bar{\phi}$ the average work function, and K a constant with a value of about 1.025 $Å^{-1}\cdot(eV)^{-1/2}$ for a vacuum gap. For distances of several tens of Ångstroms, a tunnel current I_t is measurable [142]. Lateral resolution of atoms on the surface requires controlled movement of the tip within 1 – 2 Å. Tip or sample movement requires coarse and fine. Piezoelectric plates enable fine positioning of the tip or sample. A suspension or damping system is essential to avoid mechanical vibrations from the environment which disturb the measurements.

During scanning of the sample surface, changes in the surface height and density of states affect the tunnel current I_t. There are two main operation modes for STM: Constant current and constant height mode [143]. In constant current mode I_t is held constant during scanning of the sample surface, as a result the tip images surfaces of constant local density of states at the position of the tip [142]. In constant height mode voltage and height are kept constant and variations in I_t are measured during scanning. Here, the resulting images are related to the charge density of the surface. STM can also be used in

spectroscopic mode (scanning tunneling spectroscopy – STS) which gives local information on the electronic structure of the sample surface. Here, the current is measured in dependence of the voltage at specific positions on the sample.

In this work, we employed a commercial SPECS 150 Aarhus STM in a separate UHV chamber which could be accessed by our UHV shuttle. We used tungsten tips, prepared by electrochemical polishing in potassium hydroxide solution with direct current. Ar ion sputtering enabled cleaning and conditioning of the tip at the STM in the UHV chamber.

2.4.6 Fourier-transform infrared spectroscopy

In order to characterize hydrogen bonds of the Si(100) and Ge(100) sample surfaces, we used a Fourier-transform infrared spectroscopy (FTIR) spectrometer (Bruker IFS 66v/s) in the surface sensitive attenuated total reflection (ATR) configuration [144]. ATR measurements required parallelepiped shaped sample geometries and special sample carrier. Details on our FTIR/ATR setup and data processing can be found in Refs. [13,145].

2.4.7 Sample preparation and standard MOCVD processes

In this work, most samples were prepared by the same MOCVD processes which ensured a contamination-free, monohydride terminated and smooth substrate surface.

2.4.7.1 Standard Si(100) process

Si(100) substrates with 0.1°, 2°, and 6° offcut in [011] direction were used in this work for the investigation of Si(100) surfaces in MOCVD ambient. The substrates were processed in the MOCVD reactor either covered by native oxides or a thin oxide layer prepared by a wet-chemical pretreatment according to Ref. [146]. The Si pretreatment consisted of four different steps: 1. Precleaning in an ultrasonic bath in isopropanol to

remove organic residuals and dust. 2. Removal of organic contamination and metals by boiling the substrates for 10 min in a basic etch solution consisting of ammonium hydroxide (NH_4OH, 25%), hydrogen peroxide (H_2O_2, 30%), and deionized water (H_2O) at the ratio of 1:1:3. 3. Oxide removal by dipping in 3% HF solution for 10 s. 4. Preparation of a well defined thin oxide layer in a boiling acid solution of hydrochloric acid (HCl, 32%), hydrogen peroxide (H_2O_2, 30%), and deionized water at a ratio of 3:1:1 for 10 min. The samples were rinsed in deionized water between all steps and dried in nitrogen flow. The wet-chemical pretreatment ensured similar starting conditions for all samples.

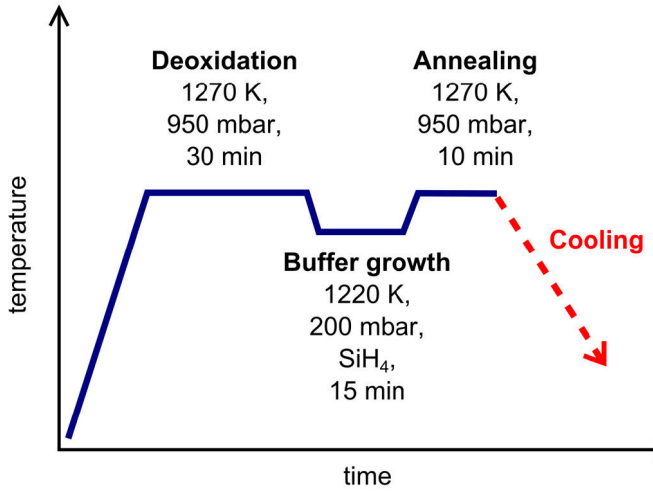

Fig. 17: Schematic diagram of the Si(100) MOCVD preparation showing the particular process steps: deoxidation, Si buffer growth, annealing, and cooling.

For the studies of the clean Si and Ge surface, all reactor parts were cleaned with regard to III-V residuals to avoid unintentional contamination of the samples during processing. The "standard" Si MOCVD process started with oxide removal by annealing for 30 min at temperatures higher than 1220 K (typically 1270 K) and 950 mbar H_2 pressure. Subsequently, a Si buffer layer of 0.25 µm thickness was grown at 1220 K and 200 mbar in 15 min by the use of SiH_4 (10% in H_2) to obtain a smooth surface morphology. After buffer growth the samples were annealed at 1270 K and high H_2 pressures for 10 min.

In this work, the influence of the final cooling procedure on the step and domain structure of the different Si(100) substrates was investigated in detail.

Complete removal of oxides and absence of other contamination, surface structure after deoxidation, as well as interaction of H_2 process gas with the Si(100) surface present the basis for this work and are summarized in section 2.5.

2.4.7.2 Standard Ge(100) process

For the Ge experiments we used Ge(100) substrates with a misorientation of 6° towards the [011] direction specified as "epiready"[1] (supplier: AXT). The "epiready" oxide covered Ge(100) samples were processed in the MOCVD system without any additional wet-chemical pre-cleaning. Preparation of a clean monohydride terminated Ge(100) surface was achieved by thermal oxide removal during an annealing step at 970 K in purified H_2 at a pressure of 100 mbar for 20 min in a cleaned (liner, susceptor) MOCVD reactor to avoid unintentional contaminations.

[1] "epiready" refers to a wet-chemical procedure of the manufacturer

2.5 State of the art: Si(100) surfaces in hydrogen ambient

This chapter summarizes the previous work of our group regarding Si(100) preparation in H_2 ambient including oxide removal [147,148], hydrogen termination [11,13], step structure after deoxidation [94] as a basis for the subsequent study.

2.5.1 Oxide removal and clean surface

Due to its dangling bonds, the clean Si(100) surface reacts with almost any organic or inorganic contamination to form undesirable impurities. Exposure to air immediately leads to so-called native oxidation of the Si surface [149]. While wet-chemical treatments including hydrofluoric acid (HF) remove SiO_2 layers and result in rather stable hydrogen terminated Si(100) surfaces, the recontamination of the surface is only suppressed to some degree [150]. A common experimental approach finishes the wet-chemical treatment of the Si(100) surface with a well-defined re-oxidation step [146] to form a protective SiO_2 layer for thermal removal directly in the epitaxy system.

Ref. [147] reports on thermal removal of oxides from oxidized Si(100) substrates. The deoxidation step consisted of a 30 min annealing step at temperatures higher than 1220 K under flow of purified hydrogen at nearly atmospheric pressure (950 mbar) after formation of a well-defined oxide layer on the substrates by a wet-chemical pretreatment. Samples were transferred to XPS for analysis of the remaining contamination after the annealing step. Fig. 18 shows a comparison of the XP spectra in the range of the O1s and Si2p photoemission lines of Si(100) samples that were annealed at 1170 K (thick blue spectra) and 1220 K (thin black spectra), respectively.

The sample which was annealed at 1170 K (thick blue spectra) exhibits a peak in the O1s XP spectrum at about 533.1 eV which complies well with the chemical shift of +2.1 eV compared to the elemental O1s line at 531 eV, as expected for oxygen bound in SiO_2 [151,152]. In the Si2p XP spectrum, the sample exhibits a peak at about 99.69 eV with a

clearly resolved shoulder at about 100.31 eV corresponding to elemental $Si2p_{3/2}$ and $Si2p_{1/2}$ line [153] and a broad peak structure at about 103.7 eV which complies with the higher oxidation state of Si in the oxidized film [154–156].

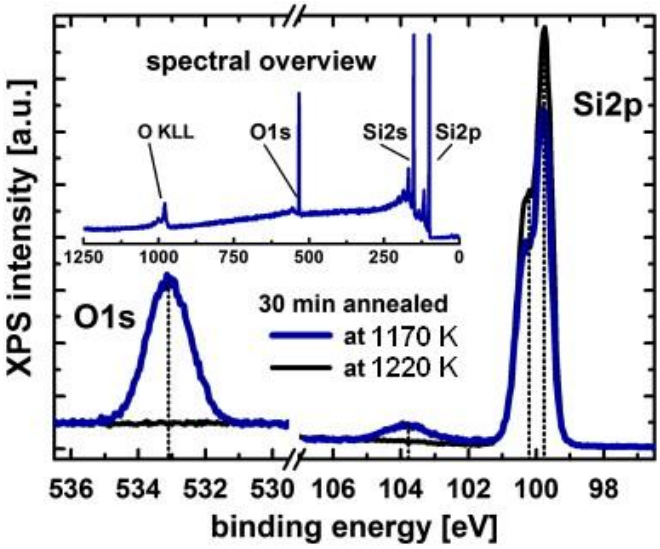

Fig. 18: XPS measurements of the O1s and Si2p lines of two Si(100) samples after annealing in the MOCVD reactor under pure H_2 flow for 30 min at 1170 K (blue, thick) and at 1220 K (black, thin) surface temperature, respectively, and an XPS overview of the non-deoxidized sample (inset) (taken from [147]).

In contrast, the absence of both the O1s line and the signal related to SiO_x (thin black spectra) confirmed complete oxide removal during annealing at 1220 K in H_2. The absence of the O1s signal agreed with an increased intensity of the entire Si2p photoemission line around the binding energy expected for elemental silicon.

XPS measurements after interruption of the deoxidation process at 10 min and 20 min annealing indicated a highly non-linear progression of the underlying deoxidation reaction. While annealing at 1220 K (Fig. 19, grey line) for 30 min in H_2 resulted in an oxide free Si(100) surface, interruption of this process at 10 min annealing time (Fig. 19, thick blue line) led to no significant reduction of the XPS intensities attributed to oxygen or oxidized silicon, similar to removal experiments performed at lower temperatures. XPS measurement following interruption of the deoxidation process after 20 min annealing showed differences in the peak intensities of the O1s and Si2p peak at laterally varied

sample positions (Fig. 19, broken black lines) indicating differences in the residual oxide coverage of the Si(100) surface and non-uniform oxide removal.

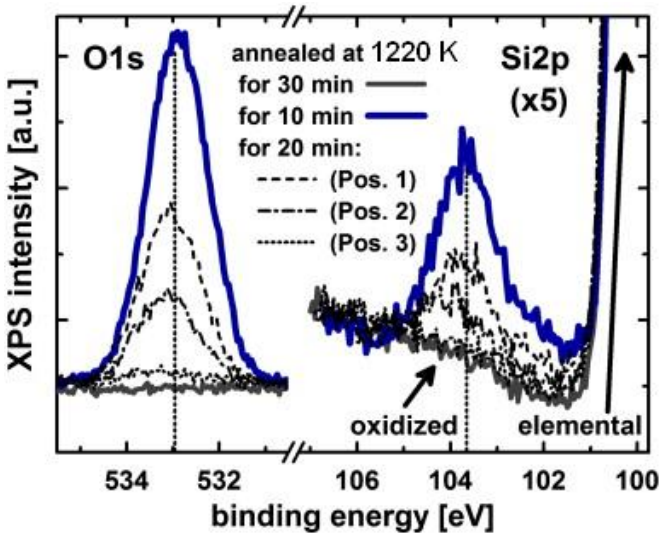

Fig. 19: XPS measurements of the O1s and Si2p lines (scaled by factor 5) of Si(100) substrates after annealing at 1220 K in H_2 ambient for 10 min (thick blue line), 20 min (broken black lines), 30 min (grey line), respectively. The XPS measurements after 20 min annealing were conducted at laterally different positions and indicate an inhomogeneous oxide film due differences in the peak intensities (taken from [147]).

Oxide removal in H_2 ambient of a CVD reactor necessitates temperatures at about 1220 K. In contrast, 1070 K are sufficient for UHV preparation [146]. The substantial difference in the deoxidation temperature indicates different mechanisms for oxide removal dependent on the process gas environment. In UHV, oxide removal occurs by formation and desorption of volatile silicon monoxide (SiO). The silicon oxide coverage impedes SiO desorption. Therefore, formation of voids in the SiO_2 layers initiates oxide removal [157–161]. According to Ref. [162] higher annealing temperatures for oxide removal in H_2 process gas ambient are due to physical restrictions by gas flow. On the other side, H_2 exposure might lead to dissociative hydrogen adsorption and formation of monohydride termination of the Si(100) [78]. Passivation of the Si dangling bonds with monohydrides might suppress diffusion of Si atoms [103] which is a driving mechanism for the void growth. An active role of hydrogen in the deoxidation process is conceivable,

since hydrogen adsorption and desorption might occur during annealing at elevated temperatures.

According to LEED and STM measurements (see Fig. 20), the Si(100) surface exhibits a (2×1)/(1×2) reconstruction which indicates a two-domain surface with single-atomic steps for substrates with low offcut. Both at the clean surface as well as at the hydrogen-covered surface, Si(100) forms Si-Si dimers, thus a (2×1)/(1×2) reconstruction. Investigations of the influence of H_2 ambient on the Si(100) surface preparation were addressed by dedicated FTIR/ATR measurements (see section 2.5.3).

2.5.2 Step and domain structure after deoxidation

Only few studies report on the atomic surface structure of Si(100) prepared in CVD environment, since many surface sensitive probes are not directly available. In most cases analysis of subsequent epitaxial layers enabled indirect conclusions on the surface structure [162,163].

In Ref. [94], we reported on the atomic surface structure of Si(100) substrates after thermal oxide removal in hydrogen. The MOCVD-to-UHV sample transfer system enabled direct access to the atomic surface structure of the CVD prepared Si(100) samples by LEED and STM. Substrates with 0.1°, 2°, and 6° offcut in [011] direction were used to study the influence of the misorientation on the step structure. The samples were annealed at 1270 K and 950 mbar H_2 for 30 min to remove all contaminations from Si(100) substrates (see section 2.5.1) [147,148] and cooled fast in H_2 ambient with a change in pressure from 950 to 100 mbar within 5 min.

Fig. 20 compares LEED patterns of the different substrate after thermal oxide removal in the MOCVD reactor. For the low offcut substrate, equally intense half-order spots in [011] and $[0\bar{1}1]$ direction in the LEED pattern indicate a two-domain (2×1)/(1×2) surface reconstruction. The LEED spots in the patterns of the Si(100) substrate with 2° and 6° offcut exhibit a splitting in the diffraction spots due to the presence of steps. The presence

of half-order spots in both crystallographic directions in the LEED pattern of the 2° sample indicates a two-domain surface with single-layer steps. The LEED pattern of the 6° sample shows stronger intensities for the half-order spots in $[0\bar{1}1]$ direction indicating a preference for the (2×1) surface reconstruction domain.

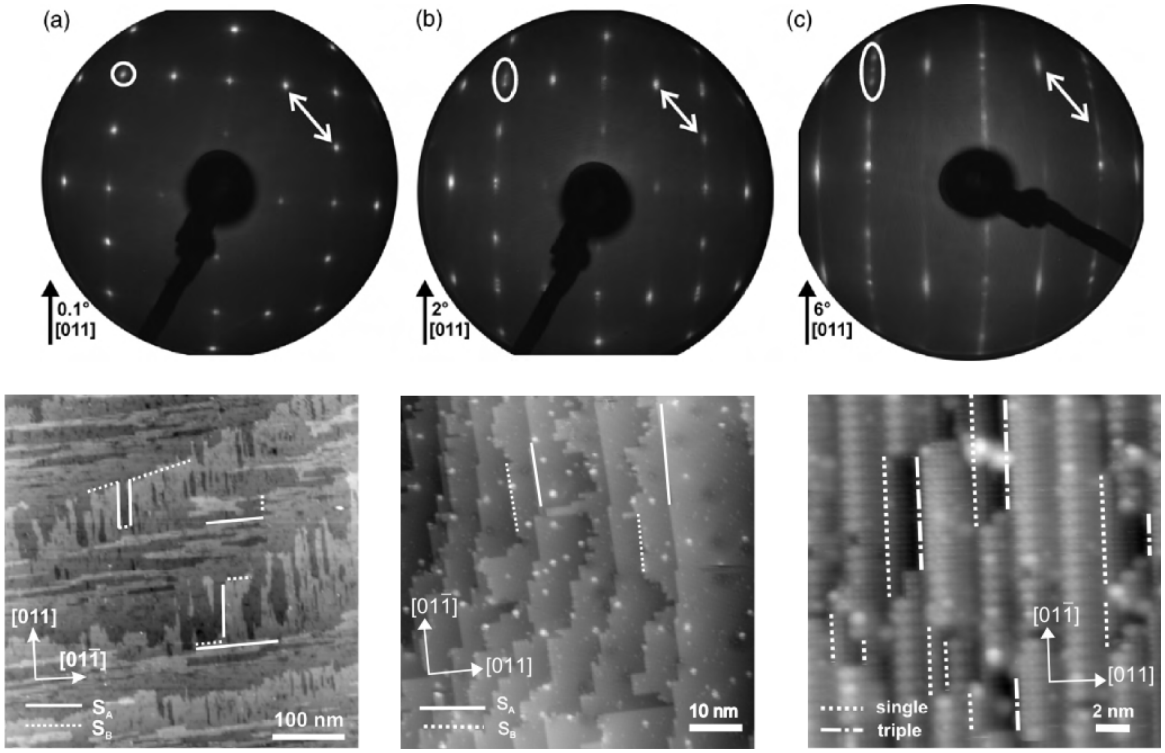

Fig. 20: LEED and corresponding STM data of Si(100) substrates with 0.1°, 2°, and 6° offcut in [011] direction after thermal oxide removal (taken from [94]).

STM measurements were conducted to reveal the atomic surface structure of the different Si(100) substrates (Fig. 20). On the nearly exact Si(100) substrate, we observed S_A and S_B steps. The step edges are frayed and elongated fringes are present on the terraces. According to calculations of the step formation energy [15], formation of S_A steps is favored over formation of S_B steps, which matches with the observation of preferentially elongated S_A step edges. Compared to a basic step configuration consisting of alternating monoatomic steps, the frayed step structure might result from interactions with the process gas. In contrast, Ref. [12] reports on formation of double-layer steps on similar substrates with low offcut, prepared in CVD environment involving a homoepitaxial buffer growth and a specific annealing procedure.

The Si(100) 2° samples exhibit a more regular step structure with alternating S_A and S_B steps. No preference for the A- or B-type domain is noticeable on both samples in agreement with the results from LEED and UHV studies [17]. The Si(100) 6° sample exhibits an irregular step structure: D_B double layer steps prevail, but single- and triple-layer step also occur (see broken white lines in Fig. 20). B-type terraces with dimer rows perpendicular to the step edges are predominant, but the presence of a minority domain representing 10-20% of the surface is clearly visible. This result agrees with the LEED measurements but contradicts observations of clean Si(100) with 6° offcut prepared in UHV where only D_B steps occur [86],[87].

According to AFM measurements and further STM images [94], all Si(100) surfaces show surface roughening on the μm scale after the oxide removal process in CVD environment. Homoepitaxial buffer growth leads to smoother morphology of the Si(100) substrates.

2.5.3 Hydrogen termination of MOCVD prepared Si(100)

The presence of H_2 as process gas may strongly influence the Si preparation in CVD environment. Only few studies [78,79] consider the interaction of Si(100) surfaces with hydrogen-based process ambient typical for CVD processing compared to the detailed knowledge about clean Si(100) and its preparation in ultrahigh vacuum (UHV) [164].

In Ref. [11], we applied several surface-sensitive instruments to study the impact of hydrogen on CVD-prepared Si(100) substrates.

2.5.3.1 Direct proof of monohydride termination

Hydrogen-sensitive ATR measurements were conducted by a commercial FTIR spectrometer in a dedicated UHV chamber on substrates with 2° off-orientation toward the [011] direction. The ATR-Si(100) sample was prepared in the MOCVD reactor as

described in section 2.4.7.1 including a slow cooling procedure from 1220 K to 770 K in 1h at 950 mbar H_2.

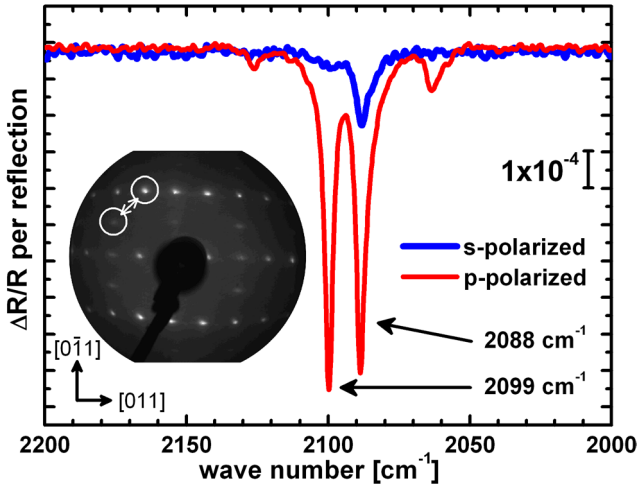

Fig. 21: ATR-spectra of VPE-prepared Si(100) measured with s-polarized and p-polarized radiation: The absorption lines at 2099 cm^{-1} and 2088 cm^{-1} correspond to the symmetric and antisymmetric stretch modes of Si–H monohydrides, respectively. S- and p-polarized spectra show different intensities of the antisymmetric stretch mode which indicates a nearly single-domain Si(100) surface. The corresponding LEED pattern (145 eV) confirms the presence of a clear majority domain on the Si(100) surface (after [13]).

FTIR measurements in ATR mode enabled direct proof for the monohydride termination on the Si(100) samples after processing in H_2 ambient of a CVD reactor as well as quantification of the domain distribution on the monohydride terminated Si(100) surfaces by polarization dependent measurements [11].

Fig. 21 shows ATR spectra measured at the Si(100) sample with different polarization in the spectral region of the characteristic Si–H absorption bands. In agreement with previous CVD studies [78,79], the two major absorption peaks in the spectrum can be identified as the characteristic stretch modes of coupled Si–H monohydrides[165]. Here, hydrogen adsorption leads to formation of H–Si–Si–H dimers and a (2×1)/(1×2) reconstructed Si(100) surface (see LEED image in inset of Fig. 21) resulting in characteristic absorption lines in the ATR spectra at 2099 cm^{-1} and 2088 cm^{-1} due to symmetric and antisymmetric stretch modes, respectively [72].

The intensities of the ATR spectra depend on the saturation of the Si dimers with hydrogen [78]. Saturated and unsaturated dimers may coexist on the MOCVD prepared Si(100) surface. An absolute quantification of the hydrogen coverage is not possible with ATR spectroscopy. So, there is no evidence for a complete monohydride termination of the entire Si(100) surface by these measurements. However, dedicated STM experiments allowed analysis of the hydrogen coverage conducted on Si(100) substrate with 0.1° offcut which were prepared identically to the ATR sample.

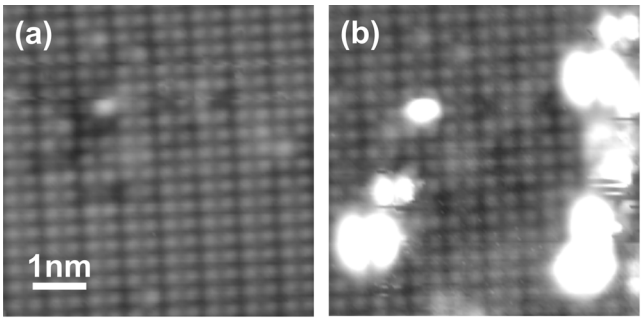

Fig. 22: Empty states STM images (sample bias +1.2 V) of MOCVD prepared Si(100) before (a) and after (b) tip-induced hydrogen desorption: bright double-lobed features are indicative for pairs of dangling bonds (taken from [11]).

STM provides information on hydrogen coverage by tip-induced hydrogen desorption (applying a sample bias voltages in excess of +3 V), as described by Shen et al. [166], enables determination of saturated and unsaturated dangling bonds. Therefore Fig. 22 (a) and (b) compares two images of the same area of a Si(100) sample with atomic resolution recorded before (a) and after (b) a scan at +3.4 V. In Fig. 22 (a), the STM image shows the uniform Si dimers on the surface. The bright lobes in Fig. 22 (b) are typical unsaturated dangling bonds on a otherwise completely monohydride terminated Si(100) surface [167].

According to the STM experiment, the Si(100) surfaces are completely saturated with hydrogen bonds after CVD processing, since we observed no dangling bonds in the STM image before the desorption experiment.

2.5.3.2 Quantification of domain distribution

The polarized ATR measurements enabled quantification of the domain distribution on the monohydride terminated Si(100) surfaces, since the measured intensities for s- or p-polarized radiation reflect the domain distribution on the Si(100) surface (Fig. 21) [165] (for details about the relation between dimer orientation and polarization of the IR radiation refer to [13]). The ATR spectra (Fig. 21) show strong absorption at 2088 cm^{-1} for p-polarization, and only a weak line for s-polarization. The ATR measurements indicate, that most H–Si–Si–H dimers are oriented parallel to the plane of incidence and only few are oriented in the perpendicular direction. Estimation of the domain distribution of the data presented in Fig. 21 [11,13] exhibits a majority domain of 80 %. The corresponding LEED pattern confirms a significant imbalance of the domain distribution, since the intensities of the half-order spots are not equal (Fig. 21 inset). Consequently, slow cooling in high H_2 pressure ambient results in formation of a Si(100) surface with strong majority domain.

In Ref. [13] ATR measurements were conducted on similarly prepared Si(100) samples with fast cooling in H_2 after the annealing step. Polarization dependent ATR measurements and LEED indicated a (2×1)/(1×2) two domain surface with roughly equal distribution of both domains. Consequently, the cooling procedure in H_2 ambient has a strong influence on the domain formation of the Si(100) surface.

2.6 RAS at Si(100) and Ge(100)

RAS enables in situ characterization of sample surfaces during processing in various process ambients such as MOCVD if the origins of the RAS signals are identified. RAS signals of the Si(100) surface have been extensively studied in literature due to their importance for microelectronic devices and their model character for semiconductor surface science. The Si(100) surface is a good example to show how different origins contribute to the RAS signal. Principally, contributions from both terraces and steps have to be regarded [24,32]. Additionally, different terminations and adsorbates significantly change the shape of the RA spectra [25,27,28,31,33,168]. Separation of the different origins of RAS contribution is crucial for the understanding of the spectra.

Because of the cubic symmetry of the diamond crystal structure, the Si bulk is optically isotropic. In order to reduce dangling bonds, dimers form at the clean Si(100) surface. The reduced symmetry of the surface, caused by the reconstruction, gives rise to an optical anisotropy. Dimerization leads to formation of a (2×1), c(4×2) or p(2×2) surface reconstruction depending on the buckling of the dimer in the neighboring rows (see 2.3.1). Ab inito calculations show a strong influence of the surface reconstruction on the RAS signal of Si(100) terraces [24,27,35]. The calculated RAS signal of the c(4×2) reconstructed Si(100) surface agrees best with experimentally obtained RA spectra of the nearly exact clean Si(100) surface [35]. According to Schmidt et al. [24], electronic transitions both directly at the surface and from bulk layers contribute to the signal. The characteristic RAS signal of a clean, nearly exact Si(100) substrate is shown in Fig. 23. It exhibits local maxima at the critical point energies E_1 and E_2 at 3.4 and 4.3 eV, respectively, and minima around 1.5, 3.0, and 3.6 eV. The features are related to different surface modified bulk optical transitions and surface-state related transitions (see Ref. [24] for details).

Fig. 23 (b) shows the RAS signal of a clean vicinal Si(100) surface taken from Ref. [31]. The characteristic features are a broad minimum around 3eV, a small shoulder at the E_1 CP energy, and a maximum at the E_2 CP energy. The influence of steps on the RAS signal

of vicinal Si(100) substrates was under debate in literature for a while. However, the experimental work of Ref. [32] as well as ab initio calculation in Ref. [24] indicated a step induced RAS signal. In particular, both monoatomic and bi-atomic steps might generate a broad RAS feature around 3 eV.

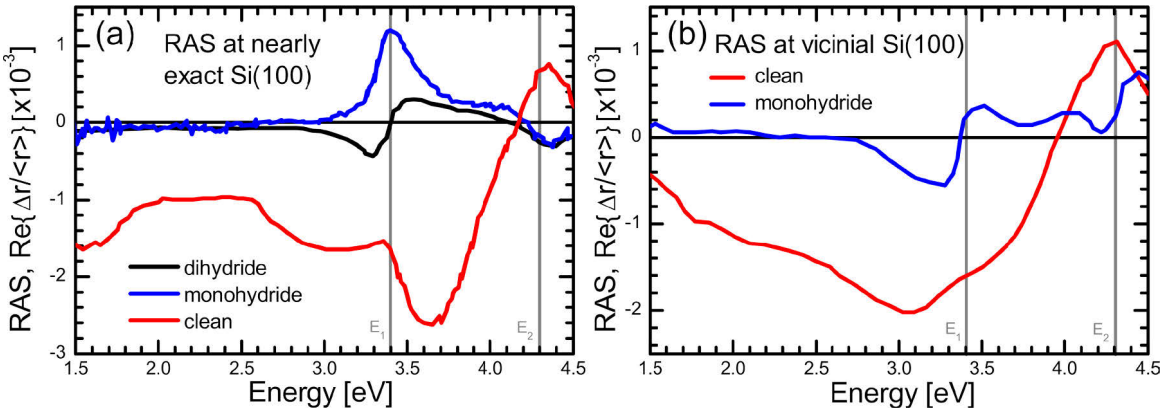

Fig. 23: (a) Experimental RAS signals measured on nearly exact Si(100) taken from Ref. [35]: clean (red line), monohydride (blue line), and dihydride (black line). (b) Experimental RAS signal of vicinal Si(100) taken from Ref. [31]: clean (red line) and monohydride terminated (blue line).

The RAS signal is also sensitive to the adsorption of molecules on the Si(100) surface. Even though the molecules exhibit no optical absorption, they may modify the silicon states leading to a change in the RAS signal [25]. Absorption of atomic hydrogen on Si(100) in UHV may lead to three different surface reconstructions with increasing hydrogen chemical potential: a monohydride (2×1), a mixed (3×1), and a dihydride (1×1) phase [68]. Both monohydride and dihydride Si(100) surfaces show characteristic RAS signals with features around the critical point energies E_1 and E_2 at 3.4 and 4.3 eV, respectively (see Fig. 23 (a)) [25,31,35]. The feature at 3.4 eV is observed as a peak at the monohydride terminated Si(100) surface, while the dihydride terminated exhibits a "derivative"-like spectrum. Remarkably, the opposite behavior was found in the RAS signal of vicinal Si(100), where the monohydride terminated surface exhibits a "derivative"-like signal (see Fig. 23 (b)) and the dihydride terminated surface features a peak at 3.4 eV [35]. According to Ref. [169], RAS features close to the critical points can be either peak-like or "derivative"-like, which is thought to be induced by surface stress

[34]. The sensitivity of RAS to hydrogen termination on Si(100) enables hydrogen adsorption and desorption studies as shown in Ref. [31].

RAS signal of Ge(100) surfaces are only reported for the clean vicinal surface. According to Refs. [36] and [37], there are similarities between the vicinal Ge(100) and Si(100) surface regarding a broad feature around 3 eV and peak-like features at the critical point energies E_1 and E_2.

3. Surface studies of MOCVD-prepared Si(100) and Ge(100) surfaces

In this work, we studied the surface preparation of Si(100) and Ge(100) substrates in MOCVD ambient. We will discuss the results for the different surfaces separately (Si(100) in section 3.1, Ge(100) in section 3.2) before comparing them (section 3.3).

3.1 Silicon (100) surfaces

The importance of hydrogen in silicon processing is well documented in literature. In MOCVD processing, hydrogen is most commonly used as a process gas, making a comprehensive understanding of its interaction with the silicon surface indispensable. Here, we study the dependence of this interaction on major process parameters, its impact on step formation and surface reconstruction domains, and the possibility to control the associated processes using in situ spectroscopy (published in [170–174]).

3.1.1 Interaction of Si(100) with H_2 process gas

First, we consider the interaction of Si(100) with the H_2 process gas ambient which leads to termination of Si(100) with monohydrides during MOCVD processing. Knowledge over surface termination is crucial for understanding the Si(100) surface preparation. Detailed STM investigations in UHV[17,80] revealed that a monohydride termination appears to impede the formation of double-layer steps on Si(100) significantly. In contrast, a tendency for double-layer steps on nearly exact Si(100) with slight misorientation towards [011] was observed after substrate annealing in molecular hydrogen at nearly atmospheric pressure as typically used for MOCVD [12]. While the result is promising for subsequent III–V heteroepitaxy, where double-layer steps are highly desired for prevention of anti-phase disorder [10], it seems to contradict established UHV results both with and without the presence of hydrogen [15–19].

Observation of different domain distribution on Si(100) surfaces depending on the cooling procedure subsequent to oxide removal indicate a strong influence of H_2 during MOCVD preparation [13]. Furthermore, higher annealing temperatures for complete deoxidation in H_2 ambient of a MOCVD reactor [12,147,175] than in UHV [146] indicate a major impact of the process gas on the oxide removal from Si(100).

We applied in situ RAS to characterize the interaction of Si(100) with hydrogen during surface preparation in a MOCVD reactor. According to well-established RA signatures of Si(100) prepared in UHV,[25,28,31] we expected clearly distinguishable spectra of clean and monohydride terminated vicinal surfaces suitable for in situ monitoring. In situ RAS during stepwise cooling from annealing temperature for thermal oxide removal and annealing in nitrogen ambient at 750 K indicate a substantial interaction between hydrogen ambient and Si(100) surface determined by the temperature dependent equilibrium of adsorption and desorption rates.

3.1.1.1 In situ RA spectra during preparation of vicinal Si(100)

We used n-type vicinal Si(100) substrates with 6° misorientations in [011] direction to obtain RA spectra characteristic for both clean and monohydride terminated surfaces independently of the distribution of reconstruction domains according to well-established RA signatures of Si(100) prepared in UHV [25,28,31].

Fig. 24 shows typical in situ RA spectra of our Si(100) samples as observed during surface preparation by annealing in molecular hydrogen at nearly atmospheric pressure in the MOCVD reactor (upper panel). Initially, the sample is still covered by a thin, protective SiO_2 layer [146], which exhibits no optical anisotropy (thin black line). Continued annealing under pure H_2 process gas flow at 1250 K leads to the development of a broad minimum around 3 eV. The final spectrum (thick red line) also contains a shoulder at 3.4 eV and a small peak at 4.2 eV and is considered characteristic for clean vicinal Si(100). In comparison to published UHV data [32], the high sample temperature during our measurements implies systematic broadening of the features as well as peak shifts [29]. Besides the thermal development of the in situ RAS signal expected due to

cooling at the end of the preparation process, interaction of the vicinal Si(100) surface with the H_2 ambient induced characteristic changes. At ambient temperature, the in situ RA spectrum (Fig. 24, lower panel) contains two sharp peak structures in a "derivative"-like arrangement around the E_1 and E_2 critical point energies at 3.4 eV and 4.3 eV, respectively. Our in situ data agree very well with RA spectra of monohydride terminated vicinal Si(100) [25,31]. ATR mode FTIR directly verified monohydride bonds on VPE prepared Si(100) [147] consistent with LEED and STM results [94] (section 2.5). The vicinal Si(100) surfaces exhibit a strong majority surface reconstruction domain as demonstrated by a (2×1) diffraction pattern (Fig. 24, left inset), where most terraces are separated by D_B type double layer steps as shown by STM (right inset).

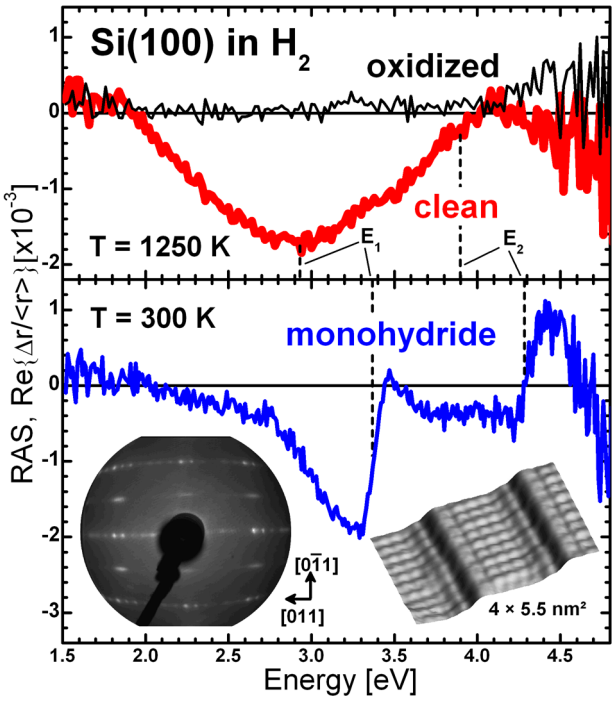

Fig. 24: VPE preparation of vicinal Si(100): in situ RA spectra and benchmarking to surface science in UHV. During annealing under H_2 flow at 1250 K (upper panel), the still oxidized substrate exhibits a featureless signal (thin black line) until the spectrum assigned to clean vicinal Si(100) (thick red line) evolves. Cooling to 300 K at the end of the VPE process (lower panel) leads to a RAS signature associated with monohydride surface, which could be characterized by LEED and STM (insets) confirming a (2×1) diffraction pattern (left) and D_B type steps (right) (taken from [170]).

3.1.1.2 In situ observation of hydrogen adsorption during cooling

Our measurements in Fig. 24 demonstrate the ability to distinguish between the clean and monohydride terminated surfaces of vicinal Si(100) during VPE processing based on in situ RAS. The surface appears to be hydrogen free during annealing at 1250 K, while a monohydride termination is found at 300 K. Temperature dependent in situ RAS data shown in Fig. 25 reveal the transformation of the line shape in detail: Subsequent to thermal deoxidation at 1270 K, we constantly observed the broad and convex minimum structure (thick red line) associated with a clean surface. Gradual reduction in the annealing temperature (in steps of 100 K) went along with transformation (thin lines) to a narrower shape of the RAS signal (thick blue line) reversible by reheating of the sample. Since the spectra shown in Fig. 25 remained stable over time, they represent characteristic equilibrium conditions for the applied process ambient and respective temperature.

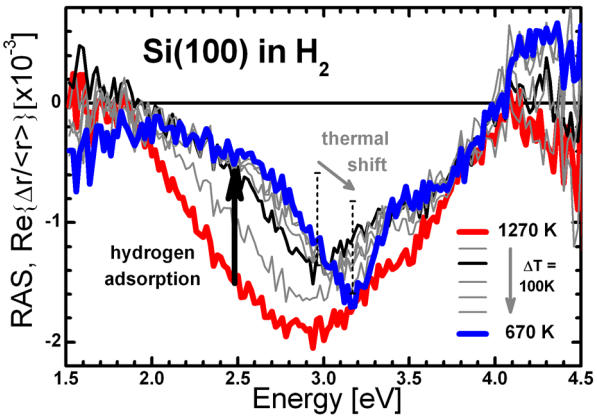

Fig. 25: In situ RAS investigation of vicinal Si(100) while cooling from 1270 to 670 K under H_2 flow. Spectra measured every 100 K (thin lines) show the transformation from clean vicinal Si(100) (thick red line) to a monohydride termination of the surface (thick blue line). Hydrogen adsorption is accompanied by a decay of signal intensity around 2.5 eV (large arrow) and the formation of a characteristic shoulder around 3.4 eV. Due to decreasing temperature, the spectra are also subject to thermal shifts and sharpening of the features (small arrow) (taken from [170]).

In situ RA spectra depend on various influences and their separation usually requires dedicated experiments [176]. Two major trends superimpose in Fig. 25:

(i) Features sharpen and shift to blue due to decreasing temperature [29].

(ii) Characteristic change due to formation of monohydride bonds [25,31].

The spectroscopic features at 670 K (thick blue line) agree well with the complete monohydride termination [11] at 300 K as shown in Fig. 24. Also the development of the RAS signal during the preceding cooling steps (Fig. 25) appears to be driven mainly by thermal effects (small arrow), while crucial changes already occurred above 1070 K (thin black line). Starting with the wide, entirely convex RAS feature assigned to clean vicinal Si(100) at 1270 K (thick red line), the first cooling steps resulted in an explicit decay of the signal intensity in the region around 2.5 eV (large arrow) as well as at about 4.5 eV. Already when reaching 1070 K (thin black line), the spectrum basically consists of a sharper minimum framed by concave elements, which matches with the "derivative"-like shape assigned to the monohydride surface. The results shown in Fig. 25 clearly suggest a monohydride termination of vicinal Si(100) in the hydrogen-based MOCVD process ambient for annealing temperatures up to more than 1000 K. Since UHV investigations [73] showed significant desorption from monohydride terminated Si(100) at 800 K and even below, our in situ observations most probably represent the dynamic balance of hydrogen adsorption and desorption events, which heavily depend on the respective process conditions. Based on STM observations in UHV, Komeda and Kumagai [80] described a model for the hydrogen coverage θ of Si(100) surfaces. Hydrogen desorption is thermally activated and proportional to θ (see Eq. 3). The rate of adsorption depends on the present coverage θ, on hydrogen partial pressure, on gas phase temperature and on the sticking coefficient correlated with surface temperature [76] (see Eq. 2). We assume equilibrium conditions regarding surface and gas phase temperature as well as regarding hydrogen coverage ($t \rightarrow \infty$) during our in situ RAS measurements (Fig. 25). Fig. 26 shows the calculated hydrogen coverage in dependence on the temperature ($T_{substrate} = T_{gas}$) for different hydrogen pressures p_{H2}. Applying parameters identical to Ref. [80], we estimated almost complete hydrogen coverage of our sample below 900 K, about 95% coverage at 1070 K and about 25% at 1270 K for nearly atmospheric pressure of hydrogen (see Fig. 26). Despite uncertainty in the parameters [76], disregard of accurate desorption kinetics [77], and the application of significantly higher pressures, the model agrees quite well with the in situ RAS results shown in Fig. 25. For increasing annealing

temperature, desorption eventually outbalances adsorption of hydrogen, but partial hydrogen coverage is predicted far beyond 1300 K. In an effort to apply RAS as quantitative in situ probe for hydrogen bonds on Si(100), we need to differentiate influences that change the signal [176].

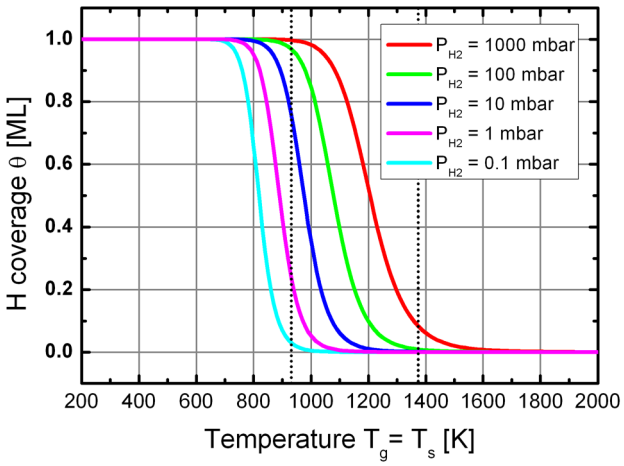

Fig. 26: Calculated H coverage in dependence of temperature for different H_2 pressures.

3.1.1.3 In situ RAS observation of H desorption

Switching the process gas to a nitrogen ambient enables separate observation of the hydrogen desorption process (Fig. 27). The in situ RA spectra of Fig. 27 show the decay of hydrogen coverage on vicinal Si(100) in nitrogen ambient. We prepared a monohydride termination by cooling in H_2 to 770 K (thick blue line) and switched the process gas. In N_2 ambient, Si–H bonds cannot be re-established once they are broken. Only the hydrogen desorption rate governs the successive transformation of the RAS signal with time (thin gray lines) in good agreement with the expected exponential decay of hydrogen coverage. The development stops when achieving the spectrum assigned to clean vicinal Si(100) (thick red line) after about 35 min. Upon resupplying H_2, we observed rapid hydrogenation confirming the high equilibrium coverage equivalent to a complete monohydride termination at 770 K. In principle, transient in situ RAS measured at fixed energies provides experimental access to the hydrogen desorption and adsorption characteristics in the MOCVD ambient.

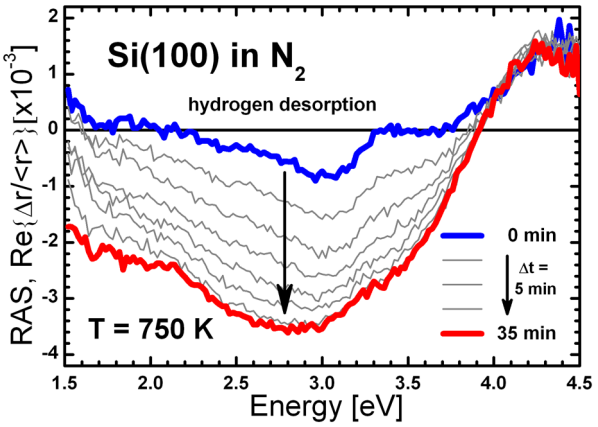

Fig. 27: In situ RAS observation of successive hydrogen desorption from vicinal Si(100). At the constant temperature of 770 K, switching the process gas to a N_2 ambient induces successive loss of hydrogen bonds. The initial monohydride termination at t = 0 min (thick blue line) successively transforms (thin gray line) until reaching the constant state of clean vicinal Si(100) (thick red line) after about 35 min (taken from [170]).

Our results demonstrate in situ access to the interaction of Si(100) surfaces with hydrogen ambient, which we consider crucial for the development of unique atomic surface structures by MOCVD based processes [11,12].

3.1.2 Anomalous double-layer step formation

The interaction between Si(100) and H_2 process gas during MOCVD processing strongly influences the step formation mechanisms on Si(100) surfaces, which we will discuss in this section.

Previous LEED and STM results showed formation of mainly single-layer steps after deoxidation of Si(100) substrates in H_2 ambient for substrates with 0.1° and 2° offcut (2.5.2, [94]). However, in section 2.5.3.2, ATR spectra and LEED results indicated an imbalance in the domain distribution on Si(100) with 2° offcut after slow cooling at high H_2 pressure. A tendency towards double-layer steps on nearly exact Si(100) substrates is reported in Refs [12,14], which contradicts theoretical and experimental studies of the

step formation energies in the range of the (2×1) monohydride reconstruction [18,19],[17].

Here, we directly display both the presence of true D_A double-layer steps on Si(100) with 2° misorientation in the [011] direction via STM and the control of their formation in situ, as a result of a CVD preparation process. In situ RA spectroscopy identifies the relevant process parameters and supports a model [92] based on surface vacancy generation, diffusion, and annihilation at step edges, which may account for the formation of this anomalous step structure.

3.1.2.1 Preparation of Si(100) with majority A-type domain

Si(100) substrates misoriented by 2° in [011] were wet-chemically pre-treated and subsequently processed in a MOCVD system under in situ control by RAS. Subsequent contamination-free sample transfer to UHV [127] enabled dedicated surface investigations by XPS, LEED, and STM as well as correlation to our in situ results. XPS verified the absence of surface contamination apart from traces of residual background arsenic (< 0.05, typically 0.01 ML).

After deoxidation, Si growth, and annealing (see section 2.4.7.1) we prepared the samples by cooling at a rate of ~8 K/min from 1270 to 770 K at a pressure of 950 mbar H_2 at the end of the CVD process. On similarly prepared Si(100) samples, we already showed a strong domain imbalance by LEED and FTIR measurements [11],[13] (see section 2.5.3). The LEED pattern, shown in the inset of Fig. 28, exhibits high-intensity half-order spots in the [011] direction, while in the $[0\bar{1}1]$ direction the half-order spots are suppressed (as indicated by the circles in the figure). Hence, dimers oriented in the [011] direction, perpendicular to the step edges (see the sketch in the lower inset), and therefore of type A, dominate the surface. Fig. 28 also shows the corresponding in situ RA spectra measured at 300 K (green line). The spectrum exhibits features around the critical point energies E_1 and E_2 of Si, a strong peak at 3.4 eV and a smaller one around 4.3 eV, respectively, as well as a shoulder around 4.0 eV. The RA spectrum with regard to its peak positions agrees perfectly with data of nearly exact Si(100) surfaces terminated with monohydrides

[31,35]. However, direct comparison to the RA spectrum of Ref. [35] (Fig. 28, red line) shows differences in amplitude and sign of the signal. Ref. [35] showed the sensitivity of RAS to the surface reconstruction of monohydride terminated Si(100) by experimental and theoretical results. Domains with mutually perpendicular dimer orientation exhibit RAS signals with opposite sign. Since RAS integrates over the entire probed surface area, the measured signal reflects the preferential dimer orientation which enables domain quantification by linear scaling (blue arrow) [177]. When comparing experimentally and theoretically derived RA spectra, in Ref. [35], the authors estimated a domain imbalance of 60:40, with a B-type domain majority for their sample obtained by electromigration on a nearly exact Si(100) surface. From our FTIR results [11,13], (see section 2.5.3), we infer a domain distribution of about 82:18 with an A-type majority domain. Comparison of the peak intensity at 3.4 eV of our RA spectrum to the spectrum of Ref. [35] scaled by a factor −3.5 (dotted gray line) indicates a domain ratio of about 85:15, in good agreement with the FTIR results [13].

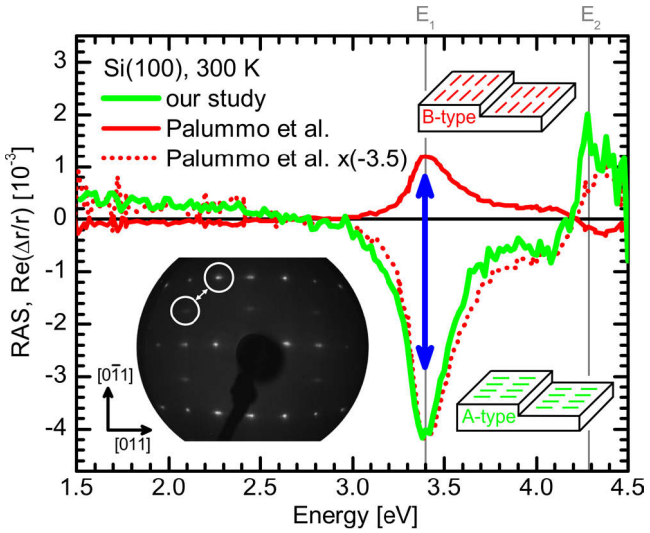

Fig. 28: LEED pattern (144 eV) and corresponding in situ RA spectra of a monohydride terminated Si(100) surface with 2◦ misorientation in [011] (green line) indicating a strong prevalence of the A-type domain (lower sketch) as well as RAS data from Ref. [35] (red line) of a monohydride terminated nominal Si(100) sample with a preferential B-type domain (upper sketch). For comparison, the scaled data (factor −3.5) of Ref. [35] (red dotted line) is also depicted (taken from [171]).

3.1.2.2 Direct observation of D_A steps on Si(100) 2°

LEED, in situ RAS, and FTIR [13] enable independent quantification of the domain ratio of our MOCVD prepared Si(100) samples on a large scale. We observed a strong majority of the A-type domain on the Si(100) samples after CVD processing. Remarkably, this result would imply the presence of unfavorable D_A-type steps on the surface. We applied STM to resolve the surface structure on an atomic to microscopic length scale.

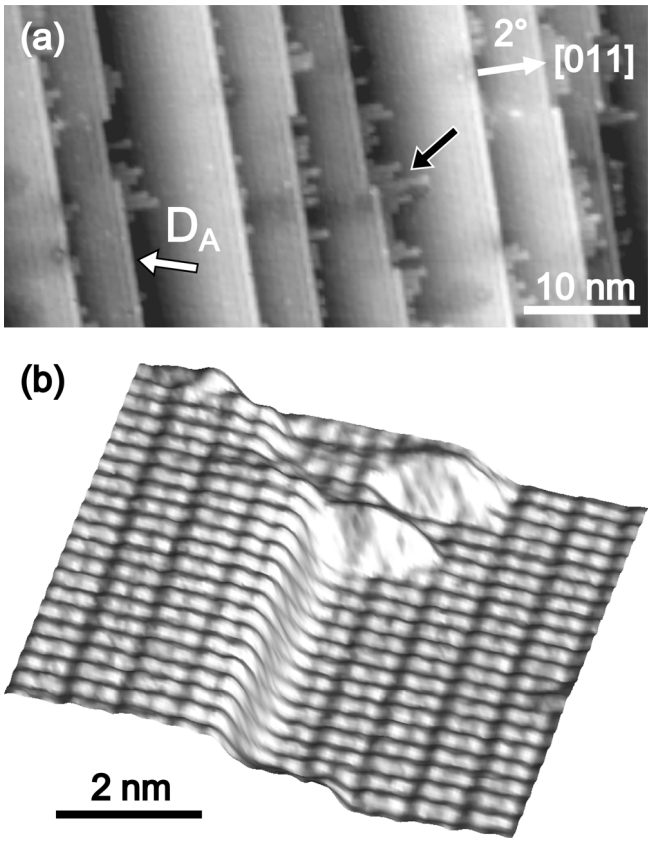

Fig. 29: (a) Empty-state image (I_t = 170 pA, V_t = 1.24 V) of Si(100) surface misoriented 2° in the [011] direction with D_A-type steps (one example marked by a white arrow). The black arrow indicates dimer rows of the residual B-type domain. (b) Empty-state image (I_t = 150 pA, V_t = 1.24 V) and atomic resolution detail (smoothed, z-scale 3×magnified) of a double-layer step at the Si(100) surface with 2° misorientation in [011]. Dimer rows parallel to the step edge, without an intermediate terrace, are clearly visible, implying a true D_A-type step (taken from [171]).

Fig. 29 (a) shows a typical STM image of this Si(100) surface where a step structure of terraces with rather straight edges was observed. The difference in height of these terraces

corresponds to two atomic layers. In some step edge locations, short stripes of variable length extend perpendicularly from the straight step edges onto the lower terrace (black arrow), but in many places the straight step edges are sharp without an intermediate fringe or terrace (one example is indicated by a white arrow). To study the structure at the step edges in more detail, we carried out STM measurements with atomic resolution. Fig. 29 shows an area around a step edge clearly resolving individual Si surface atoms. Rows of pairs of atoms are separated by a deeper trough than the one separating atoms within one pair. We identify these pairs as Si dimers, where each Si atom is terminated by a single hydrogen atom, according to previous results [11,13] (see section 2.5.3). The dimer rows run parallel to the step edge both on the terrace above the step edge and on the terrace below the step edge. The step height was confirmed to correspond to a double atomic layer step. Hence, the step type was identified as a D_A-type step referring to a double-layer step with dimer rows parallel to the step edge. Accordingly, the straight step edges in the large area image of Fig. 29 (a) can be identified as A-type step edges, and the short stripes extending perpendicular from the A-type step edges correspond to residual dimer rows of the B-type terrace. In the surface region shown in Fig. 2(a), the dominance of the A-type terraces is evident and the absence of an intermediate ledge in many locations implies a high proportion of true D_A-type steps. We obtained similar images at several locations on the sample within the scanning range of our STM (2×2 μm^2).

Our observation of D_A-type steps after standard CVD preparation is in disagreement with previous experimental [16,17] and theoretical [15,18,19,88] reports in the literature, where D_A steps were found to be the energetically most unfavorable step type on both the clean and monohydride Si(100) surface.

3.1.2.3 In situ observation of domain formation

The sensitivity of RAS to the dimer orientation on Si(100):H enables us to (i) observe and quantify the formation of the majority domain during the process, (ii) extract the essential preparation parameters, and (iii) use this information for comparison with our microscopic understanding. Thereby, we found that conditions in the temperature range

between 970 and 1020 K appear decisive for the generation of D_A double-layer steps. Crucially, we kept the hydrogen pressure constant at 950 mbar during our preparation process down to temperatures around 770 K. Previous experiments, where the pressure was reduced above 770 K, led to the standard two-domain (2×1)/(1×2) reconstruction [94].

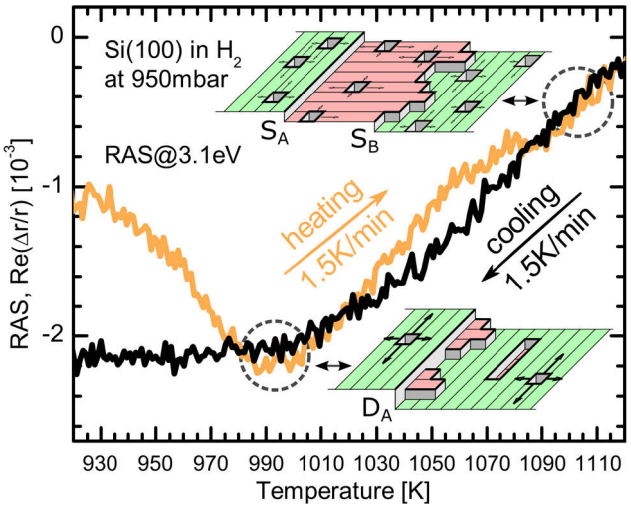

Fig. 30: Transient RAS measurements of a Si(100) sample with 2° misorientation at 3.1 eV (corresponding to the characteristic RAS peak at 3.4 eV of Fig. 1 in the given temperature range) during heating (orange line) and cooling (black line) between 920 and 1120 K in H_2 at a constant pressure of 950 mbar. Vacancy generation increases with temperature (upper sketch), whereas vacancy diffusion dominates at temperatures around 990 K (lower sketch) (taken from [171]).

To study the step formation in dependence on temperature, we observed the development of the peak around 3.4 eV in the RA spectrum of Fig. 28 during cooling and heating between 920 and 1120 K (1.5 K/min). The resulting transients at 3.1 eV (RAS peak thermally shifted) in Fig. 30 provides information on step structure formation. While cooling identifies the temperature for step formation, a comparison between the transients during cooling and heating at higher temperatures narrows down the possible mechanisms for this process. Starting from a surface with a small preference of the type-A domain, during heating (orange line), the magnitude of the signal first increases at temperatures up to 990 K and then steadily decreases to a value close to zero at 1120 K. During cooling from 1120 K down to 990 K (black line), the magnitude of the RAS signal increases, following a trajectory close to the one during heating. When cooling below 990 K, the RA

signal roughly remains constant. Based on these data, we conclude that the temperature range around 990 K is decisive in the formation of the D_A step structure. Above 990 K, the same trend is observed between heating and cooling and the two trajectories are closely aligned, although we observed some hysteresis between cooling and heating in the temperature range between 1080 and 1030 K. The close match between the curves suggests that the surface is close to a dynamic equilibrium in this temperature range. In principle, changes of the RA signal intensity may be related to (i) thermal shifts [176], (ii) hydrogen termination [11,31,170], or (iii) the surface domain ratio [35]. Since we estimated the hydrogen coverage of Si(100) to about 80% at T = 1120 K and P = 950 mbar (see Fig. 26) [80,170], the RA signal at this temperature and below mainly reflects the surface domain ratio.

3.1.2.4 D_A step formation process

In section 3.1.1, we provided evidence of the strong interaction of the hydrogen ambient with the Si(100) surface under standard CVD preparation conditions [170]. At elevated temperatures, adsorption and desorption of hydrogen take place continuously at the surface [80], providing for highly reactive conditions. The present domain ratio is determined by the interplay of several processes: hydrogen adsorption and desorption, Si removal (etching) or growth, diffusion of Si adatoms or vacancies, annihilation of vacancies, or attachment of adatoms at step edges. These processes depend on major preparation parameters such as substrate temperature, hydrogen partial pressure, and silane supply. While direct Si removal from the B-type step edge might explain the reduction of the B-type terrace, and consequently the formation of an A-type majority domain, step energetics [18,19] disfavor A-type double-layer steps over a broad range of the hydrogen chemical potential. Hence, a model relying not merely on processes at the step edges should be considered. We therefore propose to adapt a model by Bedrossian and Klitsner [92] and Swartzentruber [93] based on Si removal on the terraces. They investigated experimentally the step structure resulting from Xe-ion bombardment and annealing. Under certain conditions, they found the formation of a majority domain and of D_A steps, which depended crucially on the preferential annihilation of the vacancies at

the B-type step edge. We propose that a similar process occurs in our case, where the reactive process environment at 950 mbar H_2 pressure induces vacancy generation: The domain ratio at temperatures between 990 and 1120 K varies continuously, depending mostly on Si vacancy generation, diffusion, and annihilation. If the rate of vacancy generation at 990 K is finite, but relatively small, the generated vacancies diffuse and reach B-type step edges where they annihilate [92], resulting in a retreat of the B-type terrace and near-perfect A-type terraces (see Fig. 30, lower sketch). As the temperature increases and the rate of vacancy generation increases more strongly with temperature than the diffusion rate [18,100], diffusion to the B-type step edges is too slow to remove vacancies from the terraces (see Fig. 30, upper sketch). Since vacancy generation will not differ significantly on A- and B-type terraces, a more balanced domain ratio results, leading to a reduced RAS signature at higher temperature.

In principle, the resulting anomalous D_A step structure is thought to be thermodynamically unstable and should depend on the continuous removal of Si surface atoms, diffusion, and annihilation at the step edge. However, cooling below 990 K goes along with the formation of a stable monohydride termination [170]. Thus, Si surface atom removal does not occur anymore and hydrogen termination leads at the same time to a significant reduction of the Si adatom diffusion rate [103] and to a passivation of the Si(100) surface [80]. In analogy, vacancy diffusion rates may also be reduced, resulting in a stabilization of the anomalous surface step structure. This accounts for the difference in the two transients of Fig. 30 in the temperature range below 990 K.

3.1.3 Domain-sensitive in situ observation of layer-by-layer removal

Our model for the formation of D_A steps on Si(100) 2° offcut samples during annealing in 950 mbar H_2 is based on vacancy formation on the terraces and subsequent vacancy diffusion and preferential annihilation at the step edges [171]. In this section, we present experimental evidence for chemical Si surface atom removal in highly reactive H_2 ambient. We employed RAS as a surface-sensitive probe, which detects an oscillating

measurement signal related to layer-by-layer removal on nearly exact Si(100) surfaces under (MO)CVD conditions. STM measurements confirmed vacancy formation processes on the terraces involving anisotropic, elongated vacancy islands.

3.1.3.1 In situ observation of layer-by-layer removal

We used Si(100) substrates with 0.1° misorientation in [011] direction with optional wet-chemically pre-treatment before CVD processing. Samples were prepared according to our standard Si processes including deoxidation, Si-buffer growth, high temperature annealing (see 2.4.7.1). After fast cooling from 1270 °C to 770 °C (heating system off) and simultaneous pressure change from 950 to 100 mbar within 5 min, the sample exhibited the characteristic RA spectrum of monohydride-terminated Si(100) [35], shown in Fig. 1 (b) measured at 320 K. It consists of peak structures around the critical point energies of Si, E_1 and E_2, at 3.4 eV and around 4.3 eV, respectively, as well as a shoulder around 4 eV (green line). According to the strong negative peak at 3.4 eV, the RA spectrum corresponds to a Si(100) surface with a preference for the A-type domain (compare to Fig. 28).

We applied in situ RAS to study the inuence of H_2 on the domain ratio of nearly exact Si(100) surfaces during annealing in the temperature range between 920 K and 1070 K, which had previously been shown to be the critical range for D_A-type step formation in the case of the 2° Si(100) surface (see Fig. 30). Fig. 31 (f) shows continuous in situ RAS measurements (41s per spectrum) in color-coded representation (colorplot) of a 0.1° Si(100) sample during annealing at 1040 K and a H_2 pressure of 950 mbar after preparation of a preferential A-type domain surface as described above. In the beginning, the surface exhibits the spectra of the monohydride-terminated Si(100) surface with a preferential A-type domain indicated by the strong negative intensity around 3.1 eV (spectra shift with increasing temperature towards lower energies [178]). During further annealing, we observe an alternating change in the sign of the RAS peak around 3.1 eV in the colorplot. Here, a positive sign of the RAS peak corresponds to a surface with a preferential B-type domain.

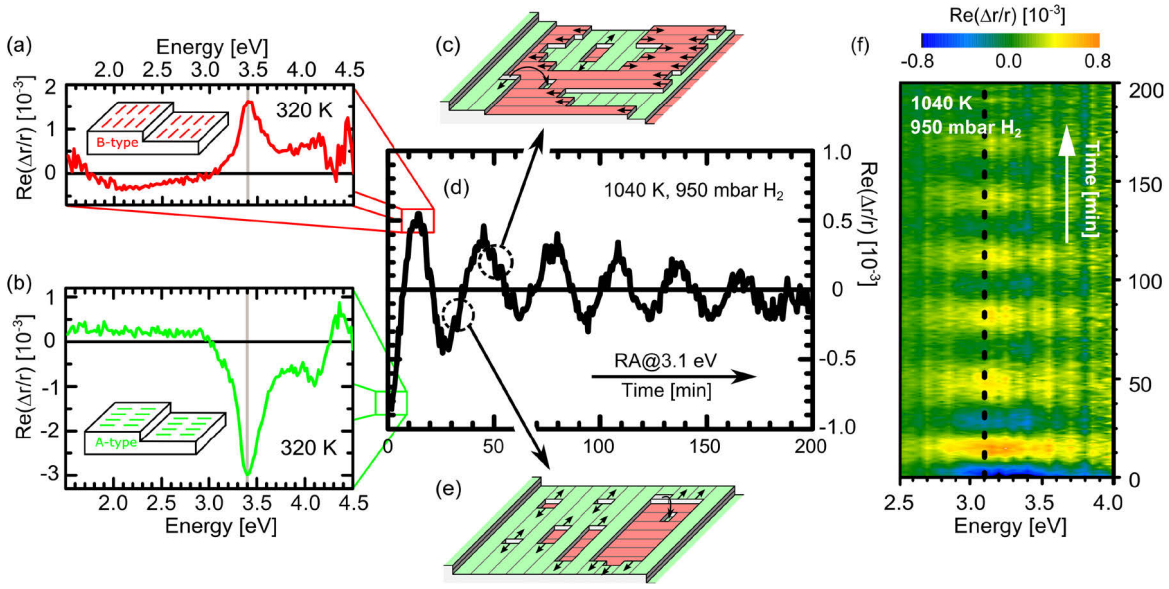

Fig. 31: In situ RAS of Si(100) 0.1° offcut samples with preference for the A-type (b) and the B-type domain (a) obtained during preparation (see text) and measured at 320 K. The sketches show the dimer orientation related to the step edges for the different domain types. Fig. 31 (f) shows continuous in situ RAS measurements of Si(100) with 0.1° offcut during annealing at 1040 K in 950 mbar H_2 represented in colorcoded mode (41s per RA spectrum). The dashed black line at 3.1 eV corresponds to the transient RAS measurement shown in (d) at the characteristic RAS peak of monohydride-terminated Si(100), which shifts with temperature [178] (see grey line in (a) and (b)). Positions on the transient marked with green and red squares correspond to a sample surface with A- or B-type majority domain, respectively, as shown in (a) and (b). In sketches (c) and (e) the vacancy formation mechanism is depicted, which explains the layer-by-layer removal process (see text) (taken from [172]).

For better illustration of the observed changes in the RAS signal with time, Fig. 31 (d) shows a RAS transient at 3.1 eV (see black dotted line in Fig. 31 (f)). The chosen energy corresponds to the characteristic RAS peak of the monohydride terminated Si(100) surface at 1040 K. The transient clearly shows an oscillation of the peak amplitude with a constant period of 30.8 min and slowly decreasing amplitude. According to the definition of the RAS signal, we observe a switch of the majority amongst the two mutually perpendicular dimer orientations whenever the RAS peak changes its sign. We conclude that the oscillations result from monolayer (ML) removal from the surface: Removal of one ML Si atoms from an A-type terrace results in a B-type terrace and vice versa. Starting from a predominant A-type surface (green square) increasing B-type oriented

surface area decreases the RAS amplitude due to the implicit integration over the probed surface area. Reaching equal domain distribution, the RAS signal cancels out completely and once the former minority domain prevails, the signal changes its sign. The prevalence of the B-type domain can be preserved on the surface, if we cool down the sample directly after evolution of the positive RAS peak (red square) with maximum cooling rate (heater off) and simultaneous reduction of the H_2 pressure from 950 to 50 mbar. Thereby, we obtain a sample with preference for the B- type domain with a positive RAS peak at 3.4 eV. The corresponding RAS signal is shown in Fig. 31 (a). The decreasing amplitude during the oscillation indicates a reduction of the maximum prevalence of both majority domains. In contrast to RHEED oscillations, which reflect surface roughness variations during Si layer removal or growth [98,179], RAS detects layer removal from specifiable terraces at the Si(100) surface, which enables in situ control of the majority dimer orientation. Hence, unlike RHEED, RAS oscillations directly reflect the domain content, with maximum amplitude in the case of double-layer stepped surfaces (whereas a smooth single-layer stepped surface would result in zero signal).

3.1.3.2 Vacancy formation and layer-by-layer removal mechanism

The oscillating RAS signal in Fig. 31(d) and (f) corresponds to an alternating formation of preferential A- and B-type domain surfaces, which implies a Si layer-by-layer removal process. The constant oscillation period indicates uniform removal of a bilayer for every period of the oscillation during H_2 annealing. The process must imply differences in the surface structure during the decreasing and increasing slopes of the transient, where the magnitude of the RAS signal indicates equal domain prevalence, but the different gradients of its time dependence lead again to the development of either A- or B-type majority domains, respectively. This limits the possible mechanisms for the removal process. We can rule out processes which regard only removal processes from the step edges that are related to the misorientation. Si removal starting from the step edges of a preferential A-type domain surface would result in a regular sequence of S_A and S_B steps and continuous Si removal in step flow mode, thus, a decreasing RAS amplitude which approaches zero without oscillations.

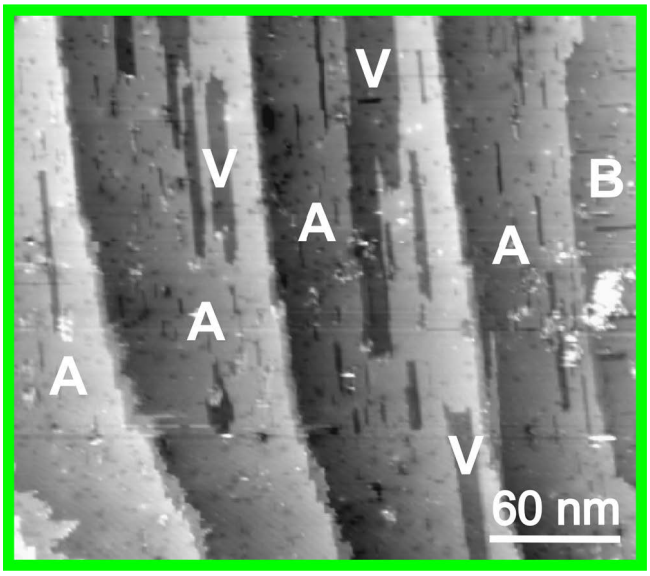

Fig. 32: STM measurement (I_t = 290 pA, V_t = 1.24 V, empty state image) of Si(100) with 0.1° offcut after fast cooling with simultaneous pressure ramp. 'A' and 'B' denote the domain type of the terraces, 'V' marks vacancy islands (taken from [172]).

We applied STM to reveal the surface structure of a Si(100) 0.1° sample which was cooled quickly with the same pressure ramp as the sample of Fig. 31(b) (see Fig. 32). The surface exhibits large A-type terraces (dimer rows parallel to step edges) and small B-type terraces (dimer rows perpendicular to step edges). The steps run slightly curved along $[0\bar{1}1]$ direction. The surface mainly exhibits D_A steps, but in some locations narrow B-type terraces remain. On the A-type terraces we also observe missing dimer rows forming vacancy islands of the B-type domain (indicated by 'V's). The vacancy islands exhibit an elongated shape extended along the direction of the dimer rows.

The occurrence of vacancy islands, as observed in the STM images in Fig. 32, substantiate Si removal from the terraces during cooling in H_2 ambient. Even though the interaction with the surface in the Si removal process during H_2 annealing differs from that in removal by Xe ion bombardment under UHV conditions [92,98], the resulting layer-by-layer removal mechanism is similar, relying on vacancy formation on the terraces. For the alternating formation of preferential A- and B-type layers during Si removal on nearly exact Si(100) substrates, we consider a mechanism that consists of (i) generation of vacancies on the terraces, (ii) anisotropic diffusion of vacancies (faster

parallel than perpendicular to the dimer rows) [99], and (iii) nucleation of vacancy islands with anisotropic expansion parallel to the dimer rows [92], as well as (iv) suppression of vacancy nucleation on the subjacent Si layer due to refilling by diffusing Si adatoms [92,180] (see Fig. 31(c) and (e)).

We conjecture that vacancies nucleate during annealing in H_2 and coalesce to elongated vacancy islands oriented parallel to the dimer rows of the Si terrace with long S_A step edges in agreement with our STM results (Fig. 32) and Refs. [92,99]. Formation of elongated vacancy islands also minimizes the surface energy compared to many small vacancies spread over the terraces. Starting from a surface with preference for A-type terraces (Fig. 31 (d), green areas) the vacancies expand (black arrows) parallel to the step edges uncovering the subjacent B terrace layer (red areas). Broadening of the vacancy island perpendicular to the dimer rows is induced by merging of several islands on a terrace layer. The preferential growth of the vacancy islands parallel to the dimer rows of the corresponding Si layer induces mutually perpendicular expansion of the islands on A- and B-type terraces. Removal of the subjacent Si layer ((Fig. 31 (d), green areas in the vacancy islands) is limited by the width of the vacancy islands in the first layer and suppressed by refilling with diffusing Si adatoms detached from the step edges of the upper (A-type) layer [92,180]. Refilling of subjacent vacancies in the second layer depends on the temperature-dependent mobility of adatoms and the width of the first vacancy island. Only after formation of wide vacancy islands in the first terrace layer, nucleation of vacancy islands in the subjacent Si layer may begin ((Fig. 31 (e)). As a result A- and B-type majority domains continuously alternate, which is directly observed by an oscillating RAS signal. In contrast, oscillating RHEED signals only reflect surface roughening during layer-by-layer removal [98]. The attenuation of the oscillation amplitude with annealing time is likely the result of increasing imperfection of the above process resulting in left-over dimer rows of former terraces.

3.1.3.3 Etch process on Si(100) in H_2 ambient

The in situ RAS measurements enabled us to study the Si etch process in H_2 ambient. From the transient in situ RAS measurements at 3.1 eV, we derived etching rates *k* for Si removal in 950 mbar H_2 ambient dependent on temperature. Data was obtained at constant temperatures (1040 K and 1090 K) and during slow heating ramps (3.3 K/min and 2.5 K/min) from 920 K to 1170 K. Fig. 33 shows the resulting Arrhenius plot from the etching rates k measured in a temperature range between 1040 – 1125 K. Assuming a first order reaction, we applied a linear fit in consideration of x and y errors using the computation method of York (red line) [181]. From the slope of the fit, we calculated an activation energy E_d of 2.75 ± 0.20 eV. Our value agrees within the error margins with data published by Gallois et al., who obtained an activation energy E_d of 3.25 ± 0.43 eV for Si etching in H_2 ambient from rates at 1325 K to 1550 K [101]. Gallois et al. assumed that SiH_2 is the main reaction species in this temperature range. Since our value of E_d is also well below the sublimation energy of Si (4.5 eV [182]), our result indicates Si etching processes by formation of SiH_x species.

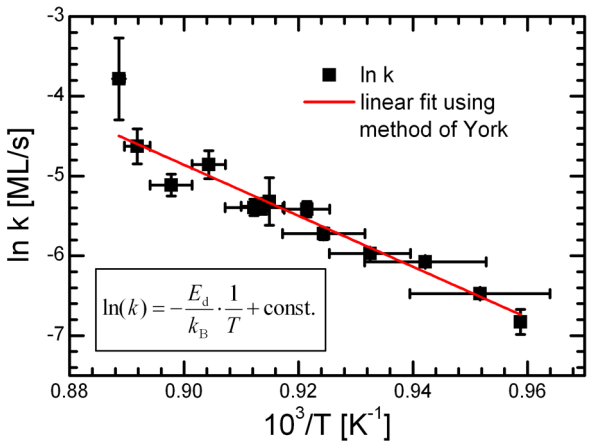

Fig. 33: Arrhenius plot of the etching rate of Si in 950 mbar H_2 from Si(100) surfaces in the temperature range 1040 – 1125 K, determined from RAS transients at 3.1 eV. From the slope of a linear fit using the computation method of York (red line) [181], we determined an activation energy E_d of 2.75 ± 0.20 eV (taken from [172]).

3.1.3.4 Influence of preparation route on domain formation

In situ monitoring of the surface preparation by RAS enabled control of the domain formation on monohydride-terminated Si surface [171]. According to our in situ RAS results (Fig. 31) the preparation route can induce completely different surface domain structures: Fast cooling and lowering of the H_2 pressure (after Si buffer growth and a high temperature annealing step) results in formation of an A-type majority-domain surface (Fig. 31 (b) green line). In contrast, ML removal in the critical temperature range during cooling can induce a B-type majority-domain surface (Fig. 31 (a) red line) or a mixed domain structure depending on exposure time. These findings also imply that nearly exact Si(100) substrates exhibit a prevalence of the A-type domain immediately after Si buffer growth and annealing at 1270 K and 950 mbar H_2. The observation of Si removal during H_2 processing substantiates our model for the formation of the energetically unfavorable D_A steps on vicinal 2° offcut Si(100) substrates, where vacancy diffusion to and annihilation at the step edges leads to a retreat of the B-type terrace after vacancy generation on the terraces (see 3.1.2.4).

The transient RAS measurement showed that Si removal processes in H_2 ambient are crucial for understanding the domain formation of Si(100) surfaces in CVD ambient. The strong dependence of the domain formation on temperature and H_2 pressure induce a highly sensitive surface preparation of nearly exact Si(100) substrates, which requires precise in situ control as the basis for subsequent III-V heteroepitaxy.

3.1.4 In situ control of dimer orientation on Si(100)

We used in situ RAS to monitor the domain formation during CVD processing directly in dependence on the major preparation parameters such as substrate temperature, hydrogen partial pressure, as well as degree of substrate misorientation.

In section 3.1.2, we showed that interaction with the process gas induces Si removal processes and a step structure driven by surface kinetics during processing at high H_2 pressures of 950 mbar. As shown in Fig. 26, the H_2 pressure strongly influences the resulting Si(100) surface termination in dependence on temperature. In order to study the influence of the H_2 pressure on the step formation, we compared RAS, LEED, and STM measurements of 2° Si(100) samples prepared under 50 and 950 mbar H_2 pressure. Transient RAS measurements showed the temperature and H_2 pressure dependent domain formation of Si(100) surfaces.

3.1.4.1 Domain formation in dependence of H_2 pressure

The Si(100) samples were prepared according to our standard Si process (see 2.4.7.1), but differed in the cooling step from 1270 K to 770 K. Fig. 34 (a) shows RA spectra of 2° Si(100) samples after fast cooling (heater off) from an annealing procedure at 1120 K and 50 mbar H_2 pressure (red line), and after slow cooling (~8 K/min) in 950 mbar H_2 pressure (green line) for comparison. The samples exhibit spectra with similar line shape but opposite sign and different intensity. Since RAS is sensitive to the dimer orientation of the monohydride-terminated Si(100) surface, the peak intensity at 3.4 eV corresponds to the domain distribution on the surface [35,171]. Accordingly, the opposite signs of the two RAS peaks indicate mutually perpendicular domain formation: a prevalence of the B domain after preparation in 50 mbar and a prevalence of the A domain after preparation in 950 mbar. Comparison of the RAS peak amplitude at 3.4 eV to Ref. [35] indicates a A:B domain ratio of 37:63 for the 50 mbar sample and an A:B domain ratio of 85:15 for the 950 mbar sample, respectively.

We measured LEED and STM to investigate the domain and step structure on the differently prepared surfaces (Fig. 34 (b), (c)). As already shown in section 3.1.2, the STM images of the 950 mbar sample exhibit mainly A-type terraces with dimer rows parallel to the step edges and few small B-type terraces, i.e. a D_A-stepped surface (one example indicated by white arrow). The corresponding LEED pattern confirms an A-type

majority domain on the surface by a clear (1×2) symmetry (see encircled half order spots).

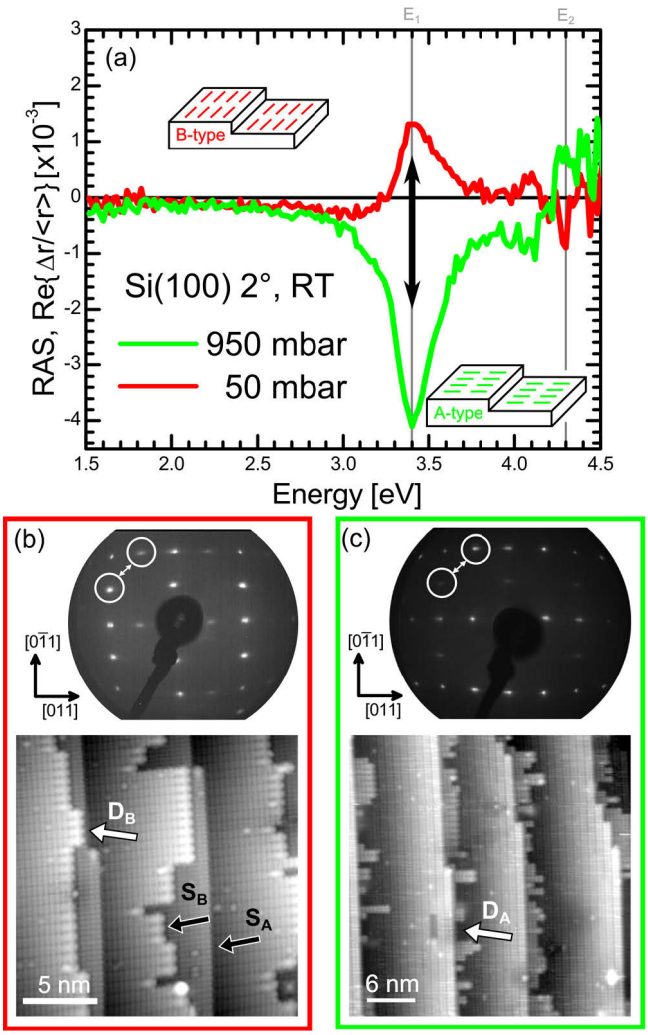

Fig. 34(a)-(c): RA spectra and corresponding LEED and STM data of Si(100) with 2° misorientatin in [011] direction after cooling procedure from 1270 K to 770 K in 50 mbar (red) and 950 mbar (green) H_2 pressure (for details see text).

In contrast, stronger intensities of the half order spots in [0$\bar{1}$1] direction in the corresponding (2×1)/(1×2) LEED pattern of the 50 mbar sample indicate a preference for the B-type terraces (Fig. 34 (b)). In agreement, the STM image exhibits mainly B-type terraces and a step structure consisting mainly of S_A and S_B single-layer steps (examples indicated by black arrows) and few D_B steps (one example indicated by white arrow).

According to our RAS, LEED, and STM analysis, Si(100) 2° surfaces exhibit a preference for the A- and B-type surface reconstruction domain depending on preparation in 950 or 50 mbar, respectively, which confirms the strong influence of the H_2 pressure on the Si(100) surface formation in the CVD reactor.

3.1.4.2 In situ observation of domain formation at low H_2 pressure

In analogy to the experiment described in section 3.1.2, we studied the domain formation at a reactor pressure of 50 mbar in dependence on temperature by domain-sensitive transient in situ RAS measurements. Fig. 35 shows transients measured at 3.1 eV (corresponding to the characteristic RAS peak at 3.4 eV of Fig. 34 in the given temperature range) during heating and cooling between 920 K and 1120 K (1.5 K/min). Starting from a surface with a preference for the A-type domain, the amplitude of the RAS signal decreases during heating (orange line) for T > 970 K. Above 1020 K the RAS signal exhibits a positive sign. With increasing temperature, the RAS signal slightly decreases to a value close to zero at 1120 K. During cooling from 1120 K down to 920 K (blue line), the sign of the RAS signal stays positive. The magnitude increases slightly with decreasing temperature reaching a maximum value around 1020 K and reduces again during further cooling.

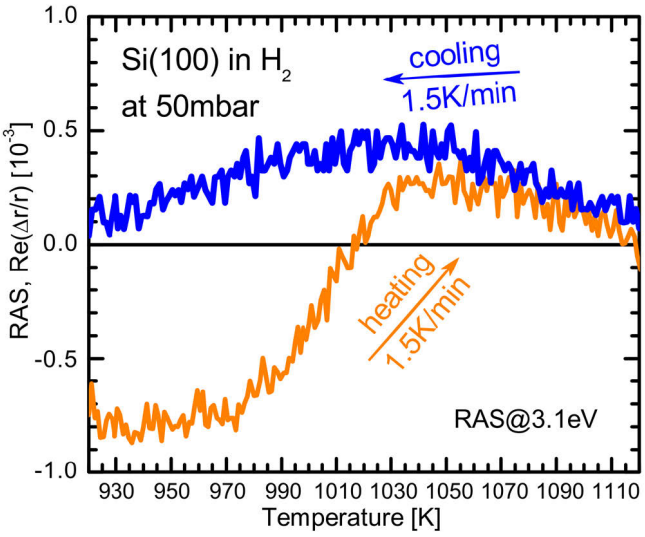

Fig. 35: Transient RAS at 3.1 eV (corresponding to the characteristic RAS peak at 3.4 eV of Fig. 34) during heating and cooling (1.5 K/min) between 920 and 1120 K in 50 mbar H_2.

According to the transient during heating, the initial surface domain structure remains stable until 970 K. Below T = 970 K, the monohydride termination likely reduces diffusion of adatoms and vacancies [103], similar to the experiments under 950 mbar H_2 (section 3.1.2). On heating above 970 K, diffusion sets in with decreasing hydrogen passivation and the A-type majority domain is reduced, and above 1020 K, the surface starts to form the B-type majority domain which agrees with expectations regarding surface energetics [17]. The reduced pressure leads to weaker H_2 interaction which induces less Si removal. The reduction in the RAS amplitude above 1050 K could be due to decreasing monohydride termination which corresponds to about 50 % in this temperature range (see Fig. 26) [31]. Since the development of the RAS signal is similar during heating and cooling above 1020 K, the surface is in an equilibrium state. The reduction of the B-type domain during cooling below 1000 K may correspond to remaining interaction of Si with H_2 and smaller stability of the B-type terraces.

Temperature and H_2 pressure control the hydrogen termination of the Si(100) surface as well as the resulting surface structure. At high H_2 pressures (950 mbar) the strong interaction leads to Si removal and vacancy generation in the critical temperature range (T = 970 – 1120 K) as shown by transient in situ RAS measurements on nearly exact Si(100) substrates (see section 3.1.2). Vacancy generation, diffusion, and annihilation at step edges form the energetically unfavorable D_A steps. Reduced pressure (50 mbar) leads to weaker H_2 interaction which induces less Si removal. Diffusion of Si atoms still occurs leading to formation of an energetically favorable surface state. Consequently, the surface exhibits a prevalence of the B-type terrace and mainly S_A and S_B steps as expected for a monohydride terminated Si(100) surface from UHV-based studies [17] and theory [18], [19]. The remaining interaction of H_2 process gas with the Si(100) surface might lead to reduced B-type domain formation compared to UHV preparation during further heating or cooling.

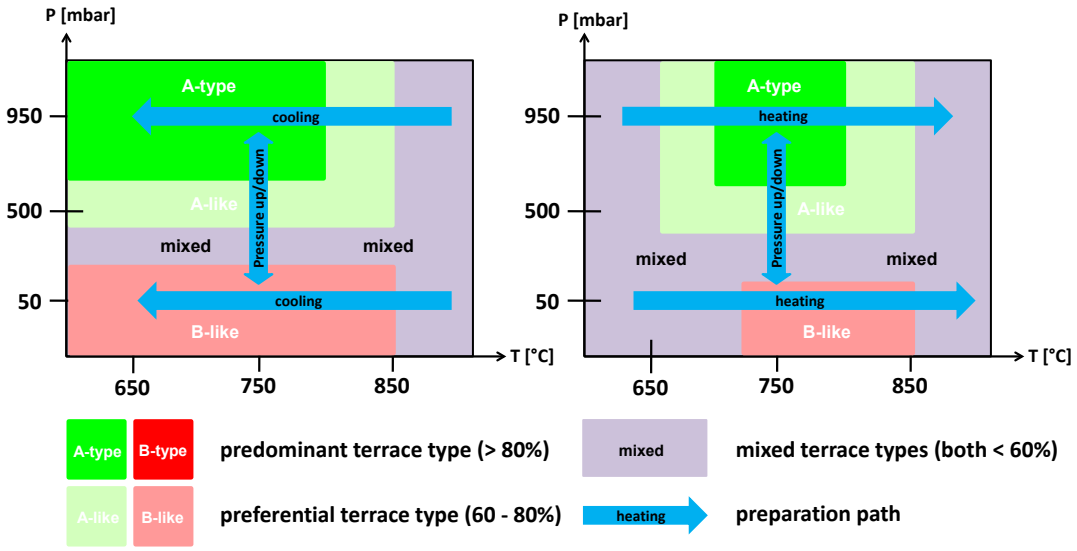

Fig. 36: Preparation diagram for the domain formation on Si(100) in dependence on temperature, H_2 pressure and preparation route as a summary of the findings from the RAS experiments. Green areas indicate formation with preferential A domain and red areas with preferential B domain, respectively. The intensity of the colors reflects the value of the prevalent domain. Blue arrows indicate the change of a process parameter (after [174]).

Since the domain formation is a reversible process, we can control the preferential domain type on the Si(100) surface by setting the respective H_2 pressure in the critical temperature range. The resulting domain formation deduced from the transient in situ RAS measurements (Fig. 30, Fig. 35) can be summarized in "preparation diagrams". The preparation diagram in Fig. 36 shows the domain formation for Si(100) 2° surfaces in dependence on H_2 pressure and temperature during processing in CVD ambient as well as preparation route (heating and cooling, pressure up/down).

3.1.4.3 Domain formation on high offcut substrates

The aforementioned results show the influence of the crucial process parameters such as *T*, *p*, *t* on the domain and step structure of Si(100) surfaces. Now, we study the preparation on substrates with high step density. Comparison of results obtained on nearly exact and 2° offcut substrates obtained after identical processes already show distinct differences in the surface structure due to the different step density and terrace width (see

section 3.1.3.4). While formation of vacancy islands on the terraces dominates the resulting surface structure on nearly exact Si(100) surfaces (see 3.1.3), vacancy annihilation processes at the step edges become more probable on substrates with higher step densities (see 3.1.2) during preparation under high H_2 pressure. As a result we observed a domain formation driven by surface kinetics. In contrast, the step structure on the surface arranges itself in the energetically most favorable configuration during preparation under low H_2 pressure (see 3.1.4.1).

For clean vicinal Si(100) substrates with higher offcut (> 2.5°) the formation of B-type single domain surfaces with D_B double-layer steps presents the energetically most favorable step configuration [16]. Preparation of substrates with high step density in H_2 process ambient may induce a strong competition between surface energetics and kinetic processes which influence the step and domain formation. Here, we studied the surface preparation of vicinal Si(100) substrates with 6° offcut under high and low H_2 pressures. RAS enabled in situ characterization of the domain distribution during MOCVD processing, while STM revealed the corresponding steps structure.

Sample preparation consisted of our standard process as described in 2.4.7.1, but differed in the subsequent cooling procedure from 1270 K to 770 K after the annealing step. The B-type sample was cooled fast (heater off) at 50 mbar H_2 pressure, while the A-type sample was cooled slowly (~8 K) at 950 mbar H_2 pressure, analogous to the sample in 3.1.2.1.

Fig. 37 shows RAS signals of both samples as well as the corresponding LEED and STM measurements. The 50 mbar sample exhibits the same RAS signal as shown in Fig. 24 after deoxidation with the characteristic “derivative”-like features at the CP energies E_1 and E_2 at 3.4 and 4.2 eV, respectively. The RAS signal agrees very well with spectra of monohydride terminated vicinal Si(100) surfaces with a B-type majority domain and D_B steps [31] which is confirmed by the corresponding (2×1) LEED pattern and STM image.

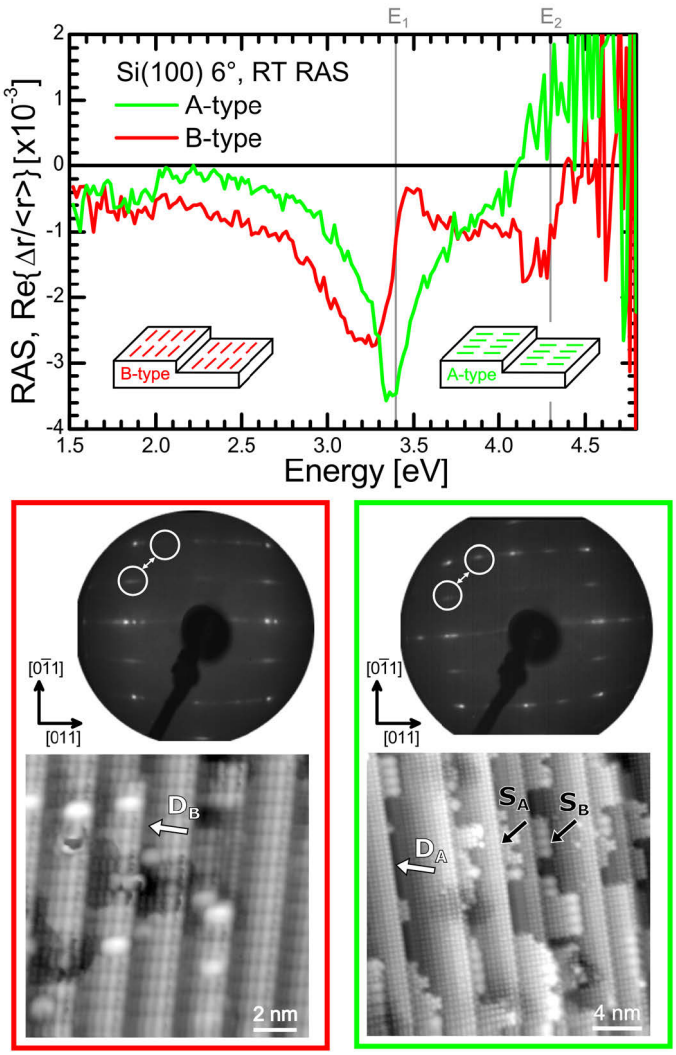

Fig. 37: (a) RAS of Si(100) 6° samples prepared by slow cooling in 950 mbar and fast cooling in 50 mbar H_2 pressure after our standard Si process. (b) and (c) presents the corresponding LEED and STM measurements.

In contrast, the 950 mbar sample exhibits a spectrum which agrees with the characteristic RAS signal of a monohydride terminated Si(100) surface with a prevalence of the A-type domain indicated by the strong negative peak-like feature at 3.4 eV. The corresponding (2×1)/(1×2) LEED pattern confirms an A-type majority domain by stronger intensities of the half order spots in the [011] direction (see circles). In the STM image of the 950 mbar sample, we observe a slight majority of A-type terraces with long, straight step edges towards the lower terrace and residual B-type terraces with frayed step edges. The surface

exhibits an irregular step structure with mainly D_A, S_A and S_B steps, as well as some D_B steps.

According to the results shown above, we are able to prepare vicinal Si(100) samples with prevalence for the A- and the B-type domain depending on the annealing conditions in H_2 ambient (T, p, t). During preparation under high H_2 pressure the surface exhibits a tendency towards D_A steps and A-type majority domain formation due to the strong interaction between H_2 and the Si surface, which induces a step formation mechanism based on kinetic process on the surface (see 3.1.2.4). In contrast, preparation under low H_2 pressure results in the energetically governed D_B double-layer step formation due to reduced interaction between process gas and surface. In comparison to the similarly prepared 2° Si(100) sample (Fig. 32), the formation of the A-type domain is much less pronounced on the 6° sample, whereas the B-type domain formation is stronger here. Step formation energetics with their tendency for D_B steps on Si(100) surfaces with high offcut competes with the kinetically driven D_A step formation.

Remarkably, the 6° Si(100) sample exhibits different RAS signals for the monohydride terminated surface with A- or B-type majority domain, which is in contrast to the RAS signals observed on the nearly exact or 2° offcut samples. This observation is important for the understanding of the origin of the RA spectra. Both contributions from the terraces (i.e. surface reconstruction) and the steps have to be considered which are affected by the hydrogen termination in our case. The RAS signal of the terraces is well understood for clean and monohydride terminated Si(100) [35]. While experimental and theoretical studies indicate relevant contribution of the steps to the clean Si(100) RAS signal of vicinal substrates [24,32], step contributions to the RAS signal are unclear for the monohydride terminated Si(100) surface. In particular, Ref. [35] reports on a very similar RAS signal for the dihydride terminated nearly exact surface and the monohydride terminated vicinal Si(100) surface.

The RAS signals of vicinal Si(100) substrates with high offcut are suitable for monitoring the domain formation on Si(100) surfaces during preparation in process gas ambient of a MOCVD system.

3.2 Germanium (100) surfaces

Vicinal Ge(100) is the common substrate for high-efficiency triple junction solar cells, since the material is lattice-matched to the subsequent III–V subcells to be grown by MOCVD [1]. Both structural and chemical properties of Ge(100) surfaces are essential for epitaxial growth, but the process gas ambient limits the direct access to surface analysis. Present knowledge about Ge(100) surfaces is mostly based on characterization in ultra-high vacuum (UHV).

In this work, the Ge(100) surface preparation in MOCVD environment was studied in detail where only scarce reports are available in literature. This involves preparation and characterization of clean Ge(100) surfaces after annealing in H_2 ambient, interaction between Ge(100) and H_2 process gas, as well as influence of arsenic and phosphorous exposure of Ge(100) on the surface structure (published in [183–186]).

3.2.1 Ge(100) surface preparation in H_2 ambient

As a starting point, we first discuss the preparation of a clean Ge(100) surface in MOCVD ambient. MOCVD processing of Ge(100) usually begins with thermal substrate annealing under hydrogen flow for oxide removal. According to UHV results [187,188], temperatures of about 720 – 770 K are sufficient, but carbon impurities may remain on the Ge(100) surface and influence the formation of a regular step structure [189,190]. In UHV, the exposure of Ge(100) to atomic hydrogen leads to the formation of a (2 × 1) reconstructed monohydride surface [165]. In sections 2.5.3 and 3.1.1, we have shown the strong interaction of Si(100) with molecular hydrogen under MOCVD process conditions, but no similar studies for the Ge(100) surface are available. RAS enables in situ characterization of substrate surfaces during MOCVD processing [21]. Refs. [36,37] show RA spectra of UHV-prepared, clean Ge(100) with 4° and 6° misorientation in [011] direction, respectively.

Here, we thoroughly analyzed the chemical and structural surface properties of MOCVD prepared Ge(100), and discussed its characteristic in situ RA spectra. Annealing in H_2 ambient removed oxides and carbon from the Ge(100) substrates as confirmed by XPS. While LEED showed the typical, dimer-based surface reconstruction of Ge(100), FTIR spectroscopy revealed the presence of a monohydride termination after H_2 annealing.

3.2.1.1 Oxide removal and preparation of clean Ge(100)

We used Ge(100) substrates with a misorientation of 6° towards the [011] direction specified as "epiready" (supplier: AXT) and specific samples (CrysTec) for FTIR [165]. As described in 2.4.7.2 samples were prepared by annealing at 970 K and 100 mbar H_2 pressure for 20 min.

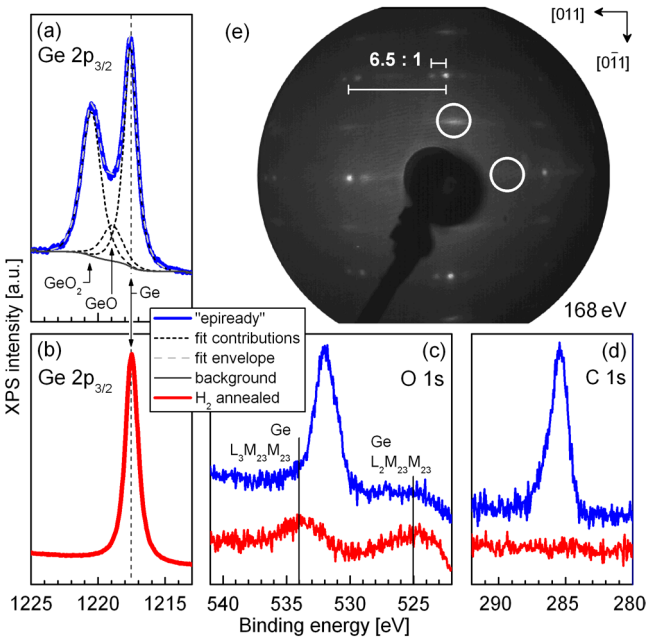

Fig. 38: XP spectra of Ge(100) "epiready" (blue) and after H_2 annealing (red) in the range of the Ge $2p_{3/2}$, O 1s and C 1s PE line with corresponding LEED pattern of the deoxidized surface (taken from [183]).

Fig. 38 (a)–(d) shows XP spectra in the range of the Ge $2p_{3/2}$, O 1s and C 1s photoemission lines of an "epiready" Ge(100) substrate and of its surface after H_2 annealing in MOCVD. The influence of band bending was corrected in the XPS data by

matching the energetic positions of the elemental Ge PE signals between the samples [147]. In the Ge $2p_{3/2}$ XP spectrum (Fig. 38 (a)), the "epiready" Ge substrate exhibits peaks at 1217.5 eV and 1220.5 eV that correspond to elemental and oxidized Ge, respectively [187,188]. Deconvolution of the oxide peak (Fig. 38 (a), dotted lines) revealed main contributions from GeO_2 and smaller ones from GeO, that are shifted about +3.0 eV and +1.7 eV with regard to the elemental Ge $2p_{3/2}$ line [187]. Broad peaks at around 531 and 285 eV arise from oxygen (O 1s) and carbon (C 1s), respectively (Fig. 38 (c), (d)).

The absence of both the O 1s line and the signal associated with GeO_x confirmed oxide removal during annealing in H_2. Remaining smaller peaks at about 534 eV and 525 eV are assigned to the $L_3M_{23}M_{23}$ and $L_2M_{23}M_{23}$ Auger emission lines of elemental Ge, respectively [191], also present as shoulders in the oxide spectrum. Within the sensitivity limits of our XPS setup (<1% of a monolayer), we detected no traces of impurities after annealing, neither carbon nor group III or V elements. According to Refs. [189,190], residual carbon can only be partially removed from the Ge(100) surface by thermal annealing in UHV. In contrast, our results indicate sufficient carbon removal during thermal deoxidation (Fig. 38 (d)). The absence of C 1s intensity in our spectra can be explained either by the specific surface conditioning of the supplier ("epiready"), or by a reaction with H_2 producing volatile CH_x species, or a combination of both.

The LEED pattern of the deoxidized Ge(100) surface (Fig. 38 (e)) shows pronounced spot splitting along [011]. In consistence with UHV studies [192], half-order spots in [011] direction indicate dimer formation on the surface and a clear prevalence (compare encircled half-order diffraction spots) of the domain with dimers parallel to the step edge – corresponding to a preference for D_B-type double layer step formation typical for vicinal Ge(100) surfaces [87]. The LEED spot splitting ratio of about 1:6.5 compared to the distance of full-order reflexes is in good agreement with the strong vicinality of the 6° offcut Ge(100) substrate. Assuming double layer step formation, we expect an average terrace width of 2.7 nm (≙ 6.7 atomic distances in the surface plane). Residual disorder in the LEED pattern is most probably due to irregularities of the step structure. In analogy to

Si(100) [18], dimerization occurs on both clean and monohydride Ge(100) surfaces, and our LEED pattern does not distinguish between these terminations.

3.2.1.2 Direct evidence for monohydride termination on Ge(100)

We carried out ATR mode FTIR measurements to check for hydrogen termination after annealing and cooling in H_2 ambient. The FTIR spectrum in Fig. 39 shows two characteristic absorption lines at about 1986 and 1975 cm^{-1} assigned to coupled Ge–H stretch modes [165]. Hydrogen saturation of the residual dangling bonds of the reconstructed Ge(100) creates H–Ge–Ge–H dimers. Their antisymmetric and symmetric vibrational modes induce dipoles within and perpendicular to the surface plane, respectively. Since polarized FTIR measurements can address dipole orientations on the surface [13], we currently work on a quantitative analysis of surface reconstruction domains on Ge(100).

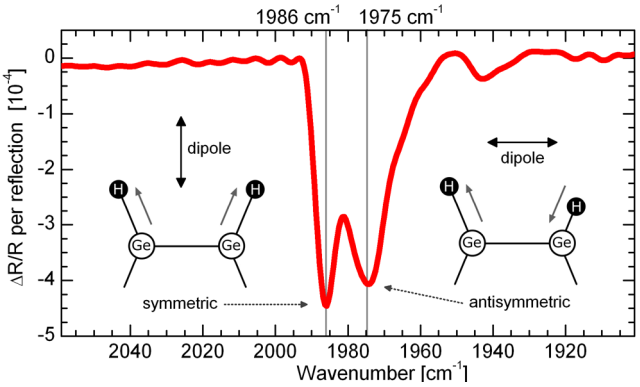

Fig. 39: FTIR spectra measured in an ATR configuration at H_2 annealed Ge(100). Clear features at 1986 and 1975 cm^{-1} agree with the symmetric and antisymmetric stretch modes of coupled Ge–H monohydrides, respectively [165] (taken from [183]).

3.2.1.3 RA spectrum of vicinal Ge(100):H

Fig. 40 shows RA spectra of "epiready" and H_2 annealed vicinal Ge(100) measured in the MOCVD reactor at 320 K (after cooling in H_2 ambient) as well as the RA spectrum of clean vicinal Ge(100) prepared in UHV [37] for comparison. Due to coverage with an amorphous oxide layer, the "epiready" surface exhibits a featureless spectrum. After H_2

annealing in the MOCVD reactor, we observe a characteristic RAS signal of the Ge(100) surface (Fig. 40, red line) consisting of a broad minimum around 3 eV and a narrow one at 1.9 eV as well as local maxima around the CP energies of Ge(100) (E_1 and $E_1 + \Delta_1$ at about 2.2 eV and E_2 at 4.3 eV, respectively). Although the general features of the observed RA spectrum roughly agree with the RAS signal of clean Ge(100) prepared by annealing in UHV [37], the local maximum around 2.2 eV is more pronounced and the minimum around 3 eV is shifted slightly towards higher energies. In contrast to Ref. [37], we observed additional fine structure of the RAS signal, particularly around 3.4 eV and 4.0 eV (arrows in Fig. 40).

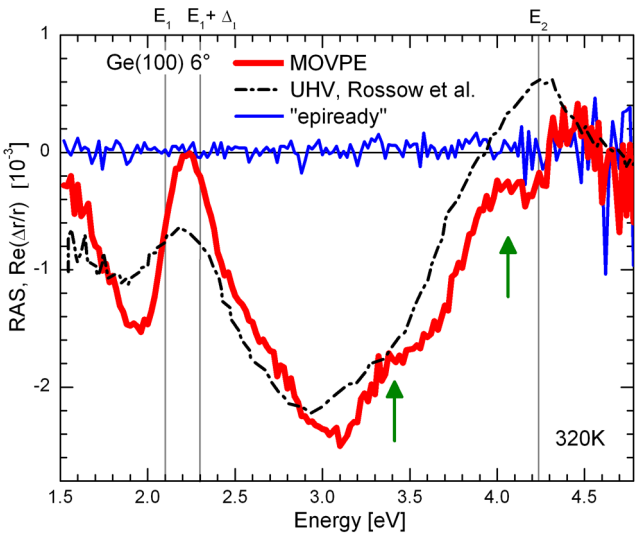

Fig. 40: In situ RA spectra of "epiready" (blue) and H_2 annealed (red) Ge(100) with 6° miscut in [011] measured at 320 K in H_2 ambient, and RAS of UHV-prepared Ge(100) (dash-dotted) [37] (taken from [183]).

In general, differences in the atomic order of probed (100) surfaces such as cleanliness, surface reconstruction, domain ratio, and chemical configuration affect shape and amplitude of RA spectra [176]. If the signal originates from the surface reconstruction, the presence of mutually perpendicular reconstruction domains results in a linear reduction of the amplitude [25]. The impurity concentration on the surface mainly affects the signal intensity, too [36]. In contrast, hydrogen saturation of dangling bonds [165] usually changes the shape of the RAS signal as observed for monohydride termination on vicinal Si(100) [31]. Since our findings exclude significant contamination of our

MOCVD prepared Ge(100) surfaces (Fig. 38) and confirm the presence of monohydride dimers (Fig. 39), we assume that both the more pronounced signal shape between 1.8 eV and 2.3 eV and the additional fine structure beyond 3 eV are characteristic of the monohydride Ge(100) surface. The limited stability of the hydrogen bonds [84] should enable us to prepare clean Ge(100) by thermal hydrogen desorption under flow of alternative process gases such as N_2 or Ar [148]. The confirmation of characteristic RA spectra which distinguish between both surface configurations of Ge(100) will enable dedicated in situ investigations of hydrogen adsorption and desorption characteristics on Ge(100) in dependence on temperature, pressure, and process gas in the MOCVD reactor similar to the results on Si(100) (see section 3.1.1).

3.2.2 Interaction of Ge(100) with H_2 process gas

Since processing in H_2 ambient results in formation of monohydride termination on Ge(100) surfaces [183], we studied the interaction between Ge(100) surface and H_2 process gas ambient, which is not well understood in literature. H desorption kinetics have been studied in UHV environment by several experimental methods [83–85]. Hydrogen desorbs from the Ge(100) surface at temperatures in the range of 500 K following first order kinetics [84,85].

In process gas ambient, RAS enables in situ surface characterization of vicinal Ge(100) surfaces. According to the results in section 3.2.1 [183], the characteristic differences in the RAS signal of the MOCVD prepared Ge(100) surface to the clean surface [36,37] might be related to the monohydride termination.

In this section, we provide experimental evidence for the sensitivity of RAS to hydrogen termination by monitoring the RAS signal during thermal annealing of a monohydride-terminated Ge(100) surface in N_2 ambient. The obtained RA spectra were correlation to various other surface sensitive tools accessed by a dedicated MOCVD-to-UHV transfer system. In situ RAS enabled us to study hydrogen desorption kinetics on the Ge(100) surface by performing successive H isothermal desorption experiments in agreement with

results from literature as well as interaction of Ge(100) with H_2 process gas during MOCVD preparation. While in situ RAS allows direct observations of changes related to hydrogen termination on the Ge(100) surface in any process environment including MOCVD, LID, STM ,and TPD are only applicable in UHV environment.

3.2.2.1 RA spectra of clean and monohydride terminated Ge(100)

We used Ge(100) substrates with a misorientation of 6° towards the [011] direction. Without any additional wet chemical pre-cleaning, the preparation was carried out in two different Aixtron AIX-200-4 MOCVD reactors located in Madrid and Berlin, both equipped with an in situ RA spectrometer (LayTec EpiRAS 200). The comparability between the experiments in both reactors was ensured by identical RA spectra for identically prepared Ge(100) samples. Reactor parts (liner, susceptor) and sample carriers were cleaned of III-V residues to avoid unintentional contamination of the samples. The samples were prepared as described above by annealing at 1000 K for 20 min in purified H_2 at a pressure of 100 mbar. As shown in the previous section the Ge(100) surface is monohydride terminated if cooled down in H_2 ambient after the deoxidation process.

Fig. 41 shows the RA spectrum of the monohydride terminated surface (thin red line). It consists of a broad and a narrow minimum around 3.0 eV one 1.9 eV, respectively, local maxima around the critical point (CP) energies of Ge(100) (E_1 and $E_1+\Delta_1$ at around 2.2 eV and E_2 at 4.3 eV) as well as two characteristic shoulders around 3.4 and 4.2 eV. The corresponding STM image (inset Fig. 41) shows a regular step structure with symmetric dimers on the terraces. The step height equals two atomic layers and the dimers are parallel to the step edges on adjacent terraces, i.e. the surface is preferentially D_B-stepped. The observed (2×1) surface reconstruction indicates a rather complete monohydride termination of the Ge(100) surface, since there are no areas with a c(4×2) or p(2×2) surface reconstruction due to buckled dimers, which is typical for clean Ge(100) surfaces [61,87]. However, the bright ball-like features most probably correspond to missing H atoms [85,193].

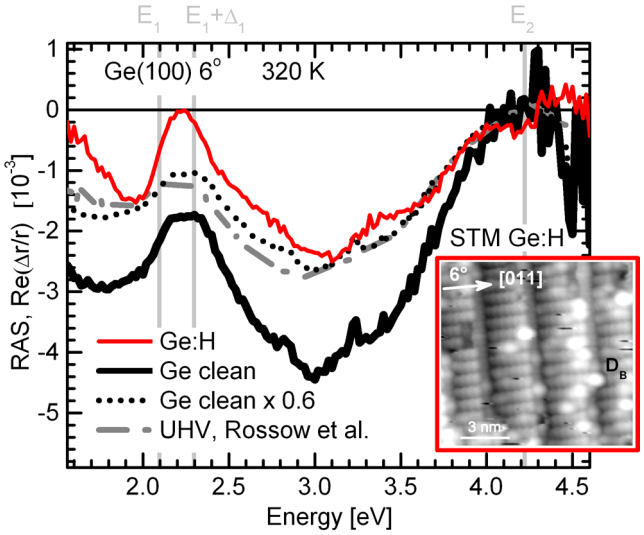

Fig. 41: In situ RA spectra of the monohydride-terminated (thin red line) and the clean (thick black line) Ge(100) surface with 6° offcut towards the [011] direction prepared in MOCVD ambient. The dash dotted gray line represents the RA spectrum of a UHV-prepared Ge(100) surface and the dotted black line corresponds to the clean MOCVD-prepared Ge(100) surface (thick black line) scaled by 0.6. The vertical lines indicate the critical points energies of Ge(100) at 320 K. The STM image (V_{sample} = -1201.2 mV, I_t = -0.65 nA) corresponds to the monohydride-terminated Ge(100) surface and shows a preferentially (2×1)-reconstructed surface with D_B-type double-layer steps (taken from [184]).

Fig. 41 also shows the RA spectrum after annealing the originally monohydride terminated surface under N_2 at 573 K and cooling to RT. The RA spectrum has similarities to the RA spectrum of the monohydride terminated Ge(100) surface. The local minimum around 1.8 eV and the maximum at 2.2 eV are shifted towards lower RAS values, the broad minimum around 3.0 eV is much more pronounced. While a shoulder is present at 3.2 eV similar to the shoulder of the RA spectrum of the monohydride terminated Ge(100) surface at 3.4 eV, we observe no additional fine structure at the local maximum at the E_2 CP.

We carried out FTIR measurements in ATR mode to directly check for hydrogen termination after annealing in N_2 ambient. While FTIR measurements performed on monohydride-terminated Ge(100) surfaces displayed two characteristic absorption lines at 1986 and 1975 cm^{-1} (see Fig. 39), no absorption lines appeared in the spectra after annealing in N_2 (not shown here), which indicates a H-free surface. XPS measurements

also confirmed the absence of any contaminants on the Ge(100) surface, in particular related to nitrogen or carbon. Hence, the RAS signal measured after N_2 annealing corresponds to the clean and H-free vicinal Ge(100) surface, obtained by thermal hydrogen desorption from the monohydride terminated surface in an inert gas ambient.

Fig. 41 compares the RAS signal of the clean Ge(100) surface prepared in MOCVD (dotted black line in Fig.1) and UHV environment (dash-dotted thin gray line) [37]. If we shift and apply a scaling factor of 0.6 to the RA spectrum obtained after annealing in N_2, the spectrum largely overlaps with the RA spectrum of the clean UHV-prepared Ge(100) surface. The difference in RAS amplitude between the samples might be due to coexistence of domains with mutually perpendicular dimer orientations [177], [27] or due to a better surface cleanliness of the sample prepared in MOCVD ambient, since many studies report on the inevitable presence of C on UHV-prepared Ge(100) surfaces [36,189,190].

3.2.2.2 H_2 desorption kinetics at Ge(100)

Since the clean and the monohydride terminated Ge(100) surface exhibit characteristic RAS signals, we applied in situ RAS for analysis of the hydrogen surface coverage during preparation in the process gas ambient of a MOCVD reactor. Fig. 42 (a) shows continuous RAS measurements during annealing of an initially monohydride terminated Ge(100) surface (thick red line) in N_2 ambient (100 mbar) at 523 K. The first spectrum was taken under H_2 process gas and shows the corresponding monohydride RAS signal (red line). After switching the process gas to N_2 (without changing the temperature) we observe a successive transformation of the RAS signal with time (thin gray lines) to the characteristic RAS signal of the clean vicinal Ge(100) surface, only governed by the temperature dependent hydrogen desorption rate. The change in the RAS signal is complete after 60 min (thick black line), indicating the end of the H desorption from the Ge(100) surface. Upon resupplying H_2, the RAS signal of the monohydride terminated Ge surface reemerges again within a few minutes (not shown here). Consequently, the sensitivity of RAS to the hydrogen termination of vicinal Ge(100) allows us to study the

hydrogen desorption and adsorption characteristics dependent on varying process conditions.

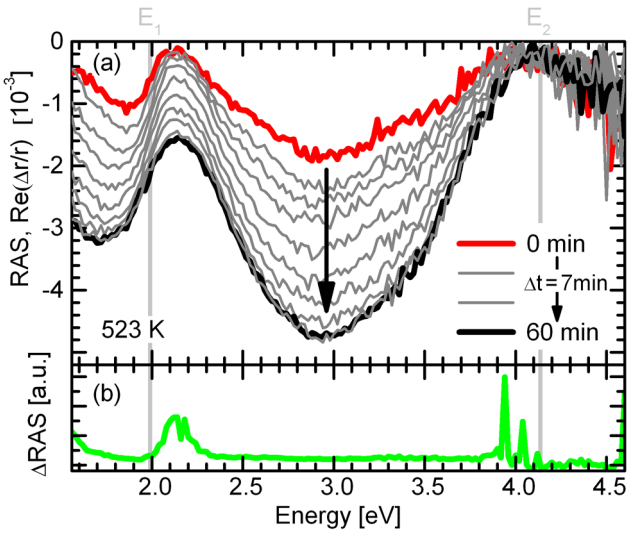

Fig. 42 (a): In situ RAS measurements (thin gray lines) during hydrogen desorption from vicinal Ge(100). Switching the process gas from H_2 (t = 0 min) to N_2 at the constant temperature of 523 K, induces successive H desorption and the monohydride RAS signal (red line) transforms (grey lines) into the RAS signal of the clean Ge(100) surface which is completely evolved after 60 min (black line). (b): Relative difference between the RAS signal of the monohydride terminated (red line) and the clean surface (black) ΔRAS = [(RAS_{60min} – RAS_{0min})/RAS_{0min}] (taken from [184]).

In order to perform detailed kinetic studies of hydrogen desorption, it is essential to use a RAS signal (at a given photon energy) that fully reflects the hydrogen termination. Features in the RA spectra are a result of an anisotropic electronic structure which may arise from the reconstructed surfaces at cubic crystals and can involve both surface states and surface modulated bulk states [20,194]. Since there was no theoretical analysis available for the RAS signal of the Ge(100) surface, we empirically analyzed the different contributions in the RA spectrum. Fig. 42 (b) shows the relative difference ΔRAS = [(RAS_{60min} – RAS_{0min})/RAS_{0min}] between RAS of the clean surface (black line) and the monohydride terminated surface (red line) in Fig. 42 (a). This plot shows whether the hydrogen termination equally affects the shape of the RA spectrum. In that case, we would get a constant ΔRAS over energy (i.e. a straight line in Fig. 42 (b). However, ΔRAS shows a peak centered at 2.1 eV (around the E_1 critical point) and a wide plateau centered around 3.0 eV. The peaks at higher energies are an artifact of the calculation,

since the RA spectra of both the monohydride and the clean surfaces are very similar and close to zero.

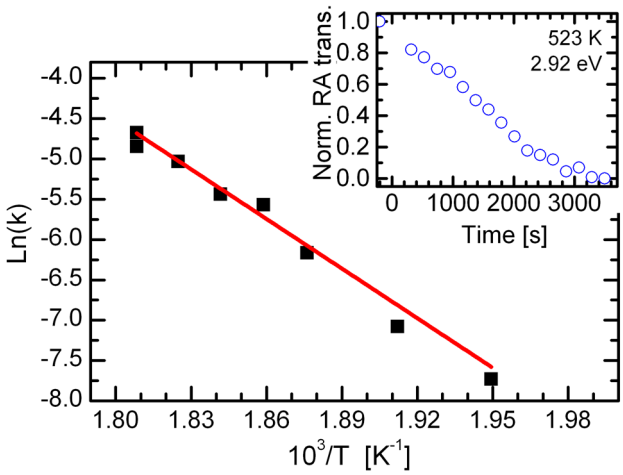

Fig. 43: Arrhenius plot of the H_2 desorption from Ge(100) surface in the temperature range 513 – 553 K, as determined from the RAS transients at 2.92 eV. The inset shows the normalized RA transient at 2.92 eV corresponding to the data of Fig. 42 (taken from [184]).

In UHV, hydrogen desorption from monohydride terminated Ge(100) surfaces follows a first-order reaction [83–85], where the rate equation is:

$$\frac{\mathrm{d}S}{\mathrm{d}t} = -\kappa S = -\nu_\mathrm{d} \exp\left(-\frac{E_\mathrm{d}}{k_\mathrm{B}T}\right) S, \qquad \textbf{Eq. 10}$$

with S being the hydrogen related signal, κ the first-order rate constant, E_d the activation energy and ν_d the preexponential factor. In order to estimate E_d and ν_d, we conducted isothermal H desorption measurements for several temperatures in the range of 513 – 573 K. We analyzed the temporal development of the spectra (hereinafter RA transient mode) for a photon energy of 2.92 eV (center of wide plateau in Fig. 42 (b)), assuming that the decay of the RAS amplitude corresponds to the loss in hydrogen coverage. Below, we compare the results to the same analysis performed at 2.12 eV (the peak in Fig. 42 (a)) and other photon energies. Accordingly, we use the normalized RA transient as the hydrogen related signal (S) in Eq. 10. We assume roughly 1 ML hydride coverage

($S = 1$) prior to desorption in N_2, since the RAS signal saturates to a constant value when H_2 is resupplied and neither dihydride formation nor relevant amounts of single dangling bonds have been detected with FTIR (see Fig. 39) and STM, respectively. We also assume no hydrogen coverage ($S = 0$) when the RAS signal saturates after H desorption in N_2.

The inset of Fig. 43 shows the normalized RAS transient at 2.92 eV taken from the in situ RAS measurements in Fig. 42 (a). The transient shows a non-single-exponential decay (in contrast to Refs. [168] and [169]) probably due to hydrogen readsorption [195], which depends on the relative magnitudes of the chemisorption rate, desorption rate, and pumping speed [195]. Therefore, we only used the $dS/dt = -\kappa S$ to obtain the rate constants κ only for $S < 0.5$, where readsorption effects are reduced [195]. The resulting Arrhenius plot of κ for this temperature range (Fig. 43) is linear over two orders of magnitude in the desorption rate, similar to Ref. [85]. From the slope and intercept of the best fit to the experimental data, we calculated $E_d = (1.8 \pm 0.2)$ eV and $\nu_d = 1 \times 10^{14\pm1}$ s^{-1}, respectively. These values are in good agreement with the data published in literature for hydrogen desorption from Ge(100) measured in other process environments by different experimental techniques [84,85,195].

Tab. 1: Comparison of the kinetic parameters for the H desorption from Ge(100) surface obtained from the RAS transients at different photon energies (taken from [184]).

Photon energy (eV)	E_d (eV)	ν_d (s^{-1})
1.72	1.7 ± 0.2	$6 \times 10^{13\pm1}$
2.12	1.3 ± 0.2	$3 \times 10^{09\pm1}$
2.52	1.8 ± 0.2	$8 \times 10^{13\pm1}$
2.92	1.8 ± 0.2	$1 \times 10^{14\pm1}$

We conducted the same analysis at 1.72, 2.12 and 2.52 eV (i.e. representative energies of the features observed in Fig. 42 (b)), the corresponding results are summarized in Tab. 1. Both E_d and ν_d for 1.72, 2.52 and 2.92 eV agree well with each other within the error estimation and, in particular, with values reported in literature [84,85,195], whereas the activation energy obtained at 2.12 eV (around the E_1 CP of bulk Ge) strongly deviates. Consequently, we suggest that the change in the minima at 1.8 and 3.0 eV between the RA spectra of the clean and monohydride-terminated Ge(100) surfaces (thick black and

thin red lines in Fig. 41) is directly related to hydrogen coverage. In contrast, the change in the local maximum at 2.1 eV is only partially related to hydrogen coverage. In other words, these findings indicate that the RAS signal of the clean Ge(100) surface is differently affected by H termination, as already expected from ΔRAS in Fig. 42 (b).

3.2.2.3 H termination of Ge(100) during processing

The desorption experiments at 513 – 553 K (Fig. 42) indicate strong interaction between process gas and Ge(100) surface similar to our observation on the Si(100) surface (see section 3.1.1). Annealing in the presence of H_2 leads to dissociative adsorption and desorption at the Si(100) surface depending on H_2 pressure as well as temperature of the process gas and the substrate surface [80]. Accordingly, the hydrogen termination varies during preparation in MOCVD ambient in dependence on the process parameters (see Fig. 25). We expect a similar behavior of the Ge(100) surface during preparation in H_2 ambient. Since the clean and the monohydride terminated vicinal Ge(100) surfaces exhibit characteristic RAS signals, we are able to study the hydrogen coverage of Ge(100) samples during preparation in the process gas of a MOCVD reactor, analogous to the experiments with Si(100) (section 3.1.1).

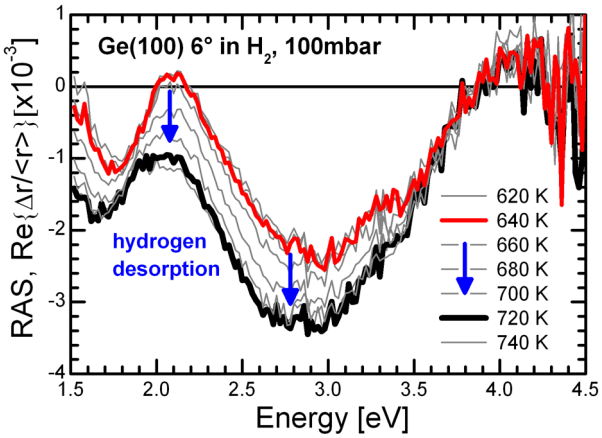

Fig. 44: Continuous in situ RAS measurement of vicinal Ge(100) during heating from 620 K to 740 K at a H_2 pressure of 100 mbar. The red and the black line correspond to the RA spectra of the monohydride and the clean surface, respectively.

In order to study the hydrogen termination of Ge(100) surfaces during standard MOCVD process condition, we conducted continuous in situ RAS measurements during a heating ramp in H_2 process gas. Fig. 44 shows in situ RAS measurements during heating from 620 K to 740 K (100 K/h) at 100 mbar H_2 taken every 20 K. Initially, the sample exhibits the characteristic RAS signal of the monohydride terminated surface (see red line at 620 K). For temperatures higher than 660 K the RAS signal changes (grey lines) until temperatures around 720 K are reached. The spectrum at 720 K agrees well with the RA spectrum of the clean Ge(100) surface, which exhibits a similar line shape but the characteristic RAS features are shifted downwards. The high surface temperature may lead to reduction of the RAS amplitude as well as broadening and shifting of the features in the spectra compared to the room temperature RA spectra in Fig. 41. During further annealing the RAS signal of the clean surfaces stays constant indicating complete hydrogen desorption from the Ge(100) surface. Cooling went along with evolution of the RAS signal related to the monohydride terminated surface again. The RA spectra stayed stable over time at constant temperature indicating equilibrium conditions for the applied process ambient.

The in situ RAS measurements during heating in 100 mbar H_2 process gas ambient (Fig. 44) indicate that the monohydride termination of Ge(100) stays stable for temperatures up to 660 K, while the Ge surface is H-free for $T > 720$ K. Under UHV conditions, H desorbs for $T > 500$ K, accordingly, we observed H desorption under N_2 supply from initially H covered surfaces at temperatures around 520 K as shown above (Fig. 42). For temperatures below 660 K, exposure to H_2 leads to re-establishing of the H-Ge-Ge-H bonds again. In analogy to Si(100), the in situ RAS signals represent the dynamic balance of hydrogen adsorption and desorption events at the Ge(100) surface, which depend on the process parameters such as temperature and hydrogen pressure. Hydrogen desorption prevails over adsorption for temperature above 660 K leading to formation of a clean Ge(100) surface and the corresponding RAS signal.

Knowledge of hydrogen interaction is crucial to understand surface preparation of Ge(100) in MOCVD ambient. In contrast to Si(100) surfaces, we found no indication for influence of H_2 process gas on the step formation at vicinal Ge(100) surfaces. According

to LEED and STM measurements preparation in H_2 ambient leads to formation of single domain surfaces with mainly D_B double-layer steps (Fig. 41), which is in agreement with results obtained under UHV conditions [87] and theory [15]. However, our MOCVD-prepared Ge(100) surfaces exhibit RAS signals with much stronger intensities compared to UHV-prepared samples [36,37], which indicates better surface quality in terms of cleanliness or atomic order.

3.2.3 In situ control of As dimer orientation on Ge(100) surfaces

Having studied the surface preparation of vicinal Ge(100) substrates in H_2 ambient, we now consider the influence of As on the surface structure. Exposure of Ge(100) to As strongly affects the As dimer orientation, the height of steps, and the atomic configuration at the step edges [110–112], which in turn affects the subsequent GaAs nucleation [104–107]. Process temperature, source, and partial pressure of arsenic are key parameters for the Ge(100):As surface preparation [110,111].

Since the atomic surface structure of the Ge(100) substrates is strongly dependent on the preparation route, we employed in situ reflection anisotropy spectroscopy (RAS) for direct characterization of Ge(100):As surfaces during MOCVD processing. Similar to RAS of Si(100) [31,170], the vicinal Ge(100) surface exhibits characteristic RAS signals for both the clean [36,37] and the monohydride terminated surface (see Fig. 41). Ref. [27] demonstrates the sensitivity of RAS to the As dimer orientation on the surface of As terminated Si(100) with 4° offcut.

In this section, we present in situ RA spectra of Ge(100):As_A and Ge(100):As_B surfaces prepared by exposure to TBAs and background As_4, respectively. We applied LEED, STM, and XPS to our Ge(100):As samples to correlate the surface properties with the observed RA spectra. While LEED confirmed mutually perpendicular preferential dimer orientations, STM revealed distinct differences in the step structure, and XPS showed the purity and varying As coverage depending on whether samples were exposed to TBAs or background As_4. The RA spectra of vicinal Ge(100):As surfaces contain contributions

related to both the As dimers and to the step structure. In particular, the sensitivity to the As dimer orientation enables precise in situ control over preparation of single domain Ge(100):As surfaces.

3.2.3.1 RA spectra of vicinal Ge(100):As

Sample preparation took place in a cleaned MOCVD reactor (with regard to III-V residuals to avoid unintentional contamination of the samples) equipped with an in situ RA spectrometer. Ge(100) substrates with 6° misorientation towards [011] direction specified as "epiready" (supplier: AXT) were prepared without any wet-chemical pre-cleaning. The MOCVD preparation was carried out under H_2 process gas at a reactor pressure of 100 mbar for all samples shown here. Annealing at 970 K for 20 min removed oxides and other contamination from the "epiready" substrates (see 3.2.1.1). According to Ref. [111], annealing in AsH_3 at temperatures around 920 K leads to the formation of a and Ge(100):As_B surface whereas annealing in background As_4 results in Ge(100):As_A. In contrast, we used TBAs as As precursor (partial pressure 2.72 x 10^{-2} mbar). Background As_4 was indirectly supplied by the inner MOCVD reactor walls when stopping the TBAs flow.

Fig. 45 shows RA spectra of the Ge(100):As_B (red line) and the Ge(100):As_A surface (green line) measured at 320 K (dimer orientation confirmed by LEED and STM, see below). Preparation of the Ge(100):As_B surface consisted of exposure to TBAs for 10 min at 940 K, cooling to 570 K under TBAs supply and additional annealing at 770 K for 5 min without TBAs supply before cooling to 590 K. In contrast, the Ge(100):As_A sample was annealed for 15 more minutes at 940 K without TBAs supply (after initial TBAs exposure), before cooling to 320 K.

Both in situ RA spectra exhibit similar line shapes but opposite sign. In particular, between 1.5 and 3.1 eV, we observed a sharp local extremum around the critical point energies E_1 and $E_1 + \Delta_1$ at 2.1 eV (blue arrow) and a broad shoulder at around 2.6 eV. As shown for Si(100):As [27], mutually perpendicularly oriented dimers induce an inversion of the RAS signal when step contributions are negligible. The coexistence of dimers with

mutually perpendicular orientation reduces the amplitude of RAS peaks and enables domain quantification by linear scaling [177]. Scaling of the Ge(100):As_B spectrum to the $As_\perp$ spectrum by a factor of -1.38 (dotted red line) matches the intensities of the peak around 2.1 eV, but also reveals explicit differences between both spectra (small gray arrows): the maximum of the Ge(100):As_A spectrum at 2.1 eV is slightly shifted (0.05 eV) towards higher energies compared to the Ge(100):As_B spectrum; above 3.1 eV, the Ge(100):As_B surface exhibits a minor peak around 3.5 eV, whereas the Ge(100):As_A surface features a small shoulder at 3.2 eV and a stronger peak around 3.9 eV with higher intensity.

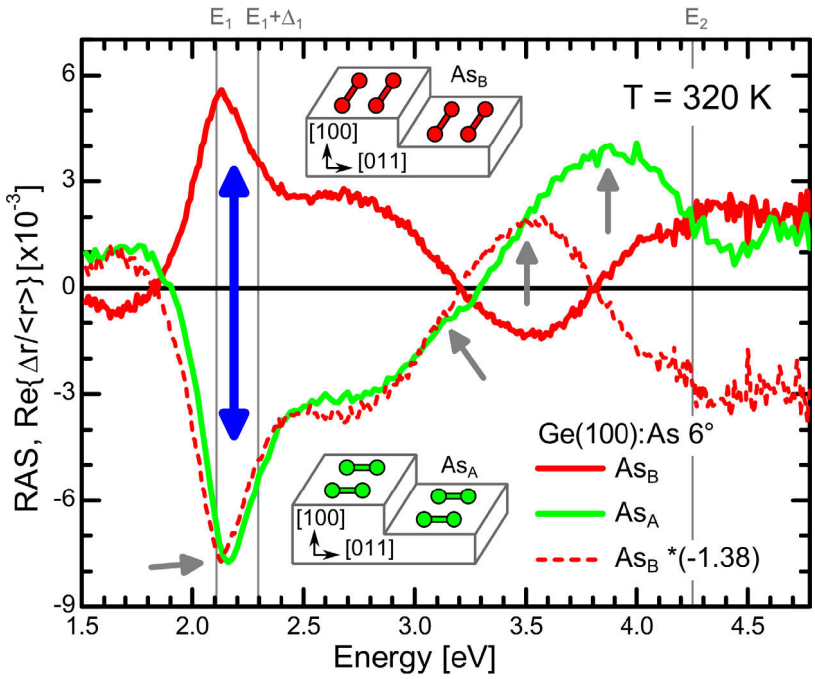

Fig. 45: In situ RAS of Ge(100):As 6° with predominant (2×1) (red) and (1×2) (green) surface reconstruction domains where dimers are oriented parallel (Ge(100):As_B) or perpendicular (Ge(100):As_A) to the step edges, respectively. For comparison, the flipped and scaled (factor 1.38) RA spectrum of Ge(100):As 6° with predominant (2×1) reconstruction is also depicted. The insets illustrate the major As dimer orientation on the surface with respect to the step edges (taken from [185]).

Beyond the type of surface reconstruction, the step structure may also contribute to the RA spectra [24,32]. On vicinal (100) surfaces, step-related RAS contributions depend on the step density [32], and the atomic configuration of the steps [24]. According to Refs.

[110,111], preparation parameters strongly influence the step structure of As exposed Ge(100):As surfaces. We assign the peak structure around 2.1 eV in the RA spectra of both Ge(100):As surfaces to the As dimers and its sign to their orientation (blue arrow), while the significant qualitative differences between the spectra (gray arrows) might be related to different step structures. We measured LEED, STM, and XPS on our Ge(100):As samples to correlate the surface properties with the observed RA spectra.

3.2.3.2 Benchmarking of Ge(100):As RA spectra

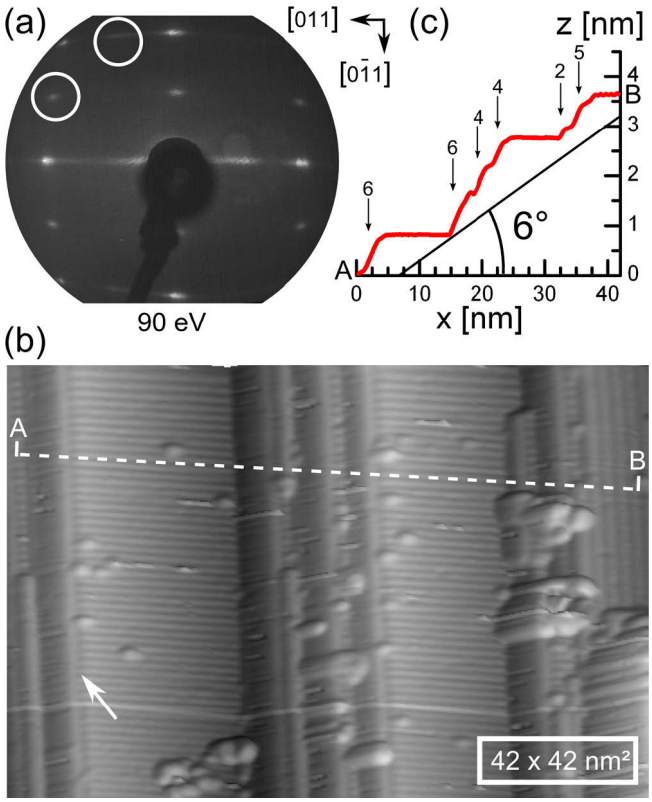

Fig. 46: LEED pattern (a) and STM image (V_{sample} = -3.0 V; I_t = 140 pA, artificially illuminated) (b) of the Ge(100):As_B surface shown in Fig. 45. (c) Presents a profile of the STM image from point A to B (taken from [185]).

Fig. 46 depicts LEED and STM results of the Ge(100):As_B sample. The LEED pattern (Fig. 46 (a)) shows half-order spots with significantly stronger intensity in [0$\bar{1}$1] direction than in [011] direction (see circles) indicating a preference for the (2×1) surface reconstruction domain — equivalent to the majority of As dimers oriented parallel to the

step edges (see upper sketch in Fig. 45). Stripes along [011] direction indicate terraces of irregular width. The STM image of the Ge(100):As_B surface (Fig. 46 (b)) shows dimer rows oriented perpendicular to the step edges, equivalent to parallel alignment of the As dimers. Steps run straight along $[0\bar{1}1]$ direction with a non-uniform step height distribution. Step bunching creates relatively large terraces (see line profile A to B in Fig. 46 (c)) probably driven by etching processes during TBAs annealing [110]. Similar to samples prepared by AsH_3 annealing [110], we observe a small ledge at the end of the dimer rows close to the edge (see arrow in Fig. 46 (b)).

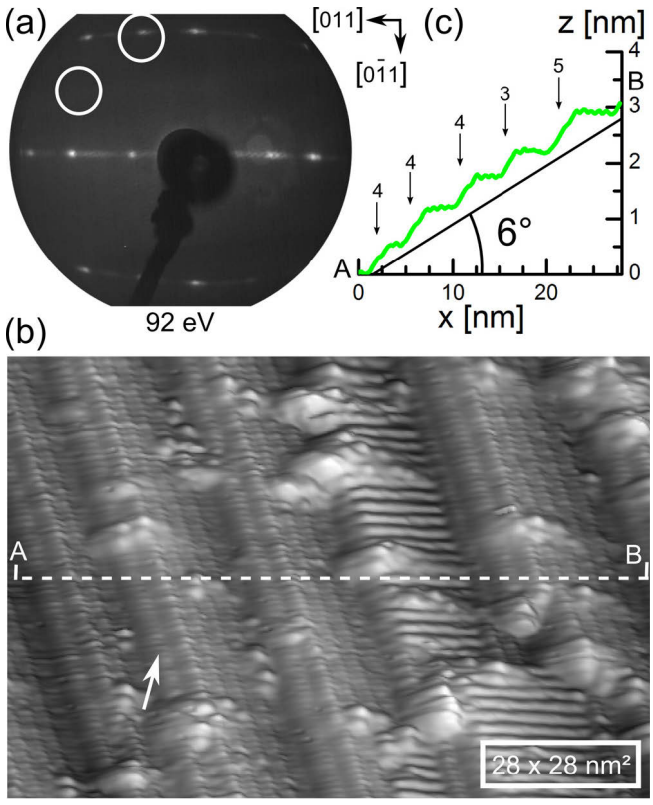

Fig. 47 LEED pattern (a) and STM image (V_{sample} = -0.76 V; I_t = 350 pA, artificially illuminated) (b) of the Ge(100):As_A surface shown in Fig. 45. (c) Presents a profile of the STM image from point A to B.

In contrast to the Ge(100):As_B sample, we recognize a clear preference for the (1×2) reconstruction in the LEED pattern of the Ge(100):As_A sample (Fig. 47 (a)). Half-order spots in [011] direction (see circles) correspond to a surface with As dimers on the

terraces oriented perpendicular to the step edges (see lower inset of Fig. 45). Accordingly, we observed a prevalence of terraces with dimer rows oriented along the step edge in the corresponding STM images (Fig. 47 (b)). Note that Fig. 47 (b) also exhibits few terraces with dimer rows perpendicular to the step edges. The line profile (Fig. 47 (c) shows a more regular sequence of terraces and steps than Fig. 46 (c). Similar to previous background As_4 studies [111] steps run straight along $[0\bar{1}1]$, being mostly four layers high, and of A-type (4A steps). More precise comparison to the step reconstruction proposed by Refs. [110,111] is difficult due to limited STM resolution. On our samples (see arrow in Fig. 47 (b)), the edge of the upper terrace of the 4A steps coincides with the maximum of the outermost dimer row of the terrace. The steps exhibit a small ledge near the centre of the slope to the lower terrace.

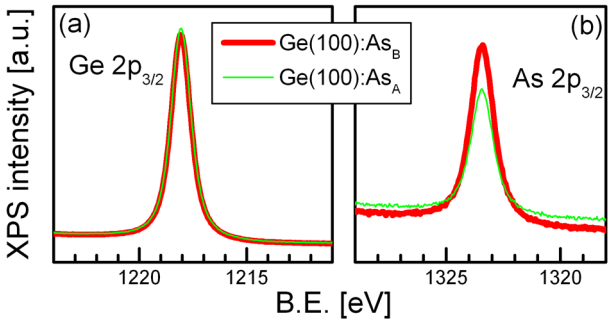

Fig. 48: XP spectra of Ge(100):As_B and Ge(100):As_A in the range of the Ge $2p_{3/2}$ and As $2p_{3/2}$ (taken from [185]).

Both LEED patterns confirm the preparation of nearly single domain Ge(100):As surfaces, but with mutually perpendicular As dimer orientation. Amplitude and sign of the peak structure in the RA spectra between 1.5 and 3.2 eV correspond to the surface reconstruction and reflect the major As dimer orientation in agreement with the LEED results. The LEED patterns suggest the presence of a smaller residual minority domain for the Ge(100):As_A sample, in good agreement with observation of higher RAS intensity around 2.1 eV in the RA spectra (Fig. 45) compared to the data of the Ge(100):As_B surface. The characteristics of the line shape in the RA spectra (grey arrows in Fig. 45) may arise from structural differences on the Ge(100):As surfaces (compare profiles and step edges indicated by arrows in Fig. 46 and Fig. 47 as shown for Si(100)[24,32]. The

occurrence of minority domain terraces on the Ge(100):As_A sample is consistent with mutually perpendicular As dimers but also with selective As desorption exposing the underlying Ge dimers.

We estimated and compared the As concentration on the Ge(100):As_B and Ge(100):As_A samples by XPS employing the surface sensitive Ge $2p_{3/2}$ and As $2p_{3/2}$ photoemission lines. Normalization by matching the intensities of the Ge 3d line, which is a less surface sensitive peak, facilitates a direct comparison of the data (Fig. 48). The Ge $2p_{3/2}$ and As $2p_{3/2}$ line shapes of both samples are equal without an indication for As-Ge bonds in terms of a chemical shift (most probably below our experimental resolution). However, the Ge(100):As_B surface shows a significantly higher intensity in the As $2p_{3/2}$ photoemission line (Fig. 48 (b)). Based on the intensity ratio of the core level intensities (As $2p_{3/2}$ to Ge $2p_{3/2}$) and assuming a simple two-layer model and an electron mean free path of 9 Å for the utilized energy range [196,197], we estimated the As coverages for the different samples: We obtained about 1.0 monolayer (ML) and about 0.7 ML As for the Ge(100):As_B and Ge(100):As_A surface, respectively. Given the surface sensitivity of the XPS, arsenic diffusion into the Ge substrates [198] cannot fully explain the significant differences of the estimation. Arsenic is known to cover Ge(100) by a monolayer forming a chemically passivating surface reconstruction [110], and might desorb from the Ge surface during annealing at 920 K in background As_4 [189]. However, also excess As adsorption might occur during TBAs exposure in direct analogy to excess phosphorus accumulation on GaP(100) surfaces [176]. Considering the high step density on vicinal substrates, the As coverage of the steps edges might have an impact, too. Our STM images show multiple layer steps due to step bunching for Ge(100):As_B, whereas 4A steps prevail on Ge(100):As_A. Since we also identified very different step types (compare step edges at arrows in Fig. 46 (b) and Fig. 47 (b)) on both surfaces, differences in the As coverages appear at least conceivable.

3.2.3.3 As dimer orientation in dependence on process parameters

We applied in situ RAS to directly characterize the influence of process temperature and source of arsenic on the domain formation of vicinal Ge(100):As during preparation in MOCVD ambient. In particular, the amplitude and sign of the RAS feature around 1.9 eV corresponds to the prevalent As dimer orientation on the Ge(100):As surfaces as shown above. Fig. 49 shows continuous RAS measurements during annealing at 940 K in the presence of TBAs and As_4. Exposure of the Ge(100) substrate to TBAs (p_{Part} = 2.72*10^{-2} mbar) at 940 K for 10 min leads to formation of the Ge(100):As_B RAS signal with a positive sign of the peak structure around 1.9 eV and a small negative peak around 3.3 eV (Fig. 49 red line), respectively. After switching off TBAs (gray lines), the positive peak structure decreases and the RAS signal of the Ge(100):As_A surface develops, showing a negative peak with similar structure (green line) and a broad positive feature around 3.6 eV. The spectra (grey lines) show a fast change directly after switching off TBAs within the first 100 s, while afterwards the development slows down. Re-supply of TBAs at 940 K leads to a reversible formation of the former RAS signal (red line, not shown here). When switching on and off TBAs supply during MOCVD preparation, the main source of arsenic present in the reactor changes from TBAs and its pyrolysis products to background As_4 stemming from the arsenic contaminated reactor walls. Accordingly, we directly observe the change from a Ge(100):As_B to a Ge(100):As_A surface at T = 940 K in dependence of the main arsenic source. Both RAS signals remain stable at T = 940 K in TBAs flow or background As_4, respectively.

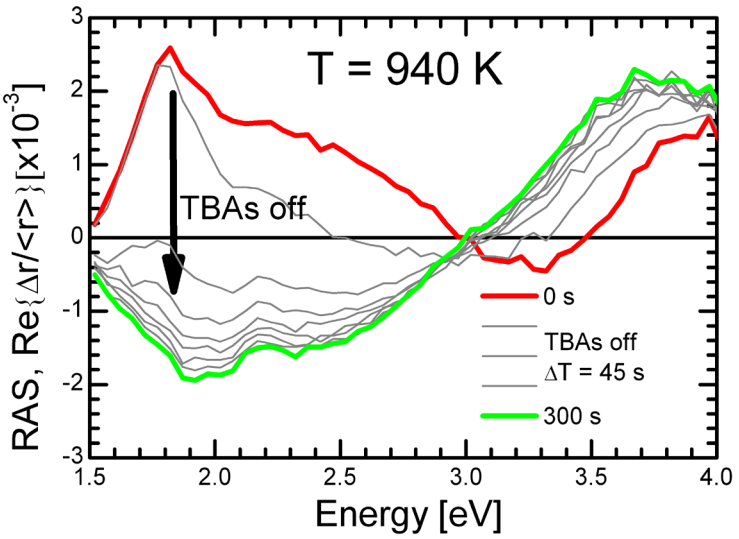

Fig. 49: In situ RA spectra of Ge(100):As with 6° offcut measured every 45 s at 940 K with TBAs on (t = 0 s) and after switching off, showing the transition (grey lines) from Ge(100):As_B (red) to Ge(100):As_A (green).

In order to characterize the temperature-dependent influence of the arsenic source in the reactor on the domain formation we conducted continuous in situ RAS measurements during heating in the presence of TBAs and As_4. Fig. 50 shows in situ RAS measurements in color-coded representation during a heating run from 590 K to 950 K with 100 K/h under TBAs flow (p_{Part} = 2.72*10^{-2} mbar). The RA spectra plotted below refer to the colored horizontal lines in the colorplot at different temperatures. The RAS transient on the right hand side of the color plot corresponds to the black vertical line in the colorplot at 1.9 eV, showing the temperature dependent development of the RAS signal, which is related to the prevalent As dimer orientation on the Ge(100):As surfaces. The heating experiment starts after preparation of a Ge(100):As_A surface as described above. The Ge sample exhibits the corresponding RAS signal as shown for T = 610 K (green line). The transient clearly shows how the negative RAS peak at 1.9 eV steadily decreases during heating until it reaches zero around 820 K. For temperatures between 820 K and 880 K, a RAS signal with a very small broad feature at higher energies is measured (see grey line) and the transient remains at zero. However, the RAS signal of the Ge(100):As_B surface quickly emerges for T > 880 K, according to the slope of the RAS transient, and is fully developed around 940 K (see red line).

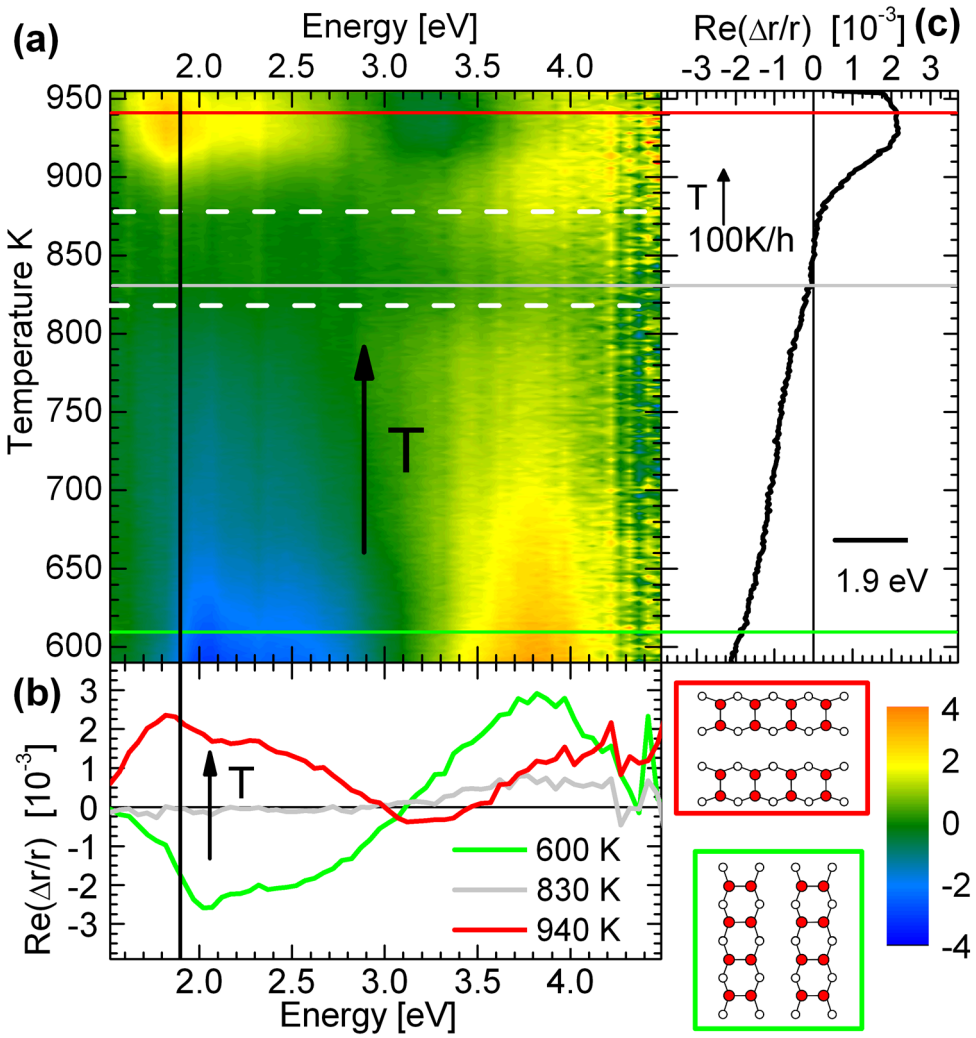

Fig. 50: Continuous in situ RAS measurements in color-coded representation (52 s/RAS) during a heating run from 590 K to 950 K in the presence of TBAs (p_{Part} = 2.72*10^{-2} mbar) starting with a Ge(100):As_B surface. The RA spectra below correspond to the colored horizontal lines at different temperatures, while the RAS transient on the right corresponds to the vertical black line at 1.9 eV showing the temperature-dependent development of the domain-sensitive RAS peak of Ge(100):As.

From the RAS measurements above, we conclude that the Ge(100):As_A surface is unstable during exposure to TBAs. The reduced amplitude of RA spectrum at 610 K indicates that TBAs already influences the Ge surface at low temperatures. The Ge(100):As_A surface degrades slowly with increasing temperature and a two domain surface is formed for temperatures between 820 K and 880 K (area between white dotted lines Fig. 51). Temperatures higher than 880 K are required to induce a Ge(100):As_B

surface in the presence of TBAs. Of course, variation of the TBAs partial pressure may significantly change the observed time and temperature dependence of the domain formation.

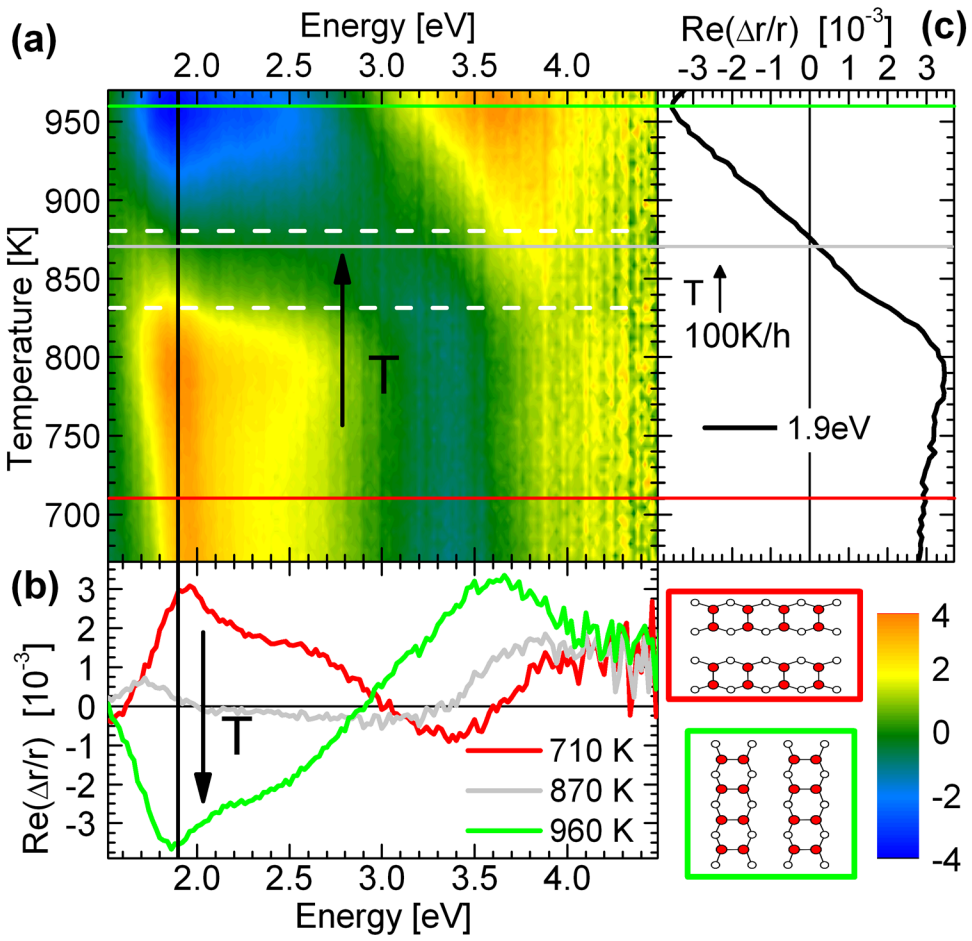

Fig. 51: Continuous in situ RAS measurements in color-coded representation (145 s/RAS) during a heating run from 670 K to 970 K in the presence of As_4 ($p_{part} = 2.72 \times 10^{-2}$ mbar) starting with a Ge(100):As_A surface. The RA spectra below correspond to the colored vertical lines at different temperatures, while the RAS transient on the right corresponds to the vertical black line at 1.9 eV showing the temperature dependent development of the domain sensitive RAS peak of Ge(100):As.

Fig. 51 shows continuous RAS measurements during a heating ramp from 670 K to 970 K in the presence of As_4. The colorplot starts after preparation of a Ge(100):As_B surface by exposure of the Ge sample to TBAs at 940 K and cooling to 670 K, where TBAs was switched off. At the beginning, the surface exhibits the characteristic Ge(100):As_B RAS signal with a positive RAS peak around 1.9 eV (see red line). The corresponding RAS

transient at 1.9 eV (vertical black line) therefore starts with a positive value, respectively, which increases slightly during heating up to temperatures around 800 K. For temperatures higher than 800 K, the Ge(100):As_B RAS signal decreases quickly during further heating, and we observe a transition to the Ge(100):As_A RAS signal which is completely evolved around 950 K. In the temperature range where the value of the transient RAS signal at 1.9 eV is around zero, we observe a RA spectrum with a distinct broad feature around 3.8 eV (grey line), which is much more pronounced than the RAS signal observed during the heating run in TBAs in the transition range.

During annealing in As_4, the Ge(100):As_B surface stays stable until temperatures around 800 K according to the development in the RAS measurements. We even observe an increasing RAS amplitude around 1.9 eV which indicates increasing atomic order on the surface probably due to desorption of residual TBAs precursor fragment or better ordering of the As dimers. While the in situ RAS measurements indicate a temperature range during the transition from the Ge(100):As_A to the Ge(100):As_B surface under TBAs flow which induces a two-domain surface (area indicated by dotted white lines in Fig. 51), we observe a continuous transition from the Ge(100):As_B to the Ge(100):As_A surface during heating in As_4. In particular, the samples exhibit different RAS signals in the transition range (compare grey lines). Temperatures above 920 K are necessary to prepare a prevalent Ge(100):As_A surface.

The in situ RAS experiments show significant differences in the influence of TBAs and As_4 on the domain structure of Ge(100) during heating. During annealing in TBAs only the formation of Ge(100):As_B surface is preferred which requires temperatures above 880 K. However, the Ge(100):As_A surface evolves when switching off TBAs supply in the same temperature range. Accordingly, the Ge(100):As surface preparation exhibits a highly sensitive domain formation under different reactor conditions. Similar to the observations on the Si(100) surface in H_2 ambient, surface energetics as well as kinetics compete during step and domain formation induced by temperature and the interaction between the AsH_3 or As_4 and the Ge(100) surface. The in situ RAS measurements enable direct characterization of the different processes of the Ge(100) surface in dependence on the relevant process parameters. However, further RAS measurements under different

reactor conditions and from different starting points as well as detailed analysis of the surface structure at characteristic points in the preparation are required for a complete understanding. In particular, analysis of the transition between sample surfaces with mutually perpendicular majority domains might give an insight in the step formation processes.

3.2.4 Influence of TBP on the Ge(100) surface structure

Growth of a high quality III–V nucleation layers usually begins with exposure of Ge(100) substrates to group V precursors after high temperature annealing for oxide removal [46,105,110,199]. Particularly, P termination of the Ge(100) surface should be obtained prior to nucleation for state-of-the-art GaInP on Ge(100) heteroepitaxy in MOCVD environment [108,109]. Only little is known about the P terminated Ge(100) surface prepared in a process gas ambient [108,118]. In this section, we studied the vicinal Ge(100) surface after exposure to TBP in MOCVD ambient. While XPS and LEED revealed the surface termination and reconstruction, respectively, RAS was used for in situ characterization of TBP annealed Ge(100) surfaces during MOCVD preparation. Correlation of the RA spectrum of the TBP annealed Ge(100) surface to results from XPS and LEED indicated a characteristic RAS signal for the P-terminated vicinal Ge(100) surface.

3.2.4.1 In situ RAS signal of TBP annealed vicinal Ge(100)

After preparation of a clean Ge(100) surface according to the process described in section 2.4.7.2, the samples were annealed under a TBP flow of 1.03×10^{-4} mol/min at 920 K and a reactor pressure of 100 mbar for 5 min. Subsequently, the samples were cooled down to 570 K, at which point the TBP flow was switched off.

Fig. 52 shows the characteristic RAS signal of the TBP annealed (thick black line) vicinal Ge(100) surface measured at RT in comparison to the RAS signals of the monohydride terminated (thin red line), and the clean Ge(100) surface (broken gray line). Exposure to TBP as described above resulted in a characteristic RA spectrum (Fig. 52, black line) which consists of a broad negative minimum at 2.3 eV (matching the Ge(100) E_1+Δ_1 critical point), a broad positive maximum at 3.7 eV and a shoulder at 1.9 eV.

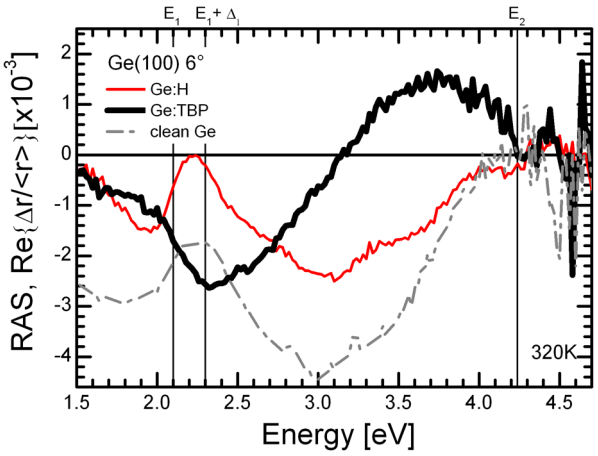

Fig. 52: In situ RA spectra of monohydride terminated (thin red line), clean (broken gray line) and TBP annealed (thick black line) Ge(100) with 6° offcut in [011] measured at 320 K in H_2 ambient. Vertical lines indicate the critical points energies of Ge(100) (taken from [186]).

3.2.4.2 Chemical composition and surface reconstruction

We carried out XPS and LEED measurements to explore the chemical configuration and the reconstruction of the surface after annealing in TBP. Fig. 53 (c)–(e) shows XP spectra in the range of the Ge $2p_{3/2}$, P 2p and C 1s photoemission lines of the Ge(100) substrate after exposure to TBP (black line) and annealing in H_2 (red line) for comparison. The influence of band bending was corrected in the XPS data by matching the energetic positions of the elemental Ge photoemission (PE) signals between the samples [147]. For easier viewing, we added an offset to separate both XP spectra. After H_2 annealing, the XPS measurements show neither contributions related to C (Fig. 53 (e)) nor oxygen or oxides (Fig. 53 (c)), see section 3.2.1.1 for further details. After annealing under TBP, a shoulder at 129 eV, which matches to the P 2p line, indicates the presence of P on the

surface (Fig. 53 (d)). The deconvolution of the P 2p XP spectra (Fig. 53 (d)) enabled the determination of the intensities related to the P 2p, Ge $3p_{1/2}$ and Ge $3p_{3/2}$ PE line. A small peak at 285 eV in the range of the C 1s line indicated the presence of C on the surface (Fig. 53 (e), black line). Since C was absent after H_2 annealing [183], the C contamination probably originates from a by-product of the pyrolysis of the metalorganic source. Neither traces of As, Ga nor other elements typically present in a MOCVD reactor were detected in the XP spectra after TBP annealing.

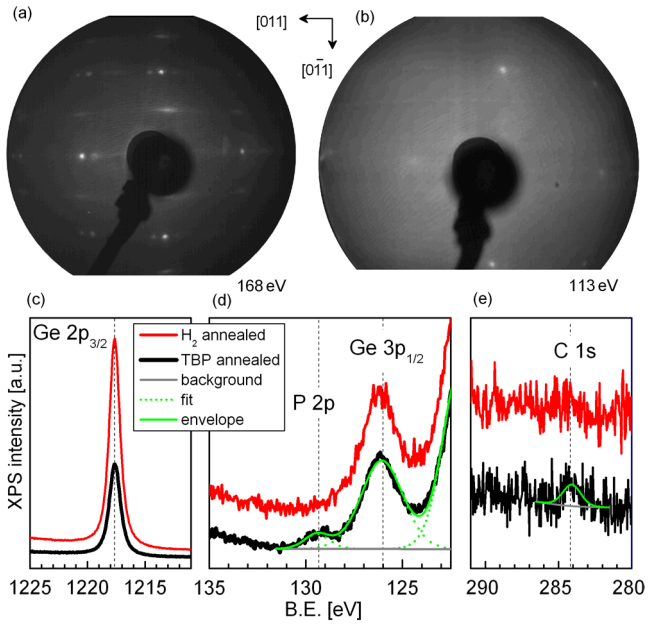

Fig. 53: LEED patterns of the Ge(100) surface after H_2 (a) and TBP annealing (b) as well as corresponding XPS measurements in the range of the Ge $2p_{3/2}$ (c), P 2p (d) and C 1s (e) PE line (taken from [186]).

The peak intensity of the Ge $2p_{3/2}$ peak is significantly reduced after the annealing procedure in TBP compared to the H_2 annealed surface (Fig. 53 (c)) due to coverage of the surface by P and C. From the attenuation of the signal intensity of the TBP annealed sample, we roughly estimated the thickness of the coverage by applying a simple two-layer model. If we assume intensity absorption in the upper layer according to the Beer–Lambert law and consider an electron mean free path of 9 Å in that energy range [196,197], we can estimate a layer thickness of about 3.3 Å containing P and C. From the intensity ratio P 2p/Ge 3p we estimated a coverage of the TBP annealed Ge surface of

about 2.1 Å equivalent to 1.5 monolayer (ML) of P using the same model and assumptions as above and an electron mean free path of 29 Å according to the different energy range [196,197]. Regarding C, it is difficult to quantify its amount on the surface due to the low and noisy C 1s signal measured. According to Shimamune [118], P termination prepared in UHV is self-limited to 1 ML. However, dissociation of TBP as well as adsorption and desorption of P can include certain quantities of excess P atoms [200].

The LEED pattern of the monohydride Ge(100) surface (Fig. 53 (a)) shows half-order spots along the $[0\bar{1}1]$ direction and spot splitting along the [011] direction, which indicates a predominant (2×1) surface reconstruction with D_B steps and terraces of equal width, respectively (see Fig. 41). After TBP annealing, the Ge surface (Fig. 53 (b)) exhibits a (1×1) LEED pattern with a high background, which indicates a disordered surface. In contrast, Ref. [108] reports on a (9×2) surface reconstruction for a Ge(100) substrate with 2° offcut. Since our XPS analysis confirms the presence of C and more than one ML of P on the Ge surface, we assume that the high background in the LEED pattern is related to the presence of excess P and TBP by-products on the surface. Surface disorder caused by excess of P and TBP by-products has been reported for the MOCVD prepared P-rich GaP(100) surface [176].

Despite the observation of a disordered surface according to the LEED pattern, we do obtain a characteristic RA signal when annealing under TBP, which indicates ordered anisotropic structures on the Ge surface, at least to some degree. In general, differences in the atomic order of probed (100) surfaces - such as cleanliness, surface reconstruction and chemical configuration - affect shape and amplitude of the RA spectra [25]. Considering that (i) P induces changes in the surface reconstruction [108]; (ii) the thickness estimation for the P coverage from XPS measurements corresponds to more than 1 ML of P; and (iii) carbon [36] as well as TBP fragments [176] mainly reduce the observed RAS signal intensity, it seems very likely that the RA spectrum of Fig. 52 might arise from the surface reconstruction of the P terminated Ge(100) surface underneath a layer of TBP fragments.

3.2.4.3 In situ observation of P desorption from Ge(100)

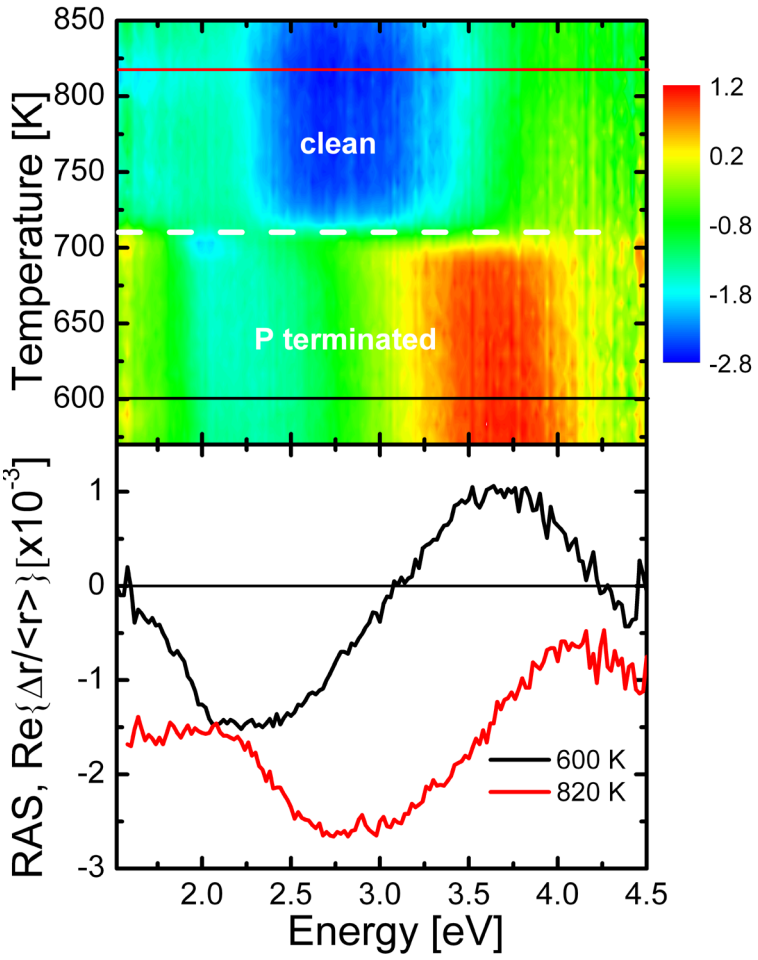

Fig. 54: Colorplot of a continuous in situ RAS measurement (upper panel) at a Ge(100) surface during heating from 570 to 850 K at a rate of 3.4 K/min without TBP supply. The color coded scale represents the intensity of the RA signal. The lower panel shows the RA spectra corresponding to the dotted lines. The RAS signal at 600 K (black) corresponds to the P-terminated Ge(100) surface and the RAS signal at 820 K (red) to the clean Ge(100) surface (taken from [186]).

A phosphorous desorption experiment was carried out to check for the origin of the RAS signal. After preparation of a P-terminated surface by TBP exposure as described above, the temperature was raised from 570 K to 850 K at a rate of 3.4 K/min at a H_2 pressure of 100 mbar without TBP supply, while RA spectra were measured continuously. The continuous RAS measurements are depicted as colorplot in Fig. 54 (upper panel). A clear change in the RAS signal is visible during the heating ramp around 700 K. Representative

initial and final spectra (Fig. 54 (lower panel)) of the observed evolution in the colorplot correspond to the P terminated and the clean Ge(100) surfaces, respectively. Their characteristic features agree very well with the RT spectra in Fig. 52 considering a thermal shift of the features towards lower energies [178]. The RAS signal of the P-terminated Ge(100) surface is stable in the temperature range of 570 – 695 K, for higher temperatures the RAS signal of the clean Ge surface evolves which is completely developed at 730 K. An XPS analysis of the resulting surface after the temperature ramp (not shown here) confirms no traces of P, but C is still present. If TBP is introduced again in the reactor, the RA spectrum associated with P termination re-emerges. Consequently, we observe the transition from a P-terminated to a clean Ge surface by RAS in Fig. 53. The Ge–P bonds cannot be re-established once they are broken at high temperatures in H_2 ambient. This transition also indicates that the RA spectrum of the TBP annealed sample is mainly surface related. Furthermore, the color-coded RAS measurement shows that P desorption from the Ge(100) surface begins at 695 K and desorption is complete at 730 K. This temperature range is in good agreement with the results from Shimamune et al. [118] for low pressure CVD systems.

3.3 Key aspects of Si(100) and Ge(100) surface preparation

In this section, we compare the key results from our surface study of MOCVD-prepared Si(100) and Ge(100) surfaces.

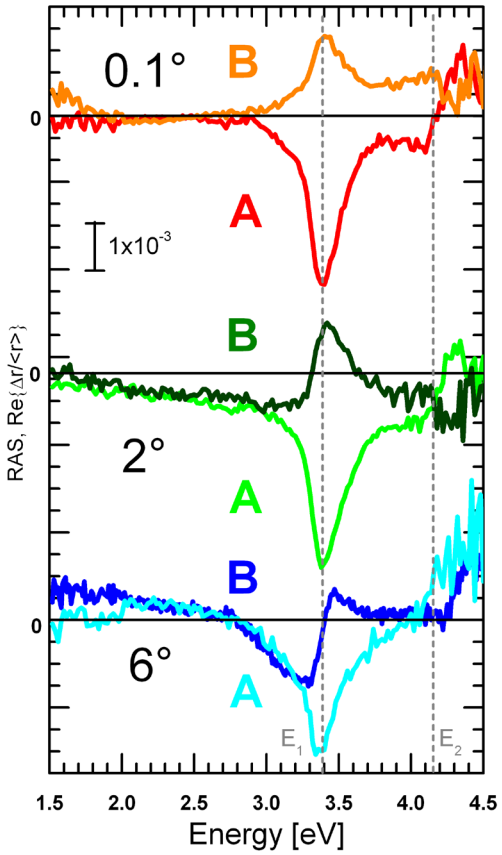

Fig. 55: In situ RA spectra of monohydride terminated Si(100) surfaces with 0.1°, 2°, and 6° offcut in [011] direction and prevalence for the A- or B-type domain, respectively. All A-type surface and the b-type surfaces of 0.1° and 2° samples exhibit a RAS signal with a characteristic peak at 3.4 eV which reflects the major dimer orientation by amplitude and sign. The "derivative"-like line shape of RAS signal of the B-type 6° sample might be related to D_B double-layer steps on the surface.

Both surfaces exhibit characteristic RAS signals which enable in situ monitoring of crucial processes during preparation in MOCVD environment. Fig. 55 and Fig. 56 summarizes the RAS signals of the monohydride terminated Si(100) surfaces as well as the signals of the different vicinal Ge(100) surfaces, we discussed above. On both

surfaces, RAS measures characteristic signals for the clean and the monohydride terminated surface, respectively, which enabled us to study hydrogen interactions on the different surfaces (see 3.1.1 and 3.2.2). The sensitivity of RAS to the dimer orientation on monohydride terminated Si(100) surfaces (see 3.1.2, 3.1.3, 3.1.4) and the vicinal Ge(100):As surface (see 3.2.3), respectively, enabled in situ quantification and control of the present domain distribution on the surfaces which is reflected by amplitude and sign of the RAS signals.

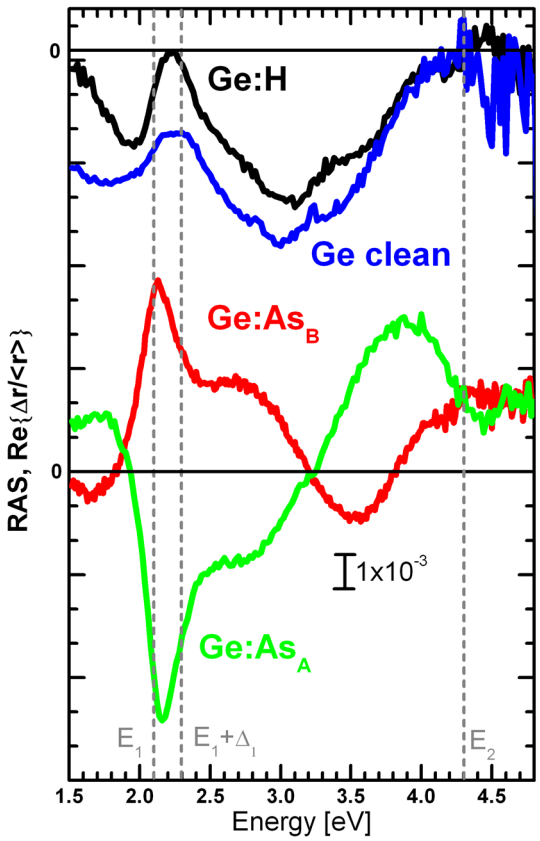

Fig. 56: In situ RA spectra of vicinal Ge(100) clean, monohydride terminated and As terminated. Structural differences of the steps on the Ge(100):As$_B$ and Ge(100):As$_A$ lead to differences in the RAS signal.

Thermal annealing in H_2 ambient reliably removes oxides and other contamination from Si(100) and Ge(100) surfaces. After deoxidation, processing in H_2 process gas ambient induces strong interaction of the substrate surface with hydrogen. There is a permanent

interplay of H_2 adsorption and desorption. Hence, the present hydrogen coverage is a result of the temperature-dependent adsorption and desorption rate. Cooling in H_2 leads to formation of a stable monohydride termination on both surfaces while the surfaces are hydrogen free in H_2 ambient at higher temperatures, respectively. The Ge(100) surface is hydrogen free at process conditions typically used for III-V nucleation (690 – 1000 K, 50 – 100 mbar H_2 pressure) [109,177,201–203], whereas Si(100) surfaces remain effectively monohydride covered in this temperature range.

For temperatures above T > 970 K hydrogen desorption starts to prevail over adsorption on Si(100). The critical temperature range from 970 K to 1120 K is decisive for the step and domain formation due to the strong interaction between hydrogen and Si substrate. Preparation under high H_2 pressure induces Si removal and vacancy generation on the terraces. On large terraced substrates, vacancy diffusion leads to formation of elongated vacancy islands and layer-by-layer removal. On vicinal substrates vacancy diffusion and annihilation preferentially at the B-type step edges, cause a retreat of this step edge and hence the formation of an A-type majority domain and D_A double layer steps. However, preparation under low H_2 pressures reduces the interaction between process gas and Si surface, leading to formation of a B-type majority domain and D_B steps on vicinal substrates, which is expected to be the energetically favored surface configuration.

In contrast, we found no indication for similar removal processes or influences on the step structure during processing of Ge(100) surfaces in H_2 ambient. Accordingly, the vicinal Ge(100) surfaces exhibit a prevalence for the B-type domain and D_B double layer steps.

Exposure to group-V precursors, which is important with regard to subsequent III-V nucleation, strongly affects the domain and step structure of the Ge(100) surface [110–112]. Similar to our observations on Si(100) in H_2 ambient, we were able to monitor and control the domain formation on Ge(100):As surfaces in dependence of arsenic source and temperature by in situ RAS. Our surface study during As annealing revealed highly reactive surface conditions for the vicinal Ge(100) surface. We were able to prepare Ge:As surfaces with mutually perpendicular major dimer orientations, a Ge(100):As_B by annealing in TBAs (AsH_3) and a Ge(100):As_A surface by annealing in background As_4,

respectively. However, exposure to As also affects the step height on vicinal Ge(100) substrates. The etching conditions under AsH_3 lead to formation of multiple layer steps due to step bunching, whereas 4A steps prevail after annealing in background As_4. On Si(100), we observed mainly formation of single- and double-layer steps after etching in H_2 ambient. Ge(100):P surfaces prepared with TBP exhibit a rather disordered surface compared to the Ge(100):As surfaces. In contrast to TBAs, annealing under TBP supply resulted in a disordered P terminated surface with carbon contamination. Accordingly, the As terminated surfaces exhibit better properties regarding subsequent III-V nucleation and heteroepitaxy.

4. Conclusion

In this work, we studied the atomic structure of Si(100) and Ge(100) surfaces in MOCVD ambient by various surface sensitive methods. Our results differ significantly from UHV-based studies and theory, since energetically and kinetically driven processes compete during MOCVD preparation. We applied in situ RAS to monitor and investigate these processes on the Si and Ge(100) surfaces in a process gas ambient of a MOCVD reactor We established RA spectra of different Si(100) and Ge(100) surfaces by benchmarking the RAS signals of our samples to results from other UHV-based surface-sensitive methods. In particular, we verified the sensitivity of RAS to the dimer orientation on monohydride terminated Si(100) and As-terminated vicinal Ge(100) surfaces. On both the Si(100):H 6° and the Ge(100):As 6° surfaces, we observed contributions to the RAS signal from the terraces as well as the steps. Therfore, RAS provided in situ observation and control of domain formation in MOCVD ambient. Processing in H_2 and N_2 ambient allowed us to identify the RAS signal of clean and monohydride terminated vicinal Ge(100). The sensitivity to the hydrogen termination enabled detailed studies of hydrogen desorption kinetics on the Ge(100) surface which agreed with other UHV-based studies.

From in situ RAS results and UHV-based surface sensitive methods, we identified the crucial preparation parameters and concluded on the step and domain formation processes. Our findings indicate a substantial interaction between the hydrogen ambient and the Si(100) surface determined by the temperature dependent equilibrium of adsorption and desorption rates. The Si(100) surface is hydrogen-free at high temperatures during processing in H_2 ambient while cooling leads to monohydride termination on the surface. The temperature range between 970 K and 1120 K, where H desorption starts to prevail over H adsorption, is crucial for the step and domain formation. In this critical temperature range, Si atom removal occurs during annealing in H_2 ambient at high pressure. Vacancy generation and anisotropic vacancy diffusion preferentially parallel to the direction of the dimer rows influence the resulting step structure. On large terraced/low-offcut Si(100) substrates vacancies merge into elongated islands resulting in Si atom removal in a layer-by-layer fashion. On vicinal surfaces, the

vacancy diffusion length is large compared to the terrace width. Vacancies preferentially annihilate at the B-type step edges, which results in a retreat of the B-type terraces and a formation of an A-type majority domain and D_A double layer steps. Monohydride passivation of the Si(100) surfaces during cooling stabilizes the energetically unfavorable step configuration. Preparation in low H_2 pressure ambient reduces the interaction between H_2 and Si(100). Accordingly, we observed the formation of an energetically favorable step structure which corresponds to a B-type majority domain on vicinal Si(100) substrates and mainly D_B steps for high offcuts. Low pressures as well as fast cooling below the critical temperature range reduce the influence of Si removal on the surface structure. According to in situ RAS measurement of the Si etch rate k in dependence on temperature, we determined an activation energy of $E_d = 2.75 \pm 0.20$ eV for Si etching from nearly exact Si(100) surfaces in 950 mbar H_2 ambient

Regarding the Ge(100) preparation, we confirmed complete removal of oxygen and other contaminations from oxidized “epiready” wafers. Analogous to Si(100), Ge(100) surfaces are monohydride terminated after processing in H_2 ambient. The hydrogen coverage of the Ge surface during processing in H_2 ambient represents a dynamic balance of hydrogen adsorption and desorption events depending on the process parameters such as temperature and hydrogen pressure. Accordingly, Ge(100) is H-free in H_2 process gas ambient at a H_2 pressure of 100 mbar for temperatures above 640 K. In contrast to Si(100), we observed no indication for etching processes induced by the H_2 interaction. The vicinal Ge(100) substrates exhibited a clear (2×1)/B-type majority domain and mainly D_B double layer steps, respectively. These findings served as a starting point to study the influence of As and P on the surface structure of vicinal Ge(100) substrates. Annealing in TBAs at 940 K resulted in a Ge(100):As surface with prevalence for As dimers oriented parallel to the step edges (Ge(100):As_B), while annealing at the same temperature in the presence of background As_4 led to a surface with As dimers oriented perpendicular to the step edges (Ge(100):As_A). STM measurements revealed distinct differences in the step structure of Ge(100):As_B and Ge(100):As_A surfaces, in particular, formation of multiple layer steps due to step bunching after annealing in TBAs, and mainly 4A quadruple-layer steps after annealing in background As_4, respectively. In situ

RAS provided access to study the highly reactive Ge(100) surface preparation under As exposure and allowed us to control the domain formation depending on the type of As in the reactor and temperature. In contrast to As exposure, TBP annealing resulted in a rather disordered P-terminated surface covered by about 1.5 ML of P and carbon contamination. We attributed the presence of carbon to a byproduct of the TBP pyrolysis, since the Ge(100) surfaces were carbon free after H_2 annealing. The P termination is less stable than the As termination, since we observed P desorption already for temperatures around 700 K by in situ RAS studies.

The established RAS signals enable further detailed studies of processes in MOCVD ambient such as H adsorption and desorption, Ge(100):As step formation, as well as Si and Ge deoxidation.

Knowledge on the formation and stability of the substrate surface structure is crucial for the subsequent III-V nucleation. Pressure and temperature variations may significantly change the domain formation. In case of single layer step formation, anti-phase disorder will be induced in the subsequently grown III-V film. As a next step, we have to investigate the influence of the different surface preparation routes on the subsequent III-V nucleation and the device quality. Here, in situ RAS can be used to control the crucial interface formation [173]. Since the present study explored the surface preparation only in a clean and an As-terminated MOCVD reactor, investigation of the influence of other III-V residual (In, Ga, As) in the reactor from previous runs is necessary. Advances in the Ge(100) surface preparation can be tested by established III-V test structures (InGaAs, InGaP double hetero structures or tandem solar cells). However, preparation of photovoltaic structures on Si(100) requires extensive research regarding the lattice-matched material of dilute nitrides or development of graded buffer structures. Furthermore, we plan to transfer the knowledge and experience of III-V on IV(100) heteroeptitaxy to the MOCVD preparation of Si(111) substrates for III-V nanowire growth, enabling 3rd generation photovoltaic structures.

Bibliography

[1] International Energy Agency (IEA), "Key World Energy Statistics 2012," 2012, <http://www.iea.org/publications/freepublications/publication/name,31287,en.html> (24 April 2013).

[2] Bruno Burger, "Electricity production from solar and wind in Germany in 2012," 2013, <http://www.ise.fraunhofer.de/en/downloads-englisch/pdf-files-englisch/news/electricity-production-from-solar-and-wind-in-germany-in-2012.pdf> (2 April 2013).

[3] W. Shockley and H. J. Queisser, "Detailed Balance Limit of Efficiency of p-n Junction Solar Cells," *J. Appl. Phys.* **32**(3), 510–519 (1961) [doi:10.1063/1.1736034].

[4] J. M. Olson, S. R. Kurtz, A. E. Kibbler, and P. Faine, "A 27.3% efficient $Ga_{0.5}In_{0.5}P$/GaAs tandem solar cell," *Appl. Phys. Lett.* **56**(7), 623–625 (1990) [doi:10.1063/1.102717].

[5] G. B. Stringfellow, *Organometallic Vapor-Phase Epitaxy, Second Edition: Theory and Practice*, 2nd ed., Academic Press (1998).

[6] A. Luque, "Will we exceed 50% efficiency in photovoltaics?," *J. Appl. Phys.* **110**(3), 031301–031301–19 (2011) [doi:10.1063/1.3600702].

[7] J. F. Geisz, J. M. Olson, D. J. Friedman, K. M. Jones, R. C. Reedy, and M. J. Romero, "Lattice-matched GaNPAs-on-silicon tandem solar cells," in *Conf. Rec. Thirty-First IEEE Photovolt. Spec. Conf. 2005*, pp. 695–698 (2005) [doi:10.1109/PVSC.2005.1488226].

[8] S. Liebich, M. Zimprich, A. Beyer, C. Lange, D. J. Franzbach, S. Chatterjee, N. Hossain, S. J. Sweeney, K. Volz, et al., "Laser operation of Ga(NAsP) lattice-matched to (001) silicon substrate," *Appl. Phys. Lett.* **99**(7), 071109–071109–3 (2011) [doi:10.1063/1.3624927].

[9] H. Kroemer, "Polar-on-nonpolar epitaxy," *J. Cryst. Growth* **81**(1-4), 193–204 (1987) [doi:10.1016/0022-0248(87)90391-5].

[10] S. F. Fang, K. Adomi, S. Iyer, H. Morkoc, H. Zabel, C. Choi, and N. Otsuka, "Gallium arsenide and other compound semiconductors on silicon," *J. Appl. Phys.* **68**(7), R31–R58 (1990) [doi:10.1063/1.346284].

[11] H. Döscher, A. Dobrich, S. Brückner, P. Kleinschmidt, and T. Hannappel, "Si(100) surfaces in a hydrogen-based process ambient," *Appl. Phys. Lett.* **97**(15), 151905 (2010) [doi:10.1063/1.3497992].

[12] B. Kunert, I. Németh, S. Reinhard, K. Volz, and W. Stolz, "Si (001) surface preparation for the antiphase domain free heteroepitaxial growth of GaP on Si substrate," *Thin Solid Films* **517**(1), 140–143 (2008) [doi:10.1016/j.tsf.2008.08.077].

[13] A. Dobrich, P. Kleinschmidt, H. Döscher, and T. Hannappel, "Quantitative investigation of hydrogen bonds on Si(100) surfaces prepared by vapor phase epitaxy," *J. Vac. Sci. Technol. B Microelectron. Nanometer Struct.* **29**, 04D114 (2011) [doi:10.1116/1.3609253].

[14] A. Beyer, J. Ohlmann, S. Liebich, H. Heim, G. Witte, W. Stolz, and K. Volz, "GaP heteroepitaxy on Si(001): Correlation of Si-surface structure, GaP growth conditions, and Si-III/V interface structure," *J. Appl. Phys.* **111**(8), 083534–083534–6 (2012) [doi:10.1063/1.4706573].

[15] D. J. Chadi, "Stabilities of single-layer and bilayer steps on Si(001) surfaces," *Phys. Rev. Lett.* **59**(15), 1691 (1987) [doi:10.1103/PhysRevLett.59.1691].

[16] B. S. Swartzentruber, Y.-W. Mo, M. B. Webb, and M. G. Lagally, "Scanning tunneling microscopy studies of structural disorder and steps on Si surfaces," *J. Vac. Sci. Technol. Vac. Surf. Films* **7**(4), 2901–2905 (1989) [doi:10.1116/1.576167].

[17] A. R. Laracuente and L. J. Whitman, "Step structure and surface morphology of hydrogen-terminated silicon: (0 0 1) to (1 1 4)," *Surf. Sci.* **545**(1-2), 70–84 (2003) [doi:10.1016/j.susc.2003.08.038].

[18] S. Jeong and A. Oshiyama, "Structural Stability and Adatom Diffusion at Steps on Hydrogenated Si(100) Surfaces," *Phys. Rev. Lett.* **81**(24), 5366 (1998) [doi:10.1103/PhysRevLett.81.5366].

[19] F. A. Reboredo, S. B. Zhang, and A. Zunger, "Hydrogen-induced instability on the flat Si(001) surface via steric repulsion," *Phys. Rev. B* **63**(12), 125316 (2001) [doi:10.1103/PhysRevB.63.125316].

[20] J.-T. Zettler, "Characterization of epitaxial semiconductor growth by reflectance anisotropy spectroscopy and ellipsometry," *Prog. Cryst. Growth Charact. Mater.* **35**(1), 27–98 (1997) [doi:10.1016/S0960-8974(97)00024-7].

[21] P. Weightman, D. S. Martin, R. J. Cole, and T. Farrell, "Reflection anisotropy spectroscopy," *Rep. Prog. Phys.* **68**(6), 1251–1341 (2005) [doi:10.1088/0034-4885/68/6/R01].

[22] P. H. Hahn, W. G. Schmidt, F. Bechstedt, O. Pulci, and R. Del Sole, "P-rich GaP(001)(2 x 1)/(2 x 2) surface: A hydrogen-adsorbate structure determined from

first-principles calculations," *Phys. Rev. B* **68**(3), 033311 (2003) [doi:10.1103/PhysRevB.68.033311].

[23] W. G. Schmidt, P. H. Hahn, F. Bechstedt, N. Esser, P. Vogt, A. Wange, and W. Richter, "InP(001)-(2 x 1) Surface: A Hydrogen Stabilized Structure," *Phys. Rev. Lett.* **90**(12), 126101 (2003) [doi:10.1103/PhysRevLett.90.126101].

[24] W. G. Schmidt, F. Bechstedt, and J. Bernholc, "Terrace and step contributions to the optical anisotropy of Si(001) surfaces," *Phys. Rev. B* **63**(4), 045322 (2001) [doi:10.1103/PhysRevB.63.045322].

[25] N. Witkowski, R. Coustel, O. Pluchery, and Y. Borensztein, "RAS: An efficient probe to characterize Si(0 0 1)-(2 × 1) surfaces," *Surf. Sci.* **600**(24), 5142–5149 (2006) [doi:10.1016/j.susc.2006.08.045].

[26] O. Supplie, T. Hannappel, M. Pristovsek, and H. Döscher, "In situ access to the dielectric anisotropy of buried III-V/Si(100) heterointerfaces," *Phys. Rev. B* **86**(3), 035308 (2012) [doi:10.1103/PhysRevB.86.035308].

[27] L. Kipp, D. K. Biegelsen, J. E. Northrup, L.-E. Swartz, and R. D. Bringans, "Reflectance Difference Spectroscopy: Experiment and Theory for the Model System Si(001):As and Application to Si(001)," *Phys. Rev. Lett.* **76**(15), 2810 (1996) [doi:10.1103/PhysRevLett.76.2810].

[28] L. Mantese, U. Rossow, and D. E. Aspnes, "Surface-induced optical anisotropy of oxidized, clean, and hydrogenated vicinal Si(001) surfaces," *Appl. Surf. Sci.* **107**, 35–41 (1996) [doi:10.1016/S0169-4332(96)00479-5].

[29] R. J. Cole, S. Tanaka, P. Gerber, J. R. Power, T. Farrell, and P. Weightman, "Temperature-dependent optical anisotropy of the vicinal Si(001):(2 x 1) surface," *Phys. Rev. B* **54**(19), 13444 (1996) [doi:10.1103/PhysRevB.54.13444].

[30] R. Shioda and J. van der Weide, "Reflectance difference spectroscopy of highly oriented (2 x 1) reconstructed Si(001) surfaces," *Phys. Rev. B* **57**(12), R6823 (1998) [doi:10.1103/PhysRevB.57.R6823].

[31] R. Shioda and J. van der Weide, "Observation of hydrogen adsorption on Si(001) by reflectance difference spectroscopy," *Appl. Surf. Sci.* **130-132**, 266–270 (1998) [doi:10.1016/S0169-4332(98)00068-3].

[32] S. G. Jaloviar, J.-L. Lin, F. Liu, V. Zielasek, L. McCaughan, and M. G. Lagally, "Step-Induced Optical Anisotropy of Vicinal Si(001)," *Phys. Rev. Lett.* **82**(4), 791 (1999) [doi:10.1103/PhysRevLett.82.791].

[33] M. Palummo, G. Onida, R. Del Sole, and B. S. Mendoza, "Ab initio optical properties of Si(100)," *Phys. Rev. B* **60**(4), 2522 (1999) [doi:10.1103/PhysRevB.60.2522].

[34] K. Hingerl, R. E. Balderas-Navarro, A. Bonanni, P. Tichopadek, and W. G. Schmidt, "On the origin of resonance features in reflectance difference data of silicon," *Appl. Surf. Sci.* **175-176**, 769–776 (2001) [doi:10.1016/S0169-4332(01)00114-3].

[35] M. Palummo, N. Witkowski, O. Pluchery, R. Del Sole, and Y. Borensztein, "Reflectance-anisotropy spectroscopy and surface differential reflectance spectra at the Si(100) surface: Combined experimental and theoretical study," *Phys. Rev. B* **79**(3), 035327–035328 (2009) [doi:10.1103/PhysRevB.79.035327].

[36] T. Yasuda, L. Mantese, U. Rossow, and D. E. Aspnes, "Surface-Induced Optical Anisotropies of Single-Domain (2 x 1) Reconstructed (001) Si and Ge Surfaces," *Phys. Rev. Lett.* **74**(17), 3431 (1995) [doi:10.1103/PhysRevLett.74.3431].

[37] U. Rossow, L. Mantese, and D. E. Aspnes, "Surface-induced optical anisotropy of Si and Ge," *J. Vac. Sci. Technol. B Microelectron. Nanometer Struct.* **18**(4), 2229 (2000) [doi:10.1116/1.1306309].

[38] O. Supplie, "In situ Reflexions-Anisotropie-Spektroskopie an MOVPE-präpariertem GaP/Si(100)," diploma thesis, Humboldt-Universität zu Berlin (2010).

[39] S. R. Kurtz, A. A. Allerman, E. D. Jones, J. M. Gee, J. J. Banas, and B. E. Hammons, "InGaAsN solar cells with 1.0 eV band gap, lattice matched to GaAs," *Appl. Phys. Lett.* **74**(5), 729 –731 (1999) [doi:10.1063/1.123105].

[40] N. Szabó, B. E. Sağol, U. Seidel, K. Schwarzburg, and T. Hannappel, "InGaAsP/InGaAs tandem cells for a solar cell configuration with more than three junctions," *Phys. Status Solidi RRL – Rapid Res. Lett.* **2**(6), 254–256 (2008) [doi:10.1002/pssr.200802141].

[41] M. Yamaguchi and C. Amano, "Efficiency calculations of thin-film GaAs solar cells on Si substrates," *J. Appl. Phys.* **58**(9), 3601–3606 (1985) [doi:10.1063/1.335737].

[42] R. R. King, D. C. Law, K. M. Edmondson, C. M. Fetzer, G. S. Kinsey, H. Yoon, R. A. Sherif, and N. H. Karam, "40% efficient metamorphic GaInP⁄GaInAs⁄Ge multijunction solar cells," *Appl. Phys. Lett.* **90**, 183516 (2007) [doi:10.1063/1.2734507].

[43] J. H. van der Merwe, "Misfit dislocation generation in epitaxial layers," *Crit. Rev. Solid State Mater. Sci.* **17**(3), 187–209 (1991) [doi:10.1080/10408439108243751].

[44] M. Tachikawa and H. Mori, "Dislocation generation of GaAs on Si in the cooling stage," *Appl. Phys. Lett.* **56**(22), 2225–2227 (1990) [doi:10.1063/1.102951].

[45] R. M. Sieg, S. A. Ringel, S. M. Ting, E. A. Fitzgerald, and R. N. Sacks, "Anti-phase domain-free growth of GaAs on offcut (001) Ge wafers by molecular beam epitaxy with suppressed Ge outdiffusion," *J. Electron. Mater.* **27**(7), 900–907 (1998) [doi:10.1007/s11664-998-0116-1].

[46] B. Galiana, I. Rey-Stolle, C. Algora, K. Volz, and W. Stolz, "A GaAs metalorganic vapor phase epitaxy growth process to reduce Ge outdiffusion from the Ge substrate," *Appl. Phys. Lett.* **92**(15), 152102–152102–3 (2008) [doi:10.1063/1.2901029].

[47] H. Döscher, O. Supplie, S. Brückner, T. Hannappel, A. Beyer, J. Ohlmann, and K. Volz, "Indirect in situ characterization of Si(100) substrates at the initial stage of III-V heteroepitaxy," *J. Cryst. Growth* **315**(1), 16–21 (2011) [doi:16/j.jcrysgro.2010.08.017].

[48] D. J. Dunstan, "Mathematical model for strain relaxation in multilayer metamorphic epitaxial structures," *Philos. Mag. A* **73**(5), 1323–1332 (1996) [doi:10.1080/01418619608245135].

[49] S.-D. Kim, S. M. Lord, and J. James S. Harris, "Strain relaxation in compositionally graded epitaxial layers," *J. Vac. Sci. Technol. B Microelectron. Nanometer Struct.* **14**(2), 642–646 (1996) [doi:10.1116/1.589150].

[50] F. Romanato, E. Napolitani, A. Carnera, A. V. Drigo, L. Lazzarini, G. Salviati, C. Ferrari, A. Bosacchi, and S. Franchi, "Strain relaxation in graded composition $In_xGa_{1-x}As$/GaAs buffer layers," *J. Appl. Phys.* **86**(9), 4748–4755 (1999) [doi:10.1063/1.371439].

[51] S. Miyoshi, H. Yaguchi, K. Onabe, R. Ito, and Y. Shiraki, "Metalorganic vapor phase epitaxy of $GaP_{1-x}N_x$] alloys on GaP," *Appl. Phys. Lett.* **63**(25), 3506–3508 (1993) [doi:10.1063/1.110109].

[52] W. Shan, W. Walukiewicz, K. M. Yu, J. W. Ager, E. E. Haller, J. F. Geisz, D. J. Friedman, J. M. Olson, S. R. Kurtz, et al., "Effect of nitrogen on the electronic band structure of group III-N-V alloys," *Phys. Rev. B* **62**(7), 4211 (2000) [doi:10.1103/PhysRevB.62.4211].

[53] B. Kunert, K. Volz, J. Koch, and W. Stolz, "Direct-band-gap Ga(NAsP)-material system pseudomorphically grown on GaP substrate," *Appl. Phys. Lett.* **88**(18), 182108–3 (2006) [doi:10.1063/1.2200758].

[54] J. Bardeen and W. H. Brattain, "The Transistor, A Semi-Conductor Triode," *Phys. Rev.* **74**(2), 230–231 (1948) [doi:10.1103/PhysRev.74.230].

[55] C. O. Chui, H. Kim, P. C. McIntyre, and K. C. Saraswat, "Atomic layer deposition of high- kappa; dielectric for germanium MOS applications - substrate," *IEEE Electron Device Lett.* **25**(5), 274 – 276 (2004) [doi:10.1109/LED.2004.827285].

[56] G. Scappucci, G. Capellini, W. C. T. Lee, and M. Y. Simmons, "Atomic-scale patterning of hydrogen terminated Ge(001) by scanning tunneling microscopy," *Nanotechnology* **20**, 495302 (2009) [doi:10.1088/0957-4484/20/49/495302].

[57] R. E. Schlier and H. E. Farnsworth, "Structure and Adsorption Characteristics of Clean Surfaces of Germanium and Silicon," *J. Chem. Phys.* **30**(4), 917–926 (1959) [doi:10.1063/1.1730126].

[58] Y. Wang, M. Shi, and J. W. Rabalais, "Structure of the Si{100} surface in the clean (2×1), (2×1)-H monohydride, (1×1)-H dihydride, and c(4×4)-H phases," *Phys. Rev. B* **48**(3), 1678–1688 (1993) [doi:10.1103/PhysRevB.48.1678].

[59] P. Krüger and J. Pollmann, "Ab initio calculations of Si, As, S, Se, and Cl adsorption on Si(001) surfaces," *Phys. Rev. B* **47**(4), 1898–1910 (1993) [doi:10.1103/PhysRevB.47.1898].

[60] J. A. Appelbaum, G. A. Baraff, and D. R. Hamann, "The Si (100) surface. III. Surface reconstruction," *Phys. Rev. B* **14**(2), 588–601 (1976) [doi:10.1103/PhysRevB.14.588].

[61] H. J. W. Zandvliet, "The Ge(0 0 1) surface," *Phys. Rep.* **388**(1), 1–40 (2003) [doi:10.1016/j.physrep.2003.09.001].

[62] H. Over, J. Wasserfall, W. Ranke, C. Ambiatello, R. Sawitzki, D. Wolf, and W. Moritz, "Surface atomic geometry of Si(001)-(2×1): A low-energy electron-diffraction structure analysis," *Phys. Rev. B* **55**(7), 4731–4736 (1997) [doi:10.1103/PhysRevB.55.4731].

[63] E. L. Bullock, R. Gunnella, L. Patthey, T. Abukawa, S. Kono, C. R. Natoli, and L. S. O. Johansson, "Surface Core-Level Photoelectron Diffraction from Si Dimers at the Si(001)-(2×1) Surface," *Phys. Rev. Lett.* **74**(14), 2756–2759 (1995) [doi:10.1103/PhysRevLett.74.2756].

[64] R. A. Wolkow, "Direct observation of an increase in buckled dimers on Si(001) at low temperature," *Phys. Rev. Lett.* **68**(17), 2636–2639 (1992) [doi:10.1103/PhysRevLett.68.2636].

[65] R. M. Tromp, R. J. Hamers, and J. E. Demuth, "Si(001) Dimer Structure Observed with Scanning Tunneling Microscopy," *Phys. Rev. Lett.* **55**(12), 1303–1306 (1985) [doi:10.1103/PhysRevLett.55.1303].

[66] T. Tabata, T. Aruga, and Y. Murata, "Order-disorder transition on Si(001): c(4×2) to (2×1)," *Surf. Sci. Lett.* **179**(1), L63–L70 (1987) [doi:10.1016/0167-2584(87)90238-6].

[67] W. Mönch, *Semiconductor Surfaces and Interfaces*, 3rd ed., Springer (2001).

[68] J. J. Boland, "Structure of the H-saturated Si(100) surface," *Phys. Rev. Lett.* **65**(26), 3325–3328 (1990) [doi:10.1103/PhysRevLett.65.3325].

[69] K.Oura, V. G. Lifshits, A. A. Saranin, A. V. Zotov, M. Katayama;, *Surface Science, An Introduction*, Springer (2003).

[70] Y. J. Chabal and K. Raghavachari, "Surface Infrared Study of Si(100)-(2×1)H," *Phys. Rev. Lett.* **53**(3), 282–285 (1984) [doi:10.1103/PhysRevLett.53.282].

[71] J. E. Northrup, "Structure of Si(100)H: Dependence on the H chemical potential," *Phys. Rev. B* **44**(3), 1419 (1991) [doi:10.1103/PhysRevB.44.1419].

[72] Y. J. Chabal, A. L. Harris, K. Raghavachari, and J. C. Tully, "Infrared spectroscopy of H-terminated silicon surfaces," *Int. J. Mod. Phys. B* **07**(04), 1031–1078 (1993) [doi:10.1142/S0217979293002237].

[73] P. Gupta, V. L. Colvin, and S. M. George, "Hydrogen desorption kinetics from monohydride and dihydride species on silicon surfaces," *Phys. Rev. B* **37**(14), 8234–8243 (1988) [doi:10.1103/PhysRevB.37.8234].

[74] K. Sinniah, M. G. Sherman, L. B. Lewis, W. H. Weinberg, J. T. Yates, and K. C. Janda, "New Mechanism for Hydrogen Desorption from Covalent Surfaces: The Monohydride Phase on Si(100)," *Phys. Rev. Lett.* **62**(5), 567–570 (1989) [doi:10.1103/PhysRevLett.62.567].

[75] K. Sinniah, M. G. Sherman, L. B. Lewis, W. H. Weinberg, J. T. Yates, and K. C. Janda, "Hydrogen desorption from the monohydride phase on Si(100)," *J. Chem. Phys.* **92**(9), 5700 (1990) [doi:10.1063/1.458501].

[76] K. W. Kolasinski, W. Nessler, A. de Meijere, and E. Hasselbrink, "Hydrogen adsorption on and desorption from Si: Considerations on the applicability of detailed balance," *Phys. Rev. Lett.* **72**(9), 1356 (1994) [doi:10.1103/PhysRevLett.72.1356].

[77] M. Dürr and U. Höfer, "Dissociative adsorption of molecular hydrogen on silicon surfaces," *Surf. Sci. Rep.* **61**(12), 465–526 (2006) [doi:10.1016/j.surfrep.2006.08.002].

[78] T. Aoyama, K. Goto, T. Yamazaki, and T. Ito, "Silicon (001) surface after annealing in hydrogen ambient," *J. Vac. Sci. Technol. Vac. Surf. Films* **14**(5), 2909–2915 (1996) [doi:10.1116/1.580244].

[79] H. Bender, S. Verhaverbeke, M. Caymax, O. Vatel, and M. M. Heyns, "Surface reconstruction of hydrogen annealed (100) silicon," *J. Appl. Phys.* **75**(2), 1207–1209 (1994) [doi:doi:10.1063/1.356478].

[80] T. Komeda and Y. Kumagai, "Si(001) surface variation with annealing in ambient H_2," *Phys. Rev. B* **58**(3), 1385 (1998) [doi:10.1103/PhysRevB.58.1385].

[81] J. Y. Maeng, J. Y. Lee, Y. E. Cho, S. Kim, and S. K. Jo, "Surface dihydrides on Ge(100): A scanning tunneling microscopy study," *Appl. Phys. Lett.* **81**, 3555 (2002) [doi:10.1063/1.1520329].

[82] S. Rivillon, Y. J. Chabal, F. Amy, and A. Kahn, "Hydrogen passivation of germanium (100) surface using wet chemical preparation," *Appl. Phys. Lett.* **87**(25), 253101 (2005) [doi:10.1063/1.2142084].

[83] M. P. D'Evelyn, S. M. Cohen, E. Rouchouze, and Y. L. Yang, "Surface π bonding and the near-first-order desorption kinetics of hydrogen from Ge(100)2×1," *J. Chem. Phys.* **98**(4), 3560–3563 (1993) [doi:10.1063/1.464078].

[84] J. Y. Lee, J. Y. Maeng, A. Kim, Y. E. Cho, and S. Kim, "Kinetics of H_2 (D_2) desorption from a Ge(100)-2×1:H (D) surface studied using scanning tunneling microscopy and temperature programmed desorption," *J. Chem. Phys.* **118**(4), 1929 (2003) [doi:10.1063/1.1531662].

[85] L. B. Lewis, J. Segall, and K. C. Janda, "Recombinative desorption of hydrogen from the Ge(100)–(2×1) surface: A laser-induced desorption study," *J. Chem. Phys.* **102**(18), 7222–7228 (1995) [doi:10.1063/1.469117].

[86] P. E. Wierenga, J. A. Kubby, and J. E. Griffith, "Tunneling images of biatomic steps on Si(001)," *Phys. Rev. Lett.* **59**(19), 2169–2172 (1987) [doi:10.1103/PhysRevLett.59.2169].

[87] J. E. Griffith, J. A. Kubby, P. E. Wierenga, R. S. Becker, and J. S. Vickers, "Tunneling microscopy of steps on vicinal Ge(001) and Si(001) surfaces," *J. Vac. Sci. Technol. Vac. Surf. Films* **6**(2), 493–496 (1988) [doi:10.1116/1.575366].

[88] R. Kaplan, "LEED study of the stepped surface of vicinal Si (100)," *Surf. Sci.* **93**(1), 145–158 (1980) [doi:10.1016/0039-6028(80)90052-7].

[89] T. W. Poon, S. Yip, P. S. Ho, and F. F. Abraham, "Equilibrium structures of Si(100) stepped surfaces," *Phys. Rev. Lett.* **65**(17), 2161–2164 (1990) [doi:10.1103/PhysRevLett.65.2161].

[90] F. K. Men, W. E. Packard, and M. B. Webb, "Si(100) Surface under an Externally Applied Stress," *Phys. Rev. Lett.* **61**(21), 2469–2471 (1988) [doi:10.1103/PhysRevLett.61.2469].

[91] T. Doi, M. Ichikawa, S. Hosoki, and K. Ninomiya, "Anisotropic diffusion between the step-up and the step-down directions on a Si(001) surface," *Phys. Rev. B* **53**(24), 16609–16614 (1996) [doi:10.1103/PhysRevB.53.16609].

[92] P. Bedrossian and T. Klitsner, "Anisotropic vacancy kinetics and single-domain stabilization on Si(100)-2×1," *Phys. Rev. Lett.* **68**(5), 646–649 (1992) [doi:10.1103/PhysRevLett.68.646].

[93] B. S. Swartzentruber, C. M. Matzke, D. L. Kendall, and J. E. Houston, "STM measurements of step-flow kinetics during atom removal by low-energy-ion bombardment of Si(001)," *Surf. Sci.* **329**(1–2), 83–89 (1995) [doi:10.1016/0039-6028(95)00042-9].

[94] H. Döscher, P. Kleinschmidt, and T. Hannappel, "Atomic surface structure of Si(100) substrates prepared in a chemical vapor environment," *Appl. Surf. Sci.* **257**(2), 574–580 (2010) [doi:10.1016/j.apsusc.2010.07.035].

[95] K. Kitahara and O. Ueda, "Observation of Atomic Structure by Scanning Tunneling Microscopy of Vicinal Si(100) Surface Annealed in Hydrogen Gas," *Jpn. J. Appl. Phys.* **33**(Part 2, No. 11B), L1571–L1573 (1994) [doi:10.1143/JJAP.33.L1571].

[96] C. Roland and G. H. Gilmer, "Epitaxy on surfaces vicinal to Si(001). II. Growth properties of Si(001) steps," *Phys. Rev. B* **46**(20), 13437 (1992) [doi:10.1103/PhysRevB.46.13437].

[97] A. J. Hoeven, J. M. Lenssinck, D. Dijkkamp, E. J. van Loenen, and J. Dieleman, "Scanning-tunneling-microscopy study of single-domain Si(001) surfaces grown by molecular-beam epitaxy," *Phys. Rev. Lett.* **63**(17), 1830–1832 (1989) [doi:10.1103/PhysRevLett.63.1830].

[98] P. Bedrossian, J. E. Houston, J. Y. Tsao, E. Chason, and S. T. Picraux, "Layer-by-layer sputtering and epitaxy of Si(100)," *Phys. Rev. Lett.* **67**(1), 124–127 (1991) [doi:10.1103/PhysRevLett.67.124].

[99] Z. Zhang, H. Chen, B. C. Bolding, and M. G. Lagally, "Vacancy diffusion on Si(100)-(2×1)," *Phys. Rev. Lett.* **71**(22), 3677–3680 (1993) [doi:10.1103/PhysRevLett.71.3677].

[100] Y. Kumagai, K. Namba, T. Komeda, and Y. Nishioka, "Formation of periodic step and terrace structure on Si(100) surface during annealing in hydrogen diluted with

inert gas," in *Pap. 44th Natl. Symp. AVS* **16**, pp. 1775–1778, AVS (1998) [doi:10.1116/1.581301].

[101] B. M. Gallois, T. M. Besmann, and M. W. Stott, "Chemical Etching of Silicon (100) by Hydrogen," *J. Am. Ceram. Soc.* **77**(11), 2949–2952 (1994) [doi:10.1111/j.1151-2916.1994.tb04529.x].

[102] H. Habuka, H. Tsunoda, M. Mayusumi, N. Tate, and M. Katayama, "Roughness of Silicon Surface Heated in Hydrogen Ambient," *J. Electrochem. Soc.* **142**(9), 3092–3098 (1995) [doi:10.1149/1.2048694].

[103] J. Nara, T. Sasaki, and T. Ohno, "Adsorption and Diffusion of Si Atoms on the H-Terminated Si(001) Surface: Si Migration Assisted by H Mobility," *Phys. Rev. Lett.* **79**(22), 4421–4424 (1997) [doi:10.1103/PhysRevLett.79.4421].

[104] S. M. Ting and E. A. Fitzgerald, "Metal-organic chemical vapor deposition of single domain GaAs on Ge/Ge_xSi_{1-x}/Si and Ge substrates," *J. Appl. Phys.* **87**(5), 2618 (2000) [doi:10.1063/1.372227].

[105] Y. Li, L. Lazzarini, L. J. Giling, and G. Salviati, "On the sublattice location of GaAs grown on Ge," *J. Appl. Phys.* **76**(10), 5748 (1994) [doi:10.1063/1.358412].

[106] B. Galiana, I. Rey-Stolle, I. Beinik, C. Algora, C. Teichert, J. M. Molina-Aldareguia, and P. Tejedor, "Characterization of antiphase domains on GaAs grown on Ge substrates by conductive atomic force microscopy for photovoltaic applications," *Sol. Energy Mater. Sol. Cells* **95**(7), 1949–1954 (2011) [doi:10.1016/j.solmat.2010.12.021].

[107] H. W. Yu, E. Y. Chang, Y. Yamamoto, B. Tillack, W. C. Wang, C. I. Kuo, Y. Y. Wong, and H. Q. Nguyen, "Effect of graded-temperature arsenic prelayer on quality of GaAs on Ge/Si substrates by metalorganic vapor phase epitaxy," *Appl. Phys. Lett.* **99**, 171908 (2011) [doi:10.1063/1.3656737].

[108] W. E. McMahon, A. E. Kibbler, and J. M. Olson, "An STM and LEED study of MOCVD-prepared P/Ge (1 0 0) to (1 1 1) surfaces," *Surf. Sci.* **571**(1-3), 146–156 (2004) [doi:10.1016/j.susc.2004.08.008].

[109] E. Barrigon, B. Galiana, and I. Rey-Stolle, "Reflectance anisotropy spectroscopy assessment of the MOVPE nucleation of GaInP on germanium (1 0 0)," *J. Cryst. Growth* **315**(1), 22–27 (2011) [doi:10.1016/j.jcrysgro.2010.09.038].

[110] W. E. McMahon and J. M. Olson, "Atomic-resolution study of steps and ridges on arsine-exposed vicinal Ge(100)," *Phys. Rev. B* **60**(4), 2480 (1999) [doi:10.1103/PhysRevB.60.2480].

[111] W. E. McMahon and J. M. Olson, "Atomic-resolution STM study of a structural phase transition of steps on vicinal As/Ge(100)," *Phys. Rev. B* **60**(23), 15999 (1999) [doi:10.1103/PhysRevB.60.15999].

[112] S. Gan, L. Li, M. J. Begarney, D. Law, B.-K. Han, and R. F. Hicks, "Step structure of arsenic-terminated vicinal Ge (100)," *J. Appl. Phys.* **85**(3), 2004 (1999) [doi:10.1063/1.369176].

[113] R. D. Bringans, D. K. Biegelsen, and L.-E. Swartz, "Atomic-step rearrangement on Si(100) by interaction with arsenic and the implication for GaAs-on-Si epitaxy," *Phys. Rev. B* **44**(7), 3054 (1991) [doi:10.1103/PhysRevB.44.3054].

[114] R. S. Becker, T. Klitsner, and J. S. Vickers, "Arsenic-terminated silicon and germanium surfaces studied by scanning tunnelling microscopy," *Mon. Microsc. J.* **3**(2), 157–165 (1870) [doi:10.1111/j.1365-2818.1870.tb06341.x].

[115] O. L. Alerhand, J. Wang, J. D. Joannopoulos, E. Kaxiras, and R. S. Becker, "Adsorption of As on stepped Si(100): Resolution of the sublattice-orientation dilemma," *Phys. Rev. B* **44**(12), 6534 (1991) [doi:10.1103/PhysRevB.44.6534].

[116] R. M. Tromp, A. W. Denier van der Gon, and M. C. Reuter, "Surface stress as a driving force for interfacial mixing," *Phys. Rev. Lett.* **68**(15), 2313–2316 (1992) [doi:10.1103/PhysRevLett.68.2313].

[117] B. D. Yu and A. Oshiyama, "Dimer exchange mechanism for substitutional As adsorption on Si(100)," *Phys. Rev. Lett.* **71**(4), 585–588 (1993) [doi:10.1103/PhysRevLett.71.585].

[118] Y. Shimamune, M. Sakuraba, T. Matsuura, and J. Murota, "Atomic-layer adsorption of P on Si(100) and Ge(100) by PH_3 using an ultraclean low-pressure chemical vapor deposition," *Appl. Surf. Sci.* **162-163**, 390–394 (2000) [doi:10.1016/S0169-4332(00)00221-X].

[119] W. E. McMahon and J. M. Olson, "A scanning tunneling microscopy study of As/Ge(mnn) and P/Ge(mnn) surfaces," *J. Cryst. Growth* **225**(2-4), 410–414 (2001) [doi:10.1016/S0022-0248(01)00901-0].

[120] H. M. Manasevit, "Single-crystal gallium arsenide on insulating substrates," *Appl. Phys. Lett.* **12**(4), 156–159 (1968) [doi:10.1063/1.1651934].

[121] H. M. Manasevit and W. I. Simpson, "The use of metal-organics in the preparation of semiconductor materials: I. Epitaxial gallium–V compounds," *J. Electrochem. Soc.* **116**(12), 1725–1732 (1969) [doi:10.1149/1.2411685].

[122] K. Möller, "In situ Überwachung der MOCVD-Präparation von Gallium- und Indiumantimonid," PhD thesis, Universität Duisburg Essen (2006).

[123] U. Seidel, "Grenzflächenuntersuchungen am Tunnelkontakt einer MOCVD-präparierten Tandemsolarzelle," PhD thesis, Humboldt-Universität zu Berlin (2007).

[124] D. Rönnow, L. F. Lastras-Martínez, M. Cardona, and P. V. Santos, "Determination of the piezo-optical properties of semiconductors above the fundamental gap by means of reflectance difference spectroscopy," *J. Opt. Soc. Am. A* **16**(3), 568–573 (1999) [doi:10.1364/JOSAA.16.000568].

[125] O. Hunderi, J.-T. Zettler, and K. Haberland, "On the AlAs/GaAs (001) interface dielectric anisotropy," *Thin Solid Films* **472**(1-2), 261–269 (2005) [doi:10.1016/j.tsf.2004.06.150].

[126] T. Yasuda, "Interface, surface and bulk anisotropies of heterostructures," *Thin Solid Films* **313–314**, 544–551 (1998) [doi:10.1016/S0040-6090(97)00881-X].

[127] T. Hannappel, S. Visbeck, L. Töben, and F. Willig, "Apparatus for investigating metalorganic chemical vapor deposition-grown semiconductors with ultrahigh-vacuum based techniques," *Rev. Sci. Instrum.* **75**(5), 1297 (2004) [doi:10.1063/1.1711148].

[128] D. E. Aspnes, J. P. Harbison, A. A. Studna, and L. T. Florez, "Application of reflectance difference spectroscopy to molecular-beam epitaxy growth of GaAs and AlAs," *J. Vac. Sci. Technol. Vac. Surf. Films* **6**(3), 1327–1332 (1988) [doi:10.1116/1.575694].

[129] C. Kaspari, M. Pristovsek, and W. Richter, "A fast reflectance anisotropy spectrometer for in situ growth monitoring," *Phys. Status Solidi B* **242**(13), 2561–2569 (2005) [doi:10.1002/pssb.200541143].

[130] K. Haberland, "Optical in-situ studies during metal-organic vapor phase epitaxy with respect to III-V device production," PhD thesis, Technische Universität Berlin (2002).

[131] K. Haberland, P. Kurpas, M. Pristovsek, J.-T. Zettler, M. Weyers, and W. Richter, "Spectroscopic process sensors in MOVPE device production," *Appl. Phys. A* **68**(3), 309–313 (1999) [doi:10.1007/s003390050893].

[132] H. Hertz, "Ueber einen Einfluss des ultravioletten Lichtes auf die electrische Entladung," *Ann. Phys.* **267**(8), 983–1000 (1887) [doi:10.1002/andp.18872670827].

[133] A. Einstein, "Über einen die Erzeugung und Verwandlung des Lichtes betreffenden heuristischen Gesichtspunkt," *Ann. Phys.* **322**(6), 132–148 (1905) [doi:10.1002/andp.19053220607].

[134] H. Lüth, “Surface and Interface Physics: Its Definition and Importance,” in *Solid Surf. Interfaces Thin Films*, pp. 1–28, Springer (2010).

[135] M. P. Seah and W. A. Dench, “Quantitative electron spectroscopy of surfaces: A standard data base for electron inelastic mean free paths in solids,” *Surf. Interface Anal.* **1**(1), 2–11 (1979) [doi:10.1002/sia.740010103].

[136] S. Hüfner, *Photoelectron Spectroscopy - Principles and Applications*, Springer (1995).

[137] “Casa xps,” <http://www.casaxps.com/> (21 September 2011).

[138] J. Küppers and G. Ertl, *Low energy electrons and surface chemistry*, 2nd, completely rev. ed., Wiley-VCH (1985).

[139] M. Henzler and W. Göpel, *Oberflächenphysik des Festkörpers*, 2nd ed., Teubner Verlag (1994).

[140] H. Ibach and H. Lüth, *Solid-State Physics - An Introduction to Principles of Materials Science*, 4th ed., Springer (2009).

[141] R. H. Fowler and L. Nordheim, “Electron Emission in Intense Electric Fields,” *Proc. R. Soc. Lond. Ser. A* **119**(781), 173–181 (1928) [doi:10.1098/rspa.1928.0091].

[142] P. K. Hansma and J. Tersoff, “Scanning tunneling microscopy,” *J. Appl. Phys.* **61**(2), R1–R24 (1987) [doi:10.1063/1.338189].

[143] D. Bonnel, *Scanning Probe Microscopy and Spectroscopy: Theory, Techniques, and Applications*, 2nd ed., Wiley-VCH (2000).

[144] Y. J. Chabal, G. S. Higashi, and S. B. Christman, “Hydrogen chemisorption on Si(111)-(7×7) and -(1×1) surfaces. A comparative infrared study,” *Phys. Rev. B* **28**(8), 4472–4479 (1983) [doi:10.1103/PhysRevB.28.4472].

[145] A. Dobrich, “Wasserstoffbindungen an Silizium-Halbleiteroberflächen aus MOCVD-Präparation,” diploma thesis, Freie Universität Berlin (2009).

[146] A. Ishizaka and Y. Shiraki, “Low Temperature Surface Cleaning of Silicon and Its Application to Silicon MBE,” *J. Electrochem. Soc.* **133**(4), 666–671 (1986) [doi:10.1149/1.2108651].

[147] H. Döscher, S. Brückner, A. Dobrich, C. Höhn, P. Kleinschmidt, and T. Hannappel, “Surface preparation of Si(100) by thermal oxide removal in a chemical vapor environment,” *J. Cryst. Growth* **315**(1), 10–15 (2011) [doi:10.1016/j.jcrysgro.2010.07.017].

[148] H. Döscher, S. Brückner, and T. Hannappel, "Investigation of oxide removal from Si(100) substrates in dependence of the MOVPE process gas ambient," *J. Cryst. Growth* **318**(1), 563–569 (2011) [doi:16/j.jcrysgro.2010.11.087].

[149] M. Morita, T. Ohmi, E. Hasegawa, M. Kawakami, and M. Ohwada, "Growth of native oxide on a silicon surface," *J. Appl. Phys.* **68**(3), 1272–1281 (1990) [doi:10.1063/1.347181].

[150] H. Neergaard Waltenburg and J. T. Yates, "Surface Chemistry of Silicon," *Chem. Rev.* **95**(5), 1589–1673 (1995) [doi:10.1021/cr00037a600].

[151] T. L. Barr, "An XPS study of Si as it occurs in adsorbents, catalysts, and thin films," *Appl. Surf. Sci.* **15**(1–4), 1–35 (1983) [doi:10.1016/0378-5963(83)90003-X].

[152] M. S. Hegde, R. Caracciolo, K. S. Hatton, and J. B. Wachtman Jr., "Electronic structure and bonding in silicon oxynitride films: An XPS study," *Appl. Surf. Sci.* **37**(1), 16–24 (1989) [doi:10.1016/0169-4332(89)90969-0].

[153] R. I. G. Uhrberg, E. Landemark, and Y.-C. Chao, "High-resolution core-level studies of silicon surfaces," *J. Electron Spectrosc. Relat. Phenom.* **75**, 197–207 (1995) [doi:10.1016/0368-2048(95)02538-3].

[154] M. L. Green, E. P. Gusev, R. Degraeve, and E. L. Garfunkel, "Ultrathin (<4 nm) SiO_2 and Si–O–N gate dielectric layers for silicon microelectronics: Understanding the processing, structure, and physical and electrical limits," *J. Appl. Phys.* **90**(5), 2057–2121 (2001) [doi:10.1063/1.1385803].

[155] Z. H. Lu, M. J. Graham, D. T. Jiang, and K. H. Tan, "SiO_2/Si(100) interface studied by Al Kα x-ray and synchrotron radiation photoelectron spectroscopy," *Appl. Phys. Lett.* **63**(21), 2941–2943 (1993) [doi:10.1063/1.110279].

[156] M. Niwano, H. Katakura, Y. Takeda, Y. Takakuwa, N. Miyamoto, A. Hiraiwa, and K. Yagi, "Photoemission study of the SiO_2/Si interface structure of thin oxide films on Si(100), (111), and (110) surfaces," *J. Vac. Sci. Technol. Vac. Surf. Films* **9**(2), 195–200 (1991) [doi:10.1116/1.577520].

[157] H. Hibino, M. Uematsu, and Y. Watanabe, "Void growth during thermal decomposition of silicon oxide layers studied by low-energy electron microscopy," *J. Appl. Phys.* **100**(11), 113519–113519–8 (2006) [doi:10.1063/1.2397283].

[158] R. Tromp, G. Rubloff, P. Balk, F. LeGoues, and E. van Loenen, "High-Temperature SiO2 Decomposition at the SiO2/Si Interface," *Phys. Rev. Lett.* **55**(21), 2332–2335 (1985) [doi:10.1103/PhysRevLett.55.2332].

[159] K. Fujita, H. Watanabe, and M. Ichikawa, "Scanning tunneling microscopy study on void formation by thermal decomposition of thin oxide layers on stepped Si surfaces," *J. Appl. Phys.* **83**(8), 4091–4095 (1998) [doi:10.1063/1.367162].

[160] Y. Wei, R. M. Wallace, and A. C. Seabaugh, "Void formation on ultrathin thermal silicon oxide films on the Si(100) surface," *Appl. Phys. Lett.* **69**(9), 1270–1272 (1996) [doi:10.1063/1.117388].

[161] G. W. Rubloff, "Defect microchemistry in SiO2/Si structures," *J. Vac. Sci. Technol. Vac. Surf. Films* **8**(3), 1857–1863 (1990) [doi:10.1116/1.576816].

[162] T. Yamazaki, N. Miyata, T. Aoyama, and T. Ito, "Investigation of Thermal Removal of Native Oxide from Si (100) Surfaces in Hydrogen for Low-Temperature Si CVD Epitaxy," *J. Electrochem. Soc.* **139**(4), 1175–1180 (1992) [doi:10.1149/1.2069361].

[163] M. Grundmann, A. Krost, and D. Bimberg, "Observation of the first-order phase transition from single to double stepped Si (001) in metalorganic chemical vapor deposition of InP on Si," *J. Vac. Sci. Technol. B Microelectron. Nanometer Struct.* **9**(4), 2158–2166 (1991) [doi:10.1116/1.585757].

[164] Z. Zhang, F. Wu, and M. G. Lagally, "An atomistic view of Si(001) homoepitaxy 1," *Annu. Rev. Mater. Sci.* **27**(1), 525–553 (1997) [doi:10.1146/annurev.matsci.27.1.525].

[165] Y. J. Chabal, "High-resolution infrared spectroscopy of adsorbates on semiconductor surfaces: Hydrogen on Si(100) and Ge(100)," *Surf. Sci.* **168**(1-3), 594–608 (1986) [doi:10.1016/0039-6028(86)90890-3].

[166] T.-C. Shen, C. Wang, G. C. Abeln, J. R. Tucker, J. W. Lyding, P. Avouris, and R. E. Walkup, "Atomic-Scale Desorption Through Electronic and Vibrational Excitation Mechanisms," *Science* **268**(5217), 1590–1592 (1995) [doi:10.1126/science.268.5217.1590].

[167] J. J. Boland, "Evidence of pairing and its role in the recombinative desorption of hydrogen from the Si(100)-2×1 surface," *Phys. Rev. Lett.* **67**(12), 1539–1542 (1991) [doi:10.1103/PhysRevLett.67.1539].

[168] Y. Borensztein and N. Witkowski, "Optical response of clean and hydrogen-covered vicinal Si(001) 2 × 1 surfaces," *J. Phys. Condens. Matter* **16**(39), S4301–S4311 (2004) [doi:10.1088/0953-8984/16/39/005].

[169] R. D. Sole and G. Onida, "Surface versus crystal-termination effects in the optical properties of surfaces," *Phys. Rev. B* **60**(8), 5523–5528 (1999) [doi:10.1103/PhysRevB.60.5523].

[170] S. Brückner, H. Döscher, P. Kleinschmidt, and T. Hannappel, "In situ investigation of hydrogen interacting with Si(100)," *Appl. Phys. Lett.* **98**(21), 211909 (2011) [doi:10.1063/1.3593195].

[171] S. Brückner, H. Döscher, P. Kleinschmidt, O. Supplie, A. Dobrich, and T. Hannappel, "Anomalous double-layer step formation on Si(100) in hydrogen process ambient," *Phys. Rev. B* **86**(19), 195310 (2012) [doi:10.1103/PhysRevB.86.195310].

[172] S. Brückner, P. Kleinschmidt, O. Supplie, H. Döscher, and T. Hannappel, "Domain-sensitive in situ observation of layer-by-layer removal at Si(100) in H_2 ambient," *New J. Phys.* **15**(11), 113049 (2013) [doi:10.1088/1367-2630/15/11/113049].

[173] O. Supplie, S. Brückner, O. Romanyuk, H. Döscher, P. Kleinschmidt, F. Grosse, and T. Hannappel, "Atomic scale analysis of the GaP/Si(100) heterointerface by in situ reflection anisotropy spectroscopy and ab initio density functional theory," *submitted* (2013).

[174] S. Brückner, H. Döscher, T. Hannappel, P. Kleinschmidt, O. Supplie, and A. Dobrich, "Verfahren zur Oberflächenpräparation von Si(100)-Substraten," Deutsche Patentanmeldung 102011122749.4 (2013).

[175] G.-P. Tang, E. Peiner, H.-H. Wehmann, A. Lubnow, G. Zwinge, A. Schlachetzki, and J. Hergeth, "A new maskless selective-growth process for InP on (100) Si," *J. Appl. Phys.* **72**(9), 4366–4368 (1992) [doi:10.1063/1.352201].

[176] H. Döscher and T. Hannappel, "In situ reflection anisotropy spectroscopy analysis of heteroepitaxial GaP films grown on Si(100)," *J. Appl. Phys.* **107**(12), 123523–123523–12 (2010) [doi:10.1063/1.3357391].

[177] H. Döscher, T. Hannappel, B. Kunert, A. Beyer, K. Volz, and W. Stolz, "In situ verification of single-domain III-V on Si(100) growth via metal-organic vapor phase epitaxy," *Appl. Phys. Lett.* **93**(17), 172110–172113 (2008) [doi:10.1063/1.3009570].

[178] S. Visbeck, T. Hannappel, M. Zorn, J.-T. Zettler, and F. Willig, "Temperature dependence and origin of InP(100) reflectance anisotropy down to 20 K," *Phys. Rev. B* **63**(24), 245303 (2001) [doi:10.1103/PhysRevB.63.245303].

[179] P. I. Cohen, P. R. Pukite, J. M. V. Hove, and C. S. Lent, "Reflection high energy electron diffraction studies of epitaxial growth on semiconductor surfaces," *J. Vac. Sci. Technol. Vac. Surf. Films* **4**(3), 1251–1258 (1986) [doi:10.1116/1.573410].

[180] B. Poelsema, L. K. Verheij, and G. Comsa, "'Two-Layer' Behavior of the Pt(111) Surface during Low-Energy Ar+-Ion Sputtering at High Temperatures," *Phys. Rev. Lett.* **53**(26), 2500–2503 (1984) [doi:10.1103/PhysRevLett.53.2500].

[181] D. York, "Least-squares fitting of a straight line," *Can. J. Phys.* **44**(5), 1079–1086 (1966) [doi:10.1139/p66-090].

[182] R. E. Honig, "Sublimation Studies of Silicon in the Mass Spectrometer," *J. Chem. Phys.* **22**(9), 1610–1611 (1954) [doi:10.1063/1.1740469].

[183] S. Brückner, E. Barrigón, O. Supplie, P. Kleinschmidt, A. Dobrich, C. Löbbel, I. Rey-Stolle, H. Döscher, and T. Hannappel, "Ge(100) surfaces prepared in vapor phase epitaxy process ambient," *Phys. Status Solidi RRL – Rapid Res. Lett.* **6**(4), 178–180 (2012) [doi:10.1002/pssr.201206028].

[184] E. Barrigón, S. Brückner, O. Supplie, P. Kleinschmidt, I. Rey-Stolle, and T. Hannappel, "Optical in situ monitoring of hydrogen desorption from Ge(100) surfaces," *Appl. Phys. Lett.* **102**(11), 111608–111608–4 (2013) [doi:10.1063/1.4798248].

[185] S. Brückner, O. Supplie, E. Barrigón, J. Luczak, P. Kleinschmidt, I. Rey-Stolle, H. Döscher, and T. Hannappel, "In situ control of As dimer orientation on Ge(100) surfaces," *Appl. Phys. Lett.* **101**(12), 121602–121602–4 (2012) [doi:doi:10.1063/1.4754122].

[186] E. Barrigón, S. Brückner, O. Supplie, H. Döscher, I. Rey-Stolle, and T. Hannappel, "In situ study of Ge(100) surfaces with tertiarybutylphosphine supply in vapor phase epitaxy ambient," *J. Cryst. Growth* **370**, 173–176 (2013) [doi:10.1016/j.jcrysgro.2012.07.046].

[187] K. Prabhakaran and T. Ogino, "Oxidation of Ge(100) and Ge(111) surfaces: an UPS and XPS study," *Surf. Sci.* **325**(3), 263–271 (1995) [doi:10.1016/0039-6028(94)00746-2].

[188] J. Oh and J. C. Campbell, "Thermal desorption of Ge native oxides and the loss of Ge from the surface," *J. Electron. Mater.* **33**(4), 364–367 (2004) [doi:10.1007/s11664-004-0144-4].

[189] S. Gan, L. Li, T. Nguyen, H. Qi, R. . Hicks, and M. Yang, "Scanning tunneling microscopy of chemically cleaned germanium (100) surfaces," *Surf. Sci.* **395**(1), 69–74 (1998) [doi:10.1016/S0039-6028(97)00608-0].

[190] J. S. Hovis, R. J. Hamers, and C. M. Greenlief, "Preparation of clean and atomically flat germanium(001) surfaces," *Surf. Sci.* **440**(1-2), L815–L819 (1999) [doi:10.1016/S0039-6028(99)00866-3].

[191] E. Antonides, E. C. Janse, and G. A. Sawatzky, "LMM Auger spectra of Cu, Zn, Ga, and Ge. I. Transition probabilities, term splittings, and effective Coulomb interaction," *Phys. Rev. B* **15**(4), 1669 (1977) [doi:10.1103/PhysRevB.15.1669].

[192] C. Tegenkamp, J. Wollschläger, H. Pfnür, F.-J. Meyer zu Heringdorf, and M. Horn-von Hoegen, "Step and kink correlations on vicinal Ge(100) surfaces investigated by electron diffraction," *Phys. Rev. B* **65**(23), 235316 (2002) [doi:10.1103/PhysRevB.65.235316].

[193] J. J. Boland, "Scanning tunneling microscopy study of the adsorption and recombinative desorption of hydrogen from the Si(100)-2 x 1 surface," in *38th Natl. Symp. Am. Vac. Soc.* **10**, pp. 2458–2464, AVS (1992) [doi:10.1116/1.577984].

[194] W. G. Schmidt, N. Esser, A. M. Frisch, P. Vogt, J. Bernholc, F. Bechstedt, M. Zorn, T. Hannappel, S. Visbeck, et al., "Understanding reflectance anisotropy: Surface-state signatures and bulk-related features in the optical spectrum of InP(001)(2×4)," *Phys. Rev. B* **61**(24), R16335–R16338 (2000) [doi:10.1103/PhysRevB.61.R16335].

[195] G. Eres, "Investigation of the kinetics of digermane chemisorption and reaction product desorption in thin film growth of germanium," *J. Vac. Sci. Technol. Vac. Surf. Films* **11**(5), 2463 (1993) [doi:10.1116/1.578593].

[196] H. Gant and W. Mönch, "Electron escape depths in germanium," *Surf. Sci.* **105**(1), 217–224 (1981) [doi:10.1016/0039-6028(81)90157-6].

[197] J. Szajman, J. G. Jenkin, J. Liesegang, and R. C. G. Leckey, "Electron mean free paths in ge in the range 70–1400 eV," *J. Electron Spectrosc. Relat. Phenom.* **14**(1), 41–48 (1978) [doi:10.1016/0368-2048(78)85053-1].

[198] J. F. Morar, U. O. Karlsson, R. I. G. Uhrberg, J. Kanski, P. O. Nilsson, and H. Qu, "Angle-resolved photoemission study of the As/Ge(100) interface," *Appl. Surf. Sci.* **41–42**(0), 312–316 (1989) [doi:10.1016/0169-4332(89)90077-9].

[199] R. Tyagi, M. Singh, M. Thirumavalavan, T. Srinivasan, and S. K. Agarwal, "The influence of As and Ga prelayers on the metal-organic chemical vapor deposition of GaAs/Ge," *J. Electron. Mater.* **31**(3), 234–237 (2002) [doi:10.1007/s11664-002-0212-6].

[200] P. Vogt, T. Hannappel, S. Visbeck, K. Knorr, N. Esser, and W. Richter, "Atomic surface structure of the phosphorous-terminated InP(001) grown by MOVPE," *Phys. Rev. B* **60**(8), R5117 (1999) [doi:10.1103/PhysRevB.60.R5117].

[201] B. Galiana, E. Barrigón, I. Rey-Stolle, V. Corregidor, P. Espinet, C. Algora, and E. Alves, "Compositional analysis and evolution of defects formed on GaInP

epilayers grown on Germanium," *Superlattices Microstruct.* **45**(4-5), 277–284 (2009) [doi:10.1016/j.spmi.2008.12.013].

[202] W. He, S. L. Lu, J. R. Dong, Y. M. Zhao, X. Y. Ren, K. L. Xiong, B. Li, H. Yang, H. M. Zhu, et al., "Structural and optical properties of GaInP grown on germanium by metal-organic chemical vapor deposition," *Appl. Phys. Lett.* **97**(12), 121909 (2010) [doi:10.1063/1.3492854].

[203] K. Volz, A. Beyer, W. Witte, J. Ohlmann, I. Németh, B. Kunert, and W. Stolz, "GaP-nucleation on exact Si (0 0 1) substrates for III/V device integration," *J. Cryst. Growth* **315**(1), 37–47 (2011) [doi:10.1016/j.jcrysgro.2010.10.036].

Danksagung

Ich möchte mich bei allen Menschen bedanken, die mich während dieser Arbeit unterstützt haben. Besonderer Dank geht an:

- Prof. Thomas Hannappel für die Betreuung meiner Arbeit am Helmholtz-Zentrum Berlin und an der TU Ilmenau und für die vielen lebhaften und motiverenden Diskussionen,
- Prof. Recardo Manzke für die Bereitschaft das Erstgutachten der Arbeit an der Humboldt-Universität zu Berlin zu übernehmen,
- Prof. Wolf Gero Schmidt für die Übernahme des externen Gutachtens,
- meinen engsten Kollgen Henning Döscher, Peter Kleinschmidt, Oliver Supplie, die mich bei allen erdenklichen Aufgaben bestens unterstützt haben,
- Anja Dobrich für die FTIR-Messungen und die Zusammenarbeit hinsichtlich Si(100),
- Christian Höhn, Sven Kuballa, und Antonio Müller für zuverlässigen Betrieb der MOCVD-Anlage und den UHV-Geräte und die verlässliche Hilfe bei streikender Technik und schwierigen experimentellen Situationen,
- Enrique Barrigon für die lustige und produktive Zusammenarbeit auf dem Ge(100)-Substrat,
- den Diplomanten Sjoerd Verhagen, Claas Löbbel, Johannes Luczak für die große Hilfe und Zuarbeit bei der MOCVD-Präparation und Probencharakterisierung,
- Nadine Szabo für die Unterstützung bei der Einarbeitung in die MOCVD-Welt,
- Matthias May und Thomas Hänsel für die vielen hilfreichen Diskussionen rund um Photoelektronenspektroskopie und UHV,

- den Kollegen und Projektpartnern am Fraunhofer ISE aus der Arbeitsgruppe Dimroth und an der Philipps Universität Marburg aus Arbeitsgruppe Stolz für zahlreiche Diskussionen und fachlichen Austausch während des BMBF-Projektes III-V-Si(100)

- den Sekretärinnen Karin Regelin, Simone Gutsche und Julia Wyrostek für die Unterstützung bei sämtlichen bürokratischen und organisatorischen Aufgaben,

- allen Kollegen der Arbeitsgruppe am HZB (ex-SE4, ex-IE-5, ex-IE-6, jetzt Teil von IE-F) und der TU Ilmenau für das stets angenehme und schöne Arbeitsumfeld,

- dem BMBF für die finazielle Unterstützung (Projekte 03SF0329C und 03SF0404A).

Außerdem möchte ich meiner Familie, meiner Freundin und all meinen Freunden für praktische und geistige Unterstützung während meiner Arbeit danken.